AAM (FINAL DRAFT)

DOI: https://doi.org/10.1016/j.ebiom.2025.106087

COVID-19 vaccine type controls stromal reprogramming in draining lymph nodes

Authors: Ruth Fair-Mäkelä[1,2], Pinja Thorén[2,3]†, Joni Näsiaho[2,3]†, Pia Sundqvist[2,3], Irina Piiroinen[2,3], Laura Kähäri[2,3], Ilkka Julkunen[1,2], Johanna Ivaska[2,4,5,6], Elin Hub[7], Antal Rot[7], Bishwa Ghimire[1,2,3], Jonna Alanko[2,3,4], Marko Salmi[1,2,3]*

Affiliations:

[1]Institute of Biomedicine, University of Turku; Turku, Finland.

[2]InFLAMES Research Flagship Center, University of Turku; Turku, Finland.

[3]MediCity Research Laboratory, University of Turku; Turku, Finland.

[4]Turku Bioscience, University of Turku; Turku, Finland.

[5]Department of Life Technologies, University of Turku; Turku, Finland.

[6]Foundation for the Finnish Cancer Institute; Helsinki, Finland.

[7]William Harvey Research Institute, Queen Mary University of London; London, UK.

*Corresponding author. Email: marko.salmi@utu.fi

†These authors contributed equally to this work

One-Sentence Summary: Different COVID-19 vaccine formulations have distinct effects on the stromal cell landscape and function of draining lymph nodes.

Supplementary Materials for

COVID-19 vaccine type controls stromal reprogramming in draining lymph nodes

Ruth Fair-Mäkelä, Pinja Thorén, Joni Näsiaho, Pia Sundqvist, Irina Piiroinen, Laura Kähäri, Ilkka Julkunen, Johanna Ivaska, Elin Hub, Antal Rot, Bishwa Ghimire, Jonna Alanko, Marko Salmi

Corresponding author: marko.salmi@utu.fi

The PDF file includes:

Other Supplementary Materials for this manuscript include the following:

SUPPLEMENTARY MATERIALS AND METHODS

Draining of labeled Spikevax

mRNA-LNP vaccine (Spikevax) was labeled as previously described (*86*). Briefly, the vaccine was incubated with lipofilic PKH26 (MedCHemExpress, HY-D1415) at 10 µg/ml for 15 min at room temperature, and the excess label was filtered with a 10-kDa cutoff centrifugal filter unit (Millipore, MRCPRT010). Spikevax-PKH26 (4 µg of Spikevax mRNA in 20 µl volume) was administered subcutaneously (s.c.) or intramuscularly (i.m.) into recipient mice and the draining LNs were collected at 10-min or 6-hour time points post-immunization. After collection, LNs were directly imaged for the labeled vaccine with a Zeiss AxioZOOM.V16 stereomicroscope.

Vaccine mRNA expression in dLN leukocytes

$CD45^+CD11b^+$, $CD45^+CD11c^+$ and $CD45^+CD11b^+CD11c^+$ cells were isolated from digested Spikevax-draining LNs and enriched by sorting using the Sony SH800 Cell Sorter and a 100-µm microfluidics chip. Samples were processed into single-cell libraries, sequenced and postprocessed following the same protocol described for stromal cells (as specified in "Library preparation and scRNA-seq" in Materials and Methods). Downstream analysis was performed in R (version 4.3.0) using standard Seurat (version 4.3.0) protocol. Unsupervised clustering and analysis of key myeloid cell markers identified a distinct dendritic cell population (*Siglech*$^+$, *Ccr7*$^+$, *Cd209a*$^+$) and a monocyte-macrophage population (*Fcgr1*$^+$, *Msr1*$^+$, *Csfr1*$^+$). Few contaminating lymphocytes were also detected, including T cells (*Cd4*$^+$, *Cd8a*$^+$, *Cd3g*$^+$) and B cells (*Ms4a1*$^+$). Raw Spikevax mRNA counts were extracted from each identified leukocyte population and compared to LECs from the stromal dataset.

Image acquisition and processing

Immunofluorescent-labeled samples were examined with the Zeiss LSM880 confocal microscope (ZEISS Microscopy) with a Plan-Apochromat 10X/0.45, 20X/0.8, LD LCI Plan-Apochromat 40X/1.2, and C Plan-Apochromat 63X/1.4 objectives, and the ZEN 2.3 SP1 Black Edition software. Pinhole adjustments were used to produce the same slice thickness for each channel. Multi-tissue vibratome section *z*-stacks were imaged with the 10X objective (10 to 20 planes with *z*-step thickness of 5.5 to 6 µm) and the 40X objective (40 to 60 planes with *z*-step thickness of 0.6 µm). A 3i Marianas CSU-W1 spinning disk confocal microscope (3i) with a Plan-Apochromat 20X/0.8, a LD c-Apochromat 40X/1.1W objective, and a Hamamatsu sCMOS Orca Flash4.0 camera was used to acquire confocal images using the SlideBook 6 software (Intelligent Imaging Innovations). Conduit filling experiments with the CNA-35-EGFP probe (Fig. 6E) were imaged with a Nikon Eclipse Ti2-E widefield microscope equipped with a Plan Apo Lambda 20X/0.75 objective and a Hamamatsu sCMOS Orca Flash4.0 camera.

FISH samples were imaged with the Zeiss LSM880 confocal microscope (ZEISS Microscopy) with a 40X/1.40 objective or an Airyscan detector (ZEISS Microscopy) and a C Plan-Apochromat 63X/1.4 oil objective. High-resolution Airyscan z-stack images were acquired with the ZEN 2.3 SP1 Black Edition software and processed with the Zen 2.3 Blue Edition software.

ImageJ (v1.54p) was used to create orthogonal views, maximum intensity projections of z stacks, and to perform background subtraction [except for Fig. 1D (3D-projections), Fig. 7, B, C, and H,

and movies S1 to S10] and linear brightness adjustments to all images. Arivis Vision4D (Zeiss) was used for 3D rendering of multi-tissue whole mount images (Fig. 1D and movies S1 to S10). The fluorescent signal was visualized using volumetric rendering mode. For certain 3D images, inner structures were visualized using a clipping plane.

Pannoramic P250 slide scanner with a 20X objective (3DHISTECH Ltd) was used to acquire images of hematoxylin and eosin stained samples. Images were processed with 3DHISTECH SlideViewer (3DHISTECH Ltd).

Images of whole popliteal LNs (fig. S1F) were taken with the Zeiss Axiozoom V16 stereomicroscope (ZEISS Microscopy) equipped with a PlanNeoFluar Z 1X/0.25 objective, and an AxioCam 105 Color camera. Images were processed with Zen 3.0 SR Black edition (ZEISS Microscopy).

Image quantification

Images were analyzed with Fiji (*87*). When analyzing S protein expression kinetics in dLNs, the S protein$^+$ area was quantified from 500 × 500 pixel (SCS; defined by CD31 staining) or 700 × 700 pixel (medullary sinus) ROIs from vaccine-dLN and the contralateral non-dLN. After background subtraction, the S protein signal threshold was determined (default algorithm and cutoff value set with 6-hour time point sample, same value used for 2-hour and 30-hour samples) and the percentage of area was measured within the ROIs. Finally, any background values from the non-dLN were subtracted from the vaccine-dLN values. In 3D analyses, maximum intensity projections of vibratome images (10 slices) were created to quantify the mean fluorescence intensity (MFI) of the S protein from a CD31 mask (800 × 450 pixel ROIs from SCS and medullary sinus). CD31 signal was filtered (median filter, radius of 2.0 pixels), thresholds determined (default algorithm) and the average value (separate value for SCS and medullary sinus for each vaccine) was used to create a mask from CD31 binary images. S protein signal was measured within the created mask. Any background values from the naïve samples were subtracted from the vaccine-dLN values.

PD-L1 expression was quantified from 1400 × 1400 pixel ROIs in the medullary sinus area. After background subtraction, the PD-L1 signal threshold was determined (default algorithm and average values from Vaxzevria 6-hour sample) and the area percentage was measured from the field of view.

In scavenging receptor analyses, MFI for MARCO, MRC1, and s.c. administered 500-kDa FITC-dextran was measured from a LYVE1 mask. Briefly, background was subtracted from all images and LYVE1 signal threshold was determined from vaccinated and control samples for analysis (default algorithm, average threshold value calculated from all samples). After applying the selected threshold, a mask was created from the binary image, which was applied to measure the MFI of the target proteins/tracers within the LYVE1 mask.

In LEC junction analyses, MFI for VE-cadherin was measured from 1000 × 1000 pixel ROIs from the SCS and medullary sinus of vaccine-draining and non-dLNs. In the SCS, the MFI was measured from an ROI outlining the SCS ceiling and floor LECs. In the medullary sinus, VE-cadherin signal threshold was determined (default algorithm) and the average value (calculated from non-dLNs) was used for analysis. After applying the selected threshold, a mask was created from the binary images and VE-cadherin signal intensity was measured within the mask. Fiji was

used to measure LEC junction perimeter tracing along single LECs in the SCS based on VE-cadherin staining. The MFI of JAM-A was measured from maximum intensity projections (20 slices, thickness 0.6 µm) from selected ROIs (600 × 1200 pixels ROI for SCS, 700 × 700 pixels ROI for medullary sinus) of 3D vibratome staining and a CD31 mask. Furthermore, an ROI outlining the SCS ceiling and floor LECs was created to exclude signal of CD31 from other cell types (low level of expression in lymphocytes). CD31 signal threshold was determined (default algorithm, average value of naïve LNs) and used to create a mask. JAM-A signal intensity was measured from the mask.

In conduit function assays, WGA-A647 was analyzed from 1200 × 1200-pixel ROIs of dLN parenchymas. The signal threshold was determined (average value of control samples), the same value was applied for all analyzed samples and MFI was measured within the thresholded signal from the ROI. Collagen I and CNA-35-EGFP co-localization was analyzed by quantifying the MFI across lines drawn over the conduit using the Color Profiler plugin in Fiji. The s.c. administered CNA-35-EGFP was analyzed from the LN parenchyma omitting the medullary sinus and capsule from the analysis. A mask of the conduit was created based on the ex vivo CNA-35-tdTomato signal. For quantifying the area of ER-TR7 and ex vivo stained CNA-35, each signal threshold was determined (with the average thresholding value applied to all analyzed samples), and the area of the signal was measured from the LN.

We also quantified chemokine and chemokine receptor expression in LNs. Integrated density of ACKR4 was measured from a 10-µm wide region covering the SCS (the edge of the LN) and from inside the LN. After subtracting the corresponding background, the value was divided by the measured area for MFI. The MFI of extracellular CCL21 was measured from the whole LN. To study the chemokine scavenging capacity, we measured the MFI of CCL19-AF647 (labeled chemokine administered s.c.) from the LN SCS region from images, where the background was subtracted and the SCS region was manually selected based on the CD31-AF488 signal.

The distribution of bone-marrow derived $DsRed^+$ migratory DCs (migDC) was analyzed from maximum image projections of *z*-stacks. The migDC signal threshold was determined (default algorithm, average value of all samples) and the proportion of the signal in the SCS or non-SCS area was calculated in control and Spikevax-dLNs. Capsule thickness (including both CNA-35 and the underlying Collagen IV signal) was measured from the medullary sinus region using Fiji.

Under-agarose eosinophil migration assay

Eosinophils were isolated from enzymatically digested Nuvaxovid-dLNs (24 h time point), fluorescently stained and sorted based on a negative selection strategy (*88*) using the Sony SH800 Cell Sorter and a 100-µm microfluidics chip. The agarose assay was performed as previously described (*82*) with minor modifications. UltraPure Agarose (0.75%) (Invitrogen, 16500100) in phenol-free RPMI (Gibco, 11835030) supplemented with 5% FBS and 1X Hanks' balanced salt solution (HBSS) (pH 7.3; Sigma-Aldrich, H1387) was poured into custom-made chambers and allowed to polymerize for 30 min. A 2 mm–diameter hole was punched into the agarose for 6 µl of CCL11 at 10 µg/ml (R&D Systems, 420-ME-020/CF) or vehicle control (media without CCL11). Eosinophils were stained with NucBlue™ (Invitrogen, R37605) for 10 min at 37°C and 3×10^4 to 5×10^4 cells were injected under agarose in 1 µl of medium 3 mm away from the hole with the attractant. Cell migration was immediately recorded with an inverted Nikon Ti2 wide-field fluorescent microscope at 37°C with 5% CO_2 for 90 min with 1-min intervals using a Plan-

Fluor 4X/0.13 objective and a Hamamatsu sCMOS Orca Flash4.0 camera. Cell migration was analyzed in ImageJ2 (*89*) with the TrackMate plugin for automated cell tracking (*90*) excluding unmoving dead cells. The plots of origin normalized tracks were created in CellTracksColab (*91*).

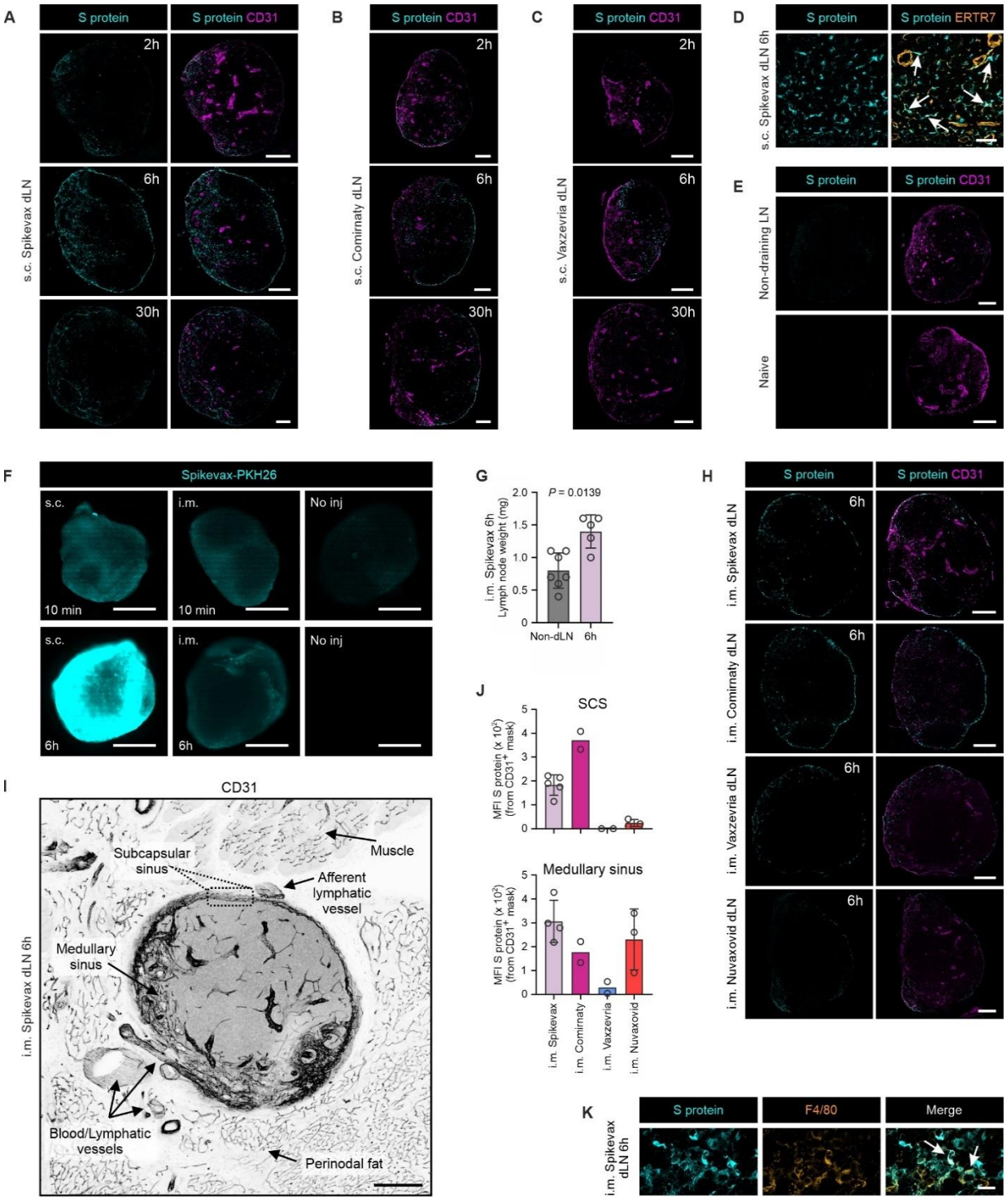
A
S protein
S protein CD31
2h
6h
30h
s.c. Spikevax dLN
B
S protein CD31
2h
6h
30h
s.c. Comirnaty dLN
C
S protein CD31
2h
6h
30h
s.c. Vaxzevria dLN
D
S protein
S protein ERTR7
s.c. Spikevax dLN 6h
E
S protein
S protein CD31
Non-draining LN
Naive
F
Spikevax-PKH26
s.c.
i.m.
No inj
10 min
10 min
6h
6h
G
P = 0.0139
i.m. Spikevax 6h
Lymph node weight (mg)
2.0
1.5
1.0
0.5
0
Non-dLN
6h
H
S protein
S protein CD31
6h
i.m. Spikevax dLN
i.m. Comirnaty dLN
i.m. Vaxzevria dLN
i.m. Nuvaxovid dLN
I
CD31
i.m. Spikevax dLN 6h
Subcapsular sinus
Muscle
Afferent lymphatic vessel
Medullary sinus
Blood/Lymphatic vessels
Perinodal fat
J
SCS
MFI S protein (x 10²)
(from CD31+ mask)
Medullary sinus
i.m. Spikevax
i.m. Comirnaty
i.m. Vaxzevria
i.m. Nuvaxovid
K
S protein
F4/80
Merge
i.m. Spikevax dLN 6h

Fig. S1. dLN stromal cells become SARS-CoV-2 S protein positive early after COVID-19 vaccinations. (**A** to **C**) Whole LN confocal images of S protein (cyan) and CD31 (magenta) in the dLNs after subcutaneous (s.c.) (A) Spikevax, (B) Comirnaty, and (C) Vaxzevria immunizations, n = 2 to 3 LNs per group. Scale bars: 200 μm. (**D**) Confocal images of S protein (cyan) and ERTR7 (orange) after s.c. Spikevax immunization, n = 3 LNs. Arrows mark S protein$^+$ stromal cells around the conduit. Scale bar: 50 μm. (**E**) Confocal images of S protein (cyan) and CD31 (magenta) in whole non-draining and naïve LNs, n = 3 LNs per group. Scale bars: 200 μm. (**F**) Drainage of PKH26-labeled Spikevax (cyan) in dLNs (s.c. and intramuscular (i.m.) administration), n = 2 LNs per group. Non-injected LNs serve as negative controls. Scale bars: 500 μm. (**G**) Tissue weights of Spikevax-non-dLNs and -dLNs (i.m. immunizations), n = 5 to 7 LNs per group. (**H**) Whole LN confocal images of S protein (cyan) and CD31 (magenta) in the dLNs after the indicated i.m. immunizations, n = 2 to 4 LNs per group. Scale bars: 200 μm. (**I**) Multi-tissue vibratome sample of Spikevax-dLN stained with CD31 (black) and annotated for the different tissue structures, n = 4. Scale bar: 200 μm. (**J**) Quantification of S protein mean fluorescence intensity (MFI) from endothelial CD31$^+$ mask in the subcapsular sinus (SCS) and medullary sinus in dLNs of immunized mice (i.m.) (representative images are shown in Fig. 1D), n = 2 to 5 LNs per group. (**K**) Confocal images of S protein (cyan) and F4/80 (orange) in the medullary sinus of Spikevax-dLN (i.m. immunizations), n = 2. Arrows mark double-positive cells. Scale bar: 20 μm. Data are from (A to I) 2 to 4, or (J and K) 1 to 2 independent experiments and are presented as means ± SD. Statistical significance was tested using (G) Mann–Whitney *U* test.

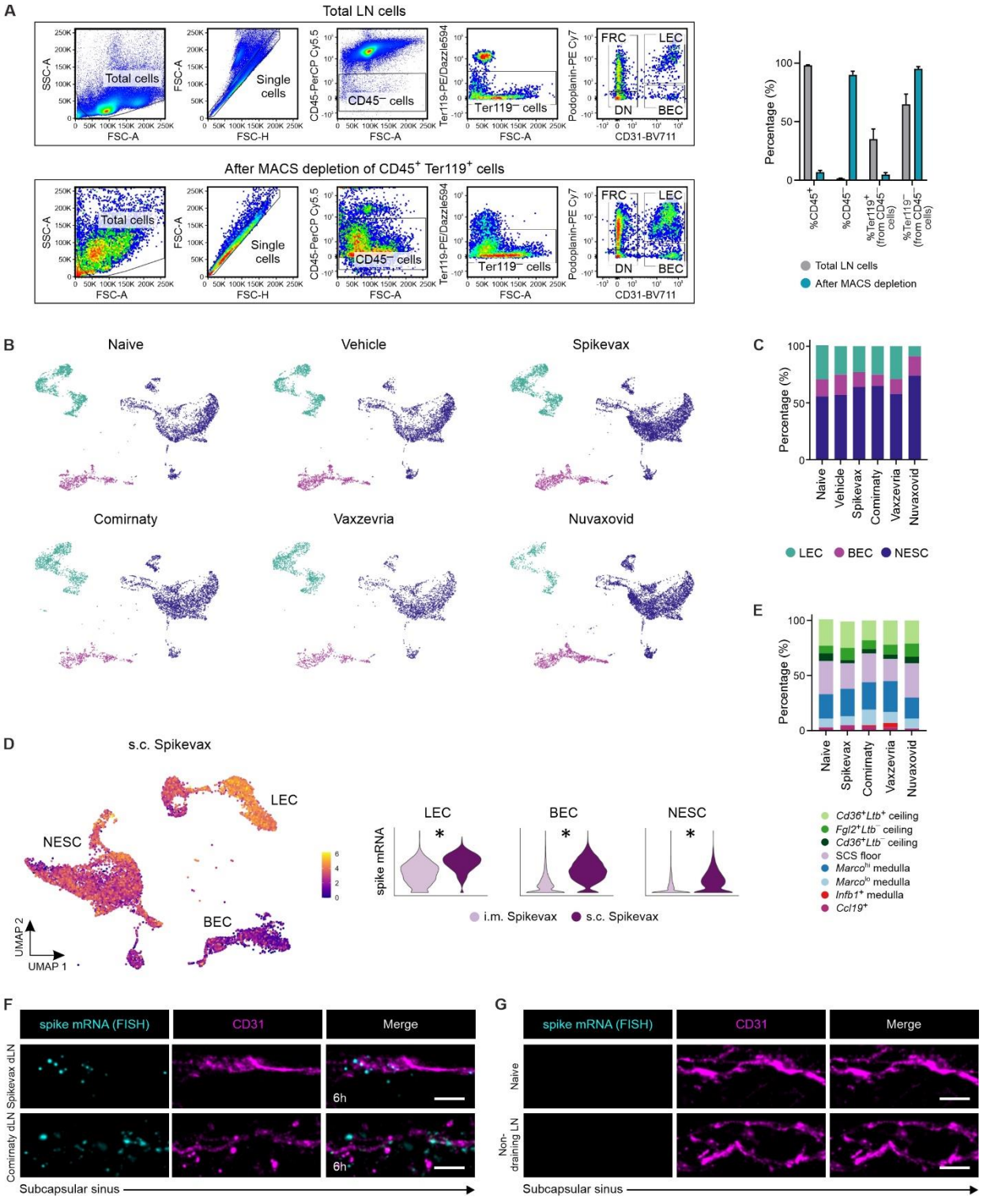
A
Total LN cells
Total cells
Single cells
CD45⁻ cells
Ter119⁻ cells
FRC
LEC
DN
BEC
SSC-A
FSC-A
FSC-H
CD45-PerCP Cy5.5
Ter119-PE/Dazzle594
Podoplanin-PE Cy7
CD31-BV711
After MACS depletion of CD45+ Ter119+ cells
Percentage (%)
%CD45+
%CD45−
%Ter119+ (from CD45− cells)
%Ter119− (from CD45− cells)
Total LN cells
After MACS depletion
B
Naive
Vehicle
Spikevax
Comirnaty
Vaxzevria
Nuvaxovid
C
Percentage (%)
Naive
Vehicle
Spikevax
Comirnaty
Vaxzevria
Nuvaxovid
LEC
BEC
NESC
D
s.c. Spikevax
LEC
NESC
BEC
UMAP 2
UMAP 1
spike mRNA
LEC
BEC
NESC
i.m. Spikevax
s.c. Spikevax
E
Percentage (%)
Naive
Spikevax
Comirnaty
Vaxzevria
Nuvaxovid
Cd36+Ltb+ ceiling
Fgl2+Ltb− ceiling
Cd36+Ltb− ceiling
SCS floor
Marcohi medulla
Marcolo medulla
Infb1+ medulla
Ccl19+
F
spike mRNA (FISH)
CD31
Merge
Spikevax dLN
Comirnaty dLN
6h
6h
Subcapsular sinus
G
spike mRNA (FISH)
CD31
Merge
Naive
Non-draining LN
Subcapsular sinus

Fig. S2. Identification of stromal cell clusters, subclusters, and spike mRNA expression in dLNs of COVID-19 vaccinated mice. (**A**) Flow cytometry analysis and quantification of samples for scRNA-seq before and after depletion of $CD45^+$ and $Ter119^+$ cells from naïve popliteal LNs (same LN drains the vaccine in immunized mice). (**B**) Uniform Manifold Approximation and Projection (UMAP) embedding of stromal cells for each analyzed sample in Fig. 2A (i.m. immunizations). (**C**) The percentage of cells falling into LECs, BECs, and NESCs (color coding as in Fig. 2A) for all samples (i.m. immunizations). (**D**) UMAP of dLN stromal cells colored by spike mRNA expression 6 hours after s.c. administration of Spikevax. Quantification (violin plots) comparing spike mRNA expression in dLNs 6 hours after s.c. and i.m. (i.m. data is from Fig. 2B) administration of Spikevax. (**E**) The percentage of cells falling into LEC subcluster populations (color coding as in Fig. 2C) for all samples (i.m. immunizations). (**F** and **G**) Maximum intensity projections of fluorescence in situ hybridization (FISH) of S protein mRNA (cyan) and CD31 staining (magenta) in (F) dLNs 6 hours after i.m. administration of Spikevax and Comirnaty vaccines (orthogonal views are shown in Fig. 2E) and (G) naïve and non-draining LNs as specificity controls. Scale bars: 5 μm. Data are (A to E) pooled from 30 LNs and 15 mice per group or (F and G) representative of 3 LNs per group from 3 independent experiments. Statistical significance was tested using (D) Wilcoxon rank sum with Bonferroni-correction (*P <0.05).

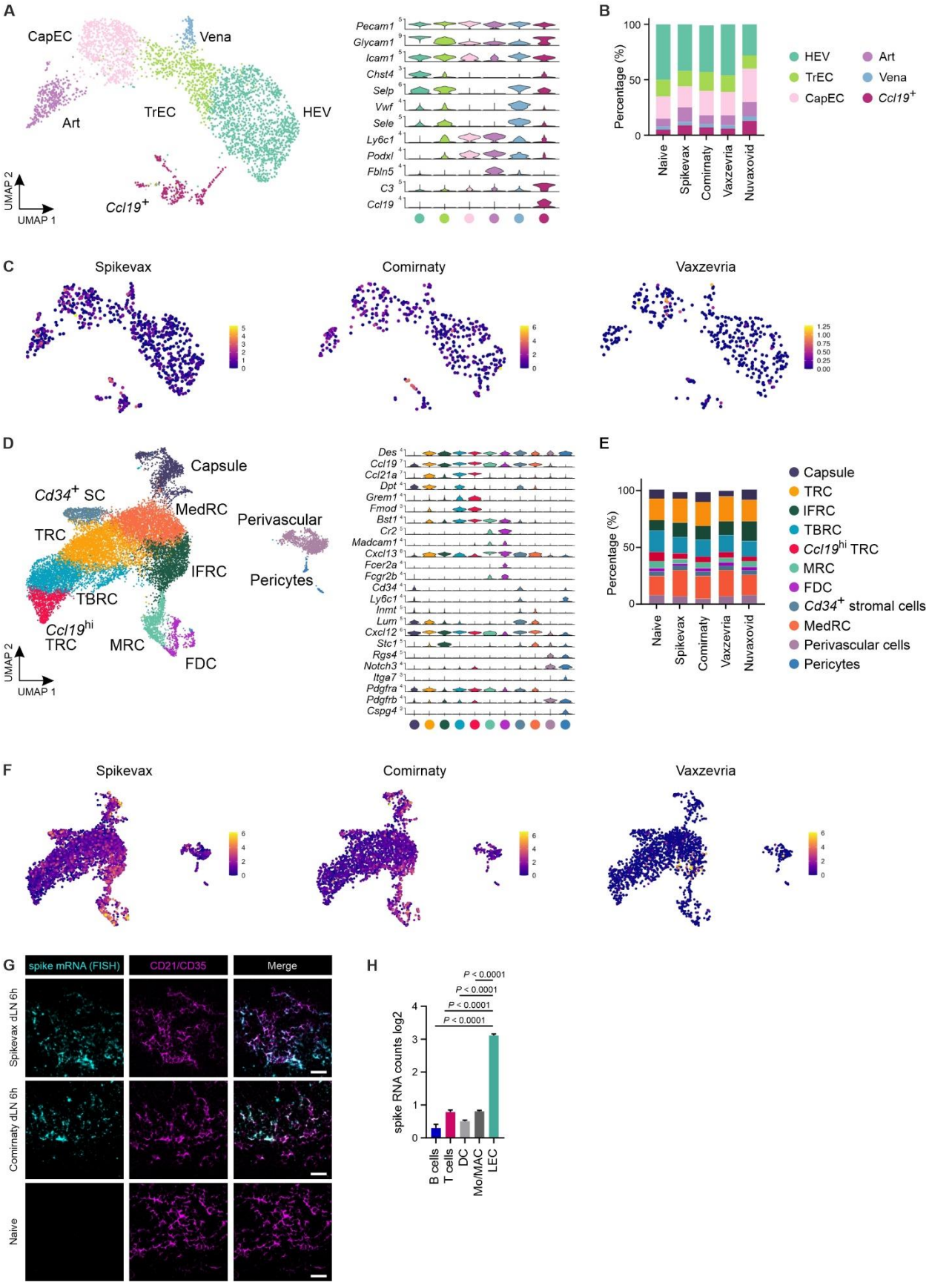
A
CapEC
Vena
Art
TrEC
HEV
Ccl19+
UMAP 2
UMAP 1
Pecam1
Glycam1
Icam1
Chst4
Selp
Vwf
Sele
Ly6c1
Podxl
Fbln5
C3
Ccl19
B
Percentage (%)
Naive
Spikevax
Comirnaty
Vaxzevria
Nuvaxovid
HEV
TrEC
CapEC
Art
Vena
Ccl19+
C
Spikevax
Comirnaty
Vaxzevria
D
Capsule
Cd34+ SC
MedRC
Perivascular
TRC
IFRC
Pericytes
TBRC
Ccl19hi TRC
MRC
FDC
UMAP 2
UMAP 1
Des
Ccl19
Ccl21a
Dpt
Grem1
Fmod
Bst1
Cr2
Madcam1
Cxcl13
Fcer2a
Fcgr2b
Cd34
Ly6c1
Inmt
Lum
Cxcl12
Stc1
Rgs4
Notch3
Itga7
Pdgfra
Pdgfrb
Cspg4
E
Percentage (%)
Naive
Spikevax
Comirnaty
Vaxzevria
Nuvaxovid
Capsule
TRC
IFRC
TBRC
Ccl19hi TRC
MRC
FDC
Cd34+ stromal cells
MedRC
Perivascular cells
Pericytes
F
Spikevax
Comirnaty
Vaxzevria
G
spike mRNA (FISH)
CD21/CD35
Merge
Spikevax dLN 6h
Comirnaty dLN 6h
Naive
H
P < 0.0001
P < 0.0001
P < 0.0001
P < 0.0001
spike RNA counts log2
B cells
T cells
DC
Mo/MAC
LEC

Fig. S3. Identification of BEC and NESC subclusters and spike mRNA expression in dLNs of COVID-19 vaccinated mice. (**A**) UMAP embedding of BECs depicting the six clusters (colored by cluster identity) and their signature genes shown in violin plots. (**B**) The percentage of cells falling into BEC subcluster populations. (**C**) UMAPs of BECs colored by the expression of spike mRNA. (**D**) UMAP of NESCs depicting the eleven clusters (colored by cluster identity) and their signature genes shown in violin plots. (**E**) The percentage of cells falling into NESC subcluster populations. (**F**) UMAPs of NESCs colored by the expression of spike mRNA. (**G**) FISH of S protein mRNA (cyan) and CD21/CD35 staining (magenta) in Spikevax- or Comirnaty-dLNs and LN of naïve control mice. Scale bars 20 µm. (**H**) Expression of spike mRNA in LECs and leukocyte populations from Spikevax-dLNs. All data (A to H) are obtained from i.m. vaccinated mice at 6 hours post-vaccination. Data are (A to F and H) pooled from 30 LNs and 15 mice per group or (G) are representative of 1 to 3 LNs per group from 2 independent experiments. Statistical significance was tested using (H) Student's *t* test.

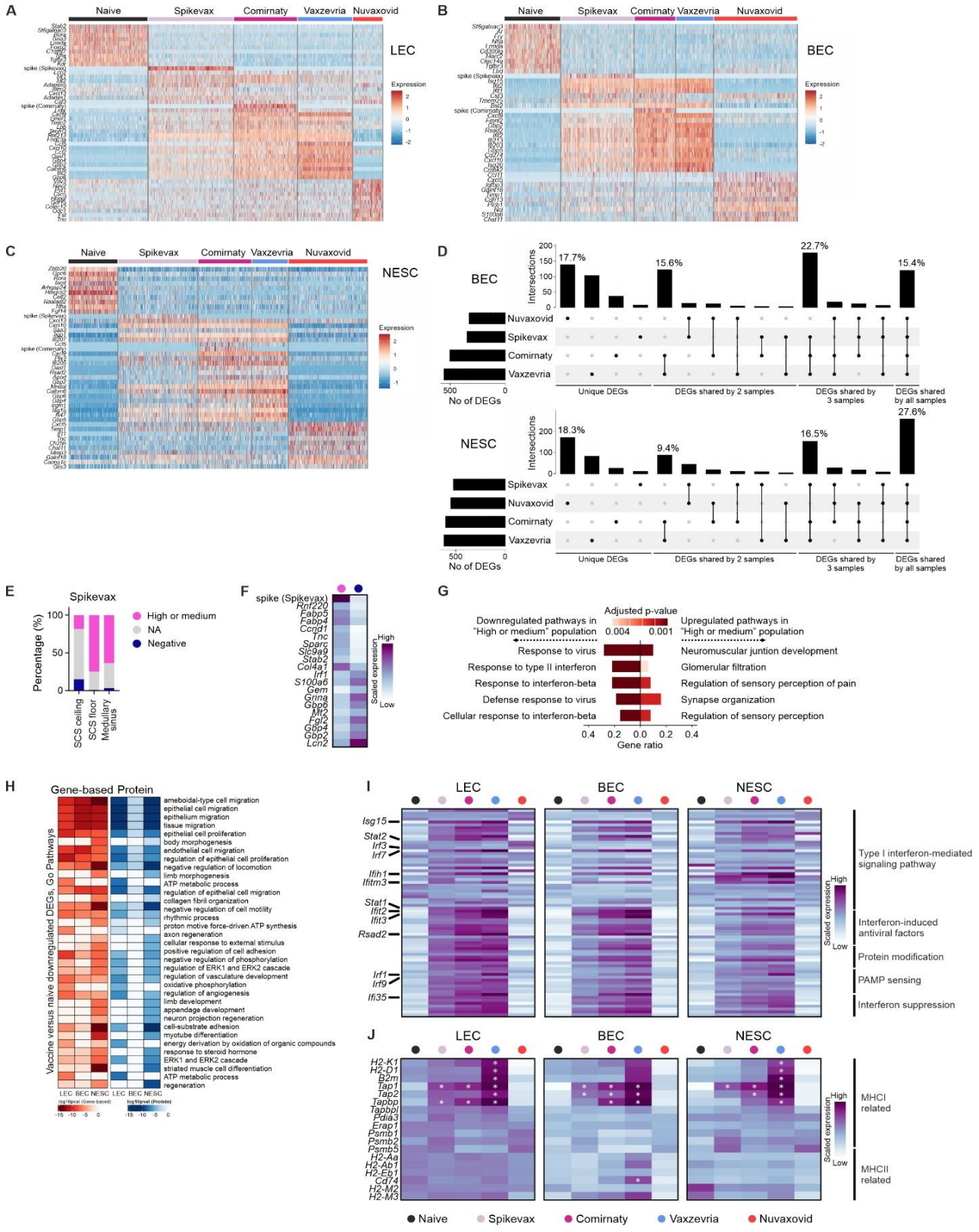
A
Naive
Spikevax
Comirnaty
Vaxzevria
Nuvaxovid
LEC
Expression
B
BEC
C
NESC
D
BEC
Intersections
17.7%
15.6%
22.7%
15.4%
Nuvaxovid
Spikevax
Comirnaty
Vaxzevria
No of DEGs
Unique DEGs
DEGs shared by 2 samples
DEGs shared by 3 samples
DEGs shared by all samples
NESC
18.3%
9.4%
16.5%
27.6%
E
Spikevax
Percentage (%)
High or medium
NA
Negative
SCS ceiling
SCS floor
Medullary sinus
F
spike (Spikevax)
Scaled expression
High
Low
G
Adjusted p-value
Downregulated pathways in "High or medium" population
Upregulated pathways in "High or medium" population
Response to virus
Response to type II interferon
Response to interferon-beta
Defense response to virus
Cellular response to interferon-beta
Neuromuscular junction development
Glomerular filtration
Regulation of sensory perception of pain
Synapse organization
Regulation of sensory perception
Gene ratio
H
Gene-based Protein
Vaccine versus naive downregulated DEGs, Go Pathways
ameboidal-type cell migration
epithelial cell migration
epithelium migration
tissue migration
epithelial cell proliferation
body morphogenesis
endothelial cell migration
regulation of epithelial cell proliferation
negative regulation of locomotion
limb morphogenesis
ATP metabolic process
regulation of epithelial cell migration
collagen fibril organization
negative regulation of cell motility
rhythmic process
proton motive force-driven ATP synthesis
axon regeneration
cellular response to external stimulus
positive regulation of cell adhesion
negative regulation of phosphorylation
regulation of ERK1 and ERK2 cascade
regulation of vasculature development
oxidative phosphorylation
regulation of angiogenesis
limb development
appendage development
neuron projection regeneration
cell-substrate adhesion
myotube differentiation
energy derivation by oxidation of organic compounds
response to steroid hormone
ERK1 and ERK2 cascade
striated muscle cell differentiation
ATP metabolic process
regeneration
LEC BEC NESC LEC BEC NESC
I
LEC
BEC
NESC
Isg15
Stat2
Irf3
Irf7
Ifih1
Ifitm3
Stat1
Ifit2
Ifit3
Rsad2
Irf1
Irf9
Ifi35
Scaled expression
High
Low
Type I interferon-mediated signaling pathway
Interferon-induced antiviral factors
Protein modification
PAMP sensing
Interferon suppression
J
LEC
BEC
NESC
H2-K1
H2-D1
B2m
Tap1
Tap2
Tapbp
Tapbpl
Pdia3
Erap1
Psmb1
Psmb2
Psmb5
H2-Aa
H2-Ab1
H2-Eb1
Cd74
H2-M2
H2-M3
MHCI related
MHCII related
Naive
Spikevax
Comirnaty
Vaxzevria
Nuvaxovid

Fig. S4. Different COVID-19 vaccines induce distinct stromal cell responses in the dLNs. (**A** to **C**) Heatmap of top differentially expressed genes (DEG) for naïve and vaccine-primed (A) LECs, (B) BECs, and (C) NESCs. (**D**) UpSet plots of unique and shared DEGs of BECs and NESCs when comparing individual vaccine samples to the naïve control. (**E**) Percentage of LEC subtypes falling into cells expressing spike mRNA at high or medium level (pink) and negative cells (non-transfected, blue) in Spikevax-dLNs [NA, cells expressing spike mRNA at low levels were excluded from comparison in (F)]. (**F**) Heatmap of top 10 DEGs expressed in the transfected and negative SCS ceiling LECs [from (E)]. (**G**) Pathway analysis of DEGs in the transfected and negative SCS ceiling LECs [from (E)]. (**H**) Top 20 downregulated gene pathways induced in dLNs by gene-based and protein vaccines. (**I**) Heatmaps of selected interferon-inducible genes in LECs, BECs, and NESCs. Genes with significantly altered expression are depicted in Data file S1. (**J**) Heatmaps of genes belonging to MCHI- and MCHII-related antigen presentation pathways in vaccine-primed dLNs. All data (A to J) are obtained from i.m. immunized mice at the 6-hour time point and are pooled from 30 LNs and 15 mice per group. Statistical significance was tested using (I and J) Wilcoxon rank sum with Bonferroni-correction (*P <0.05).

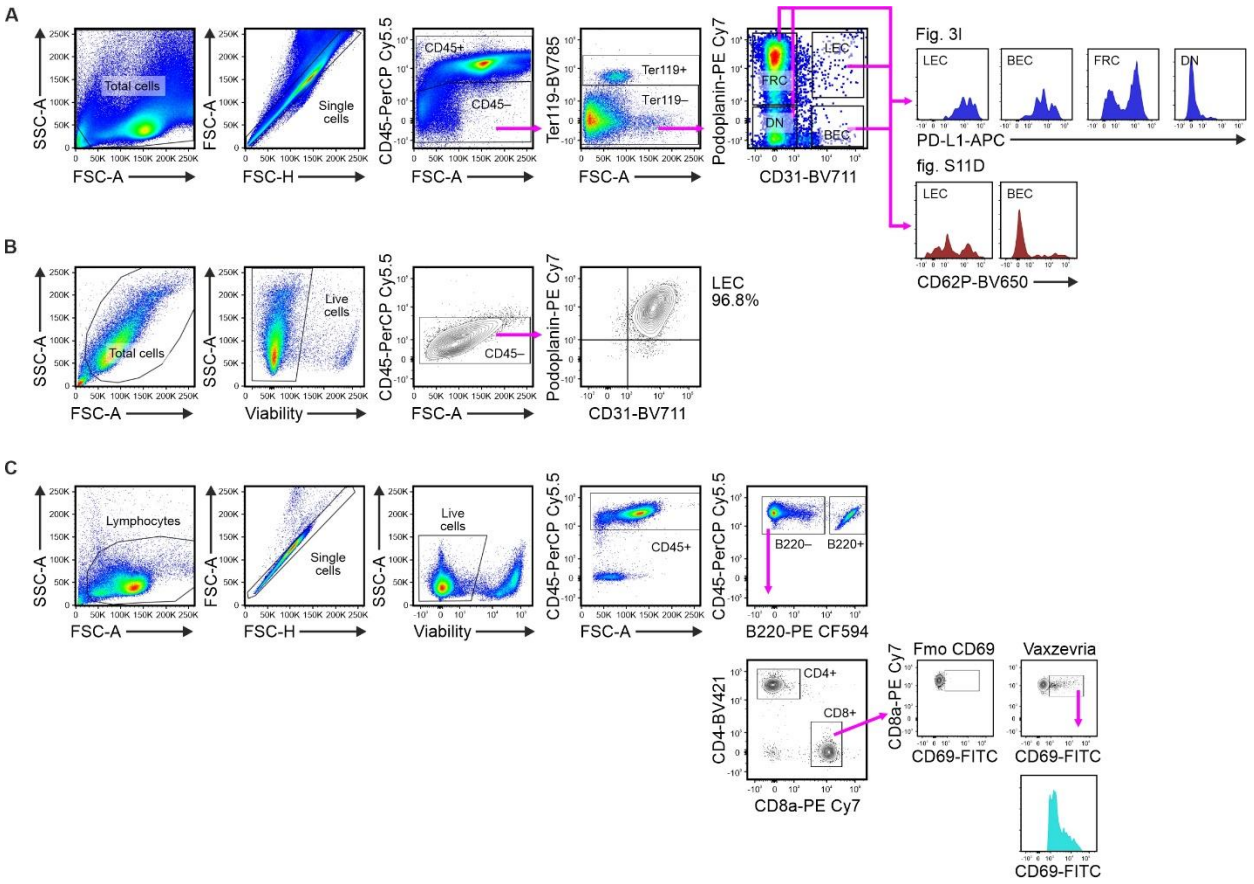

Fig. S5. Gating strategies for analyzing stromal cells and in vitro T cell activation assay. (**A**) Flow cytometry gating strategy used to identify LN stromal subpopulations in Fig. 3I and fig. S11D. (**B**) Flow cytometry analysis of in vitro cultured primary stromal cells isolated from LNs. (**C**) Flow cytometry gating strategy used to study CD69 induction on lymphocytes after co-culture with stromal cells in Fig. 3, L and M (the visualized plots are the same as in Fig. 3L).

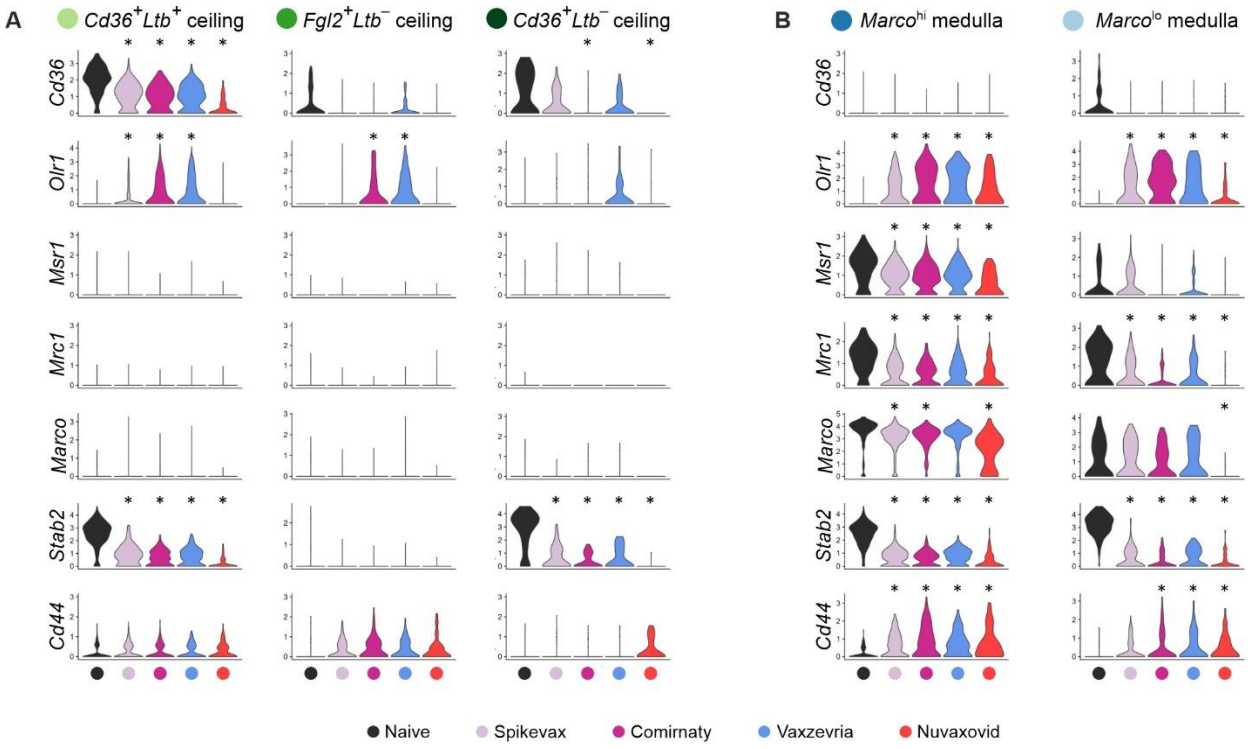

Fig. S6. Scavenger receptor expression in sinusoidal LECs is reprogrammed after immunizations. (**A** and **B**) Violin plots of selected scavenger receptor mRNA expression in the (A) subcapsular sinus and (B) medullary sinus LEC subclusters. All data (A and B) are obtained from i.m. vaccinated mice at the 6-hour time point and are pooled from 30 LNs and 15 mice per group. Statistical significance was tested using (A and B) Wilcoxon rank sum with Bonferroni-correction (*P <0.05).

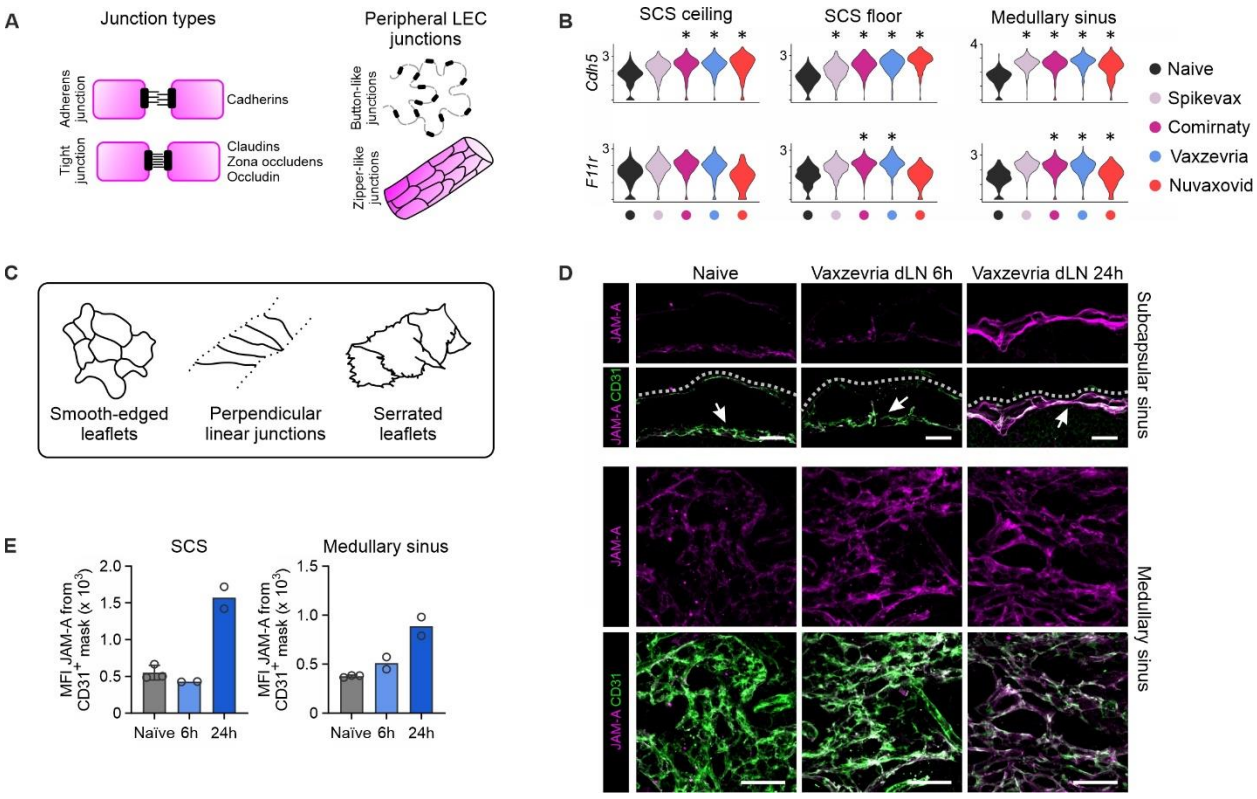

Fig. S7. Expression of junctional molecules is altered in LECs of vaccine-primed dLNs. (**A**) Schematic drawing of junction types and junction morphologies in peripheral afferent lymphatic vessel LECs. (**B**) Violin plots of *Cdh5* and *F11r* (encoding JAM-A) expression in SCS ceiling, floor and medullary sinus LECs in LNs of naïve mice and 6 hours after the indicated immunizations. (**C**) Schematic drawing of morphologically separate LEC junctions in the SCS, which are comprised of smooth-edged leaflet, perpendicularly linear and serrated leaflet-like junctions. (**D**) Maximum intensity projections of confocal images of multi-tissue vibratome samples stained for CD31 (green) with JAM-A (magenta) in the SCS and medullary sinus of naïve LN and dLNs 6 and 24 hours after Vaxzevria immunization, n = 2 to 3 LNs per group. Scale bars: 20 µm. (**E**) Quantification of mean fluorescence intensities (MFI) for JAM-A from a $CD31^+$ mask [from (D)], n = 2 to 3 LNs per group. Dashed line, SCS LEC ceiling; arrow, SCS floor. Scale bars: 20 µm. All data (B, D to E) are obtained from i.m. vaccinated mice. Data are from (B) 30 LNs and 15 mice per group, are from (D and E) 1 to 2 independent experiments and are presented as means ± SD. Statistical significance was tested using (B) Wilcoxon rank sum with Bonferroni-correction (*P <0.05).

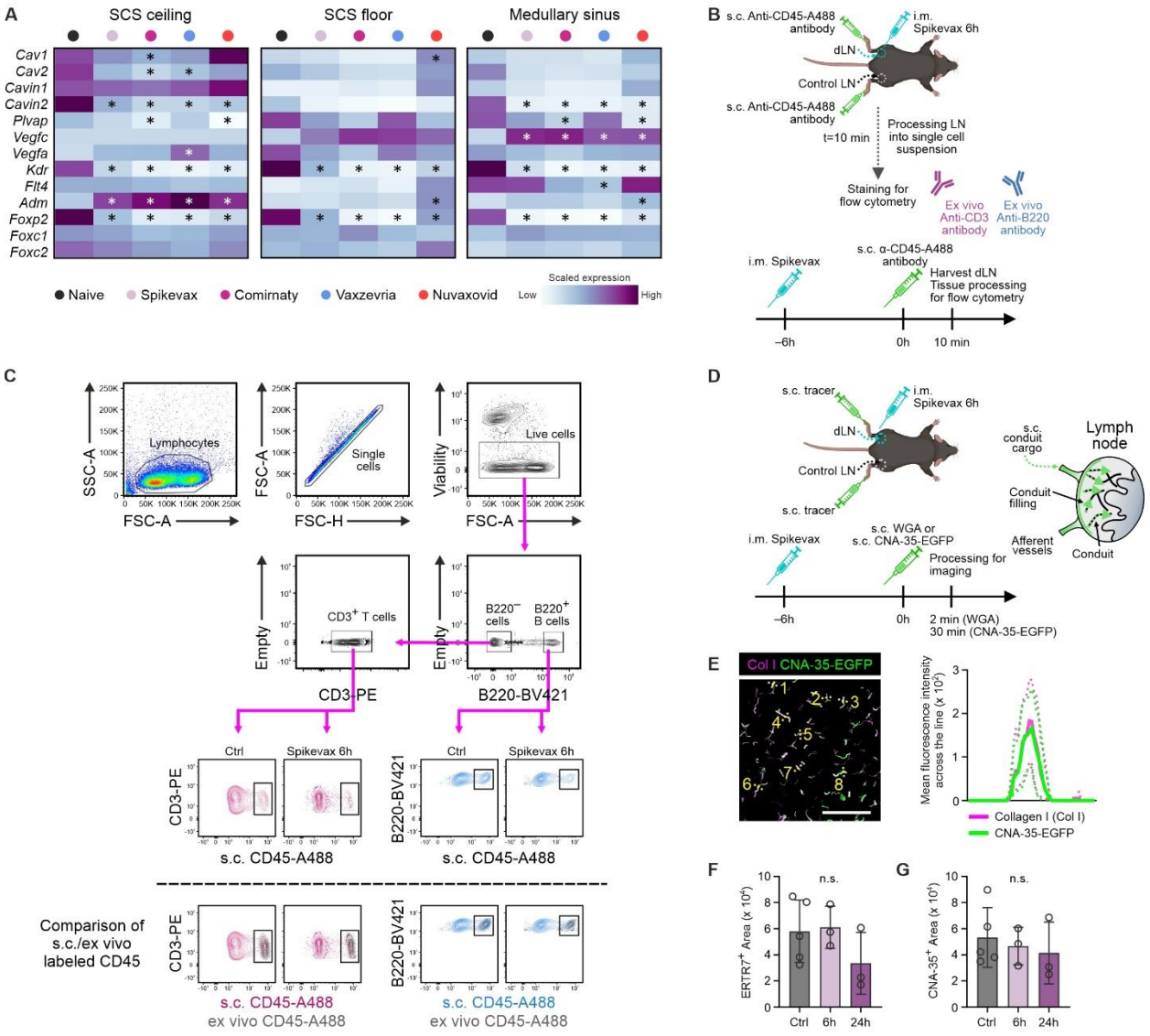

Fig. S8. Filtering of lymph-borne antigens is hampered in the dLNs early after immunizations. (**A**) Heatmaps showing expression of genes related to regulation of permeability in vaccine-primed dLNs 6-hours post-vaccination. (**B**) Experimental outline of transcytosis assays (in Fig. 6A) showing immunization (i.m.) with Spikevax, administration (s.c.) of a fluorescently-labeled anti-CD45 antibody after 6 hours followed by dLN harvesting 10 min later, and ex vivo staining for CD3 and B220. Graphics created with Biorender. (**C**) Flow cytometry gating strategy used for analyzing the binding of in vivo administered fluorescently-labeled anti-CD45 antibody (s.c. CD45-A488) to dLN lymphocytes in Fig. 6A (the visualized plots are the same as in Fig. 6A). The bottom row shows control plots onto which data from a separate ex vivo staining of LN lymphocytes with the anti-CD45 antibody was overlaid. (**D**) Experimental outline of conduit filling assays (in Fig. 6, C, E and F) showing immunization (i.m.) with Spikevax, administration (s.c.) of a fluorescently-labeled conduit cargo (wheat germ agglutinin (WGA) or the collagen binding probe CNA-35-EGFP) followed by dLN harvesting after 2 min (WGA) or 30 min (CNA-35-EGFP), and processing for imaging. Graphics created with BioRender (*92*). (**E**) Image

quantification of collagen I (magenta) and CNA-35-EGFP (green) across indicated lines, n = 8 measurements. The underlying microscopic image is the same as in Fig. 6D. Scale bar: 50 µm. (**F** and **G**) Quantification of the ex vivo-stained (F) ERTR7 and (G) CNA-35-tdTomato area in the Spikevax-non-dLN and -dLNs, n = 3 to 5 LNs. All data (A, C, F, G) are from i.m. vaccinated mice. Data are pooled from (A) 30 LNs from 15 mice in each group from (E to G) 3 independent experiments and are presented as (E) means ± confidence intervals or (F and G) means ± SD. Statistical significance was tested using (F and G) Kruskal–Wallis *H*. n.s., not significant.

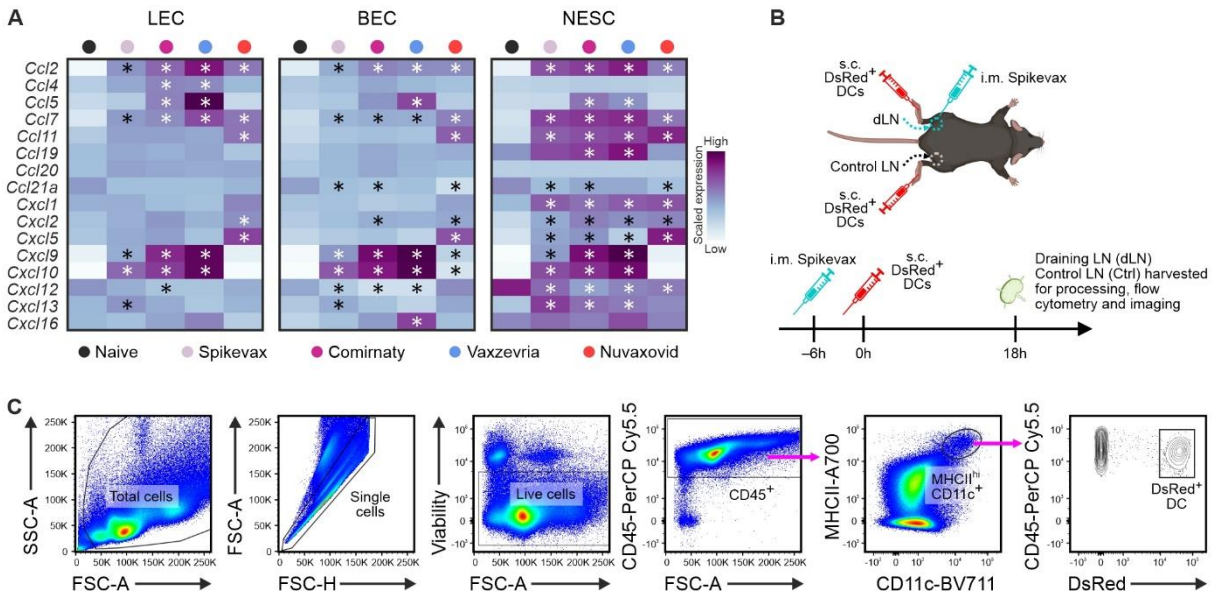

Fig. S9. Chemokine expression in vaccine-primed dLN stromal cells and flow cytometry analyses of dendritic cell subsets. (**A**) Heatmaps of chemokine gene encoding mRNAs in LEC, BEC and NESC in naïve LN and dLN 6 hours after i.m. administration of the indicated vaccines. (**B**) Experimental outline of DC migration assay (in Fig. 7, I and J) showing immunization (i.m.) with Spikevax, administration (s.c.) of bone-marrow derived DsRed^{+} DCs (6 h after vaccination) followed by dLN harvesting after 18 hours. Samples were processed for flow cytometry and imaging. Graphics created with BioRender (*92*). (**C**) Gating strategy used to identify migratory DCs in LNs after adoptive transfer of bone marrow-derived DCs isolated from DsRed^{+} donor mice (the visualized plots are the same as in Fig. 7I). Data are (A) pooled from 30 LNs and 15 mice per group. Statistical significance was tested using (A) Wilcoxon rank sum with Bonferroni-correction (*P <0.05).

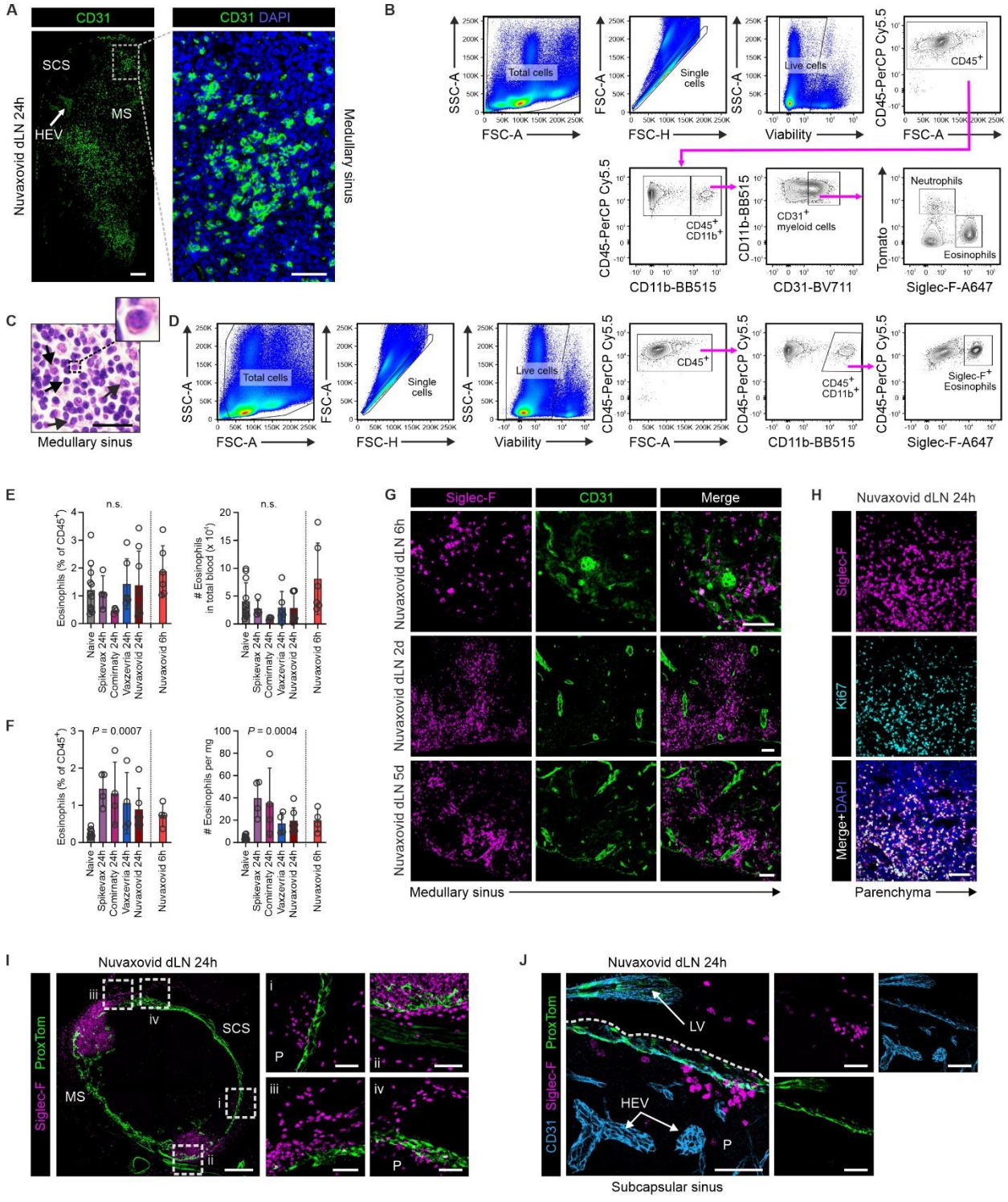
A
CD31
CD31 DAPI
SCS
MS
HEV
Nuvaxovid dLN 24h
Medullary sinus
B
Total cells
Single cells
Live cells
CD45+
Neutrophils
Eosinophils
CD45+ CD11b+
CD31+ myeloid cells
SSC-A
FSC-A
FSC-H
Viability
CD45-PerCP Cy5.5
CD11b-BB515
CD31-BV711
Tomato
Siglec-F-A647
C
Medullary sinus
D
Siglec-F+ Eosinophils
E
n.s.
Eosinophils (% of CD45+)
Eosinophils in total blood (x 10⁶)
Naive
Spikevax 24h
Comirnaty 24h
Vaxzevria 24h
Nuvaxovid 24h
Nuvaxovid 6h
F
P = 0.0007
P = 0.0004
# Eosinophils per mg
G
Siglec-F
CD31
Merge
Nuvaxovid dLN 6h
Nuvaxovid dLN 2d
Nuvaxovid dLN 5d
Medullary sinus
H
Nuvaxovid dLN 24h
Ki67
Merge+DAPI
Parenchyma
I
Nuvaxovid dLN 24h
ProxTom
iii
iv
SCS
MS
i
ii
P
J
LV
HEV
CD31
Subcapsular sinus

Fig. S10. Eosinophils infiltrate dLNs after Nuvaxovid immunizations. (**A**) Confocal images of CD31 (green) and nuclei (DAPI, blue) staining in Nuvaxovid-dLN, n = 4 LNs. A higher magnification image is from the boxed region. Scale bars: 100 µm. (**B**) Flow cytometry gating strategy and analysis of $CD31^+$ myeloid cells in Ly6G-tdTomato-reporter mice, n = 2. (**C**) Hematoxylin-eosin staining of dLN 24 hours after administration of Nuvaxovid, n = 2. Arrows point to eosinophilic granulocytes. Scale bar: 20 µm. (**D**) Flow cytometry gating strategy for eosinophil identification [used in Fig. 8A (the visualized plots are the same as in Fig. 8A), fig. S10, E and F, and fig. S11C, I to K]. (**E** and **F**) Flow cytometry analyses of Siglec-F^+ eosinophil frequency and numbers in (E) blood and (F) at the muscle injection site in naïve and vaccine-primed mice, n = 4 to 12 mice per group. (**G**) Confocal images of Siglec-F (magenta) and CD31 (green) in Nuvaxovid-dLNs, n = 2 LNs per group. Scale bars: 50 µm. (**H**) Confocal images of Siglec-F (magenta), Ki67 (cyan) and DAPI (blue) in Nuvaxovid-dLNs, n = 2. Scale bar: 50 µm. (**I** and **J**) Confocal images from multi-tissue vibratome samples of ProxTom reporter mouse (LECs in green) stained for (I) Siglec-F (magenta) and (J) Siglec-F (magenta) and CD31 (blue) in Nuvaxovid-dLNs, n = 2. LV, lymphatic vessel; MS, medullary sinus; HEV, high-endothelial venule; P, parenchyma; SCS, subcapsular sinus. Scale bars: (I) 200 µm in the main figure and 50 µm in the zoom-ins and (J) 50 µm. All data (A to J) are obtained from i.m. vaccinated mice, are from (A) 4, (B and C, G to J), 1 to 2, or (E and F) 2 to 3 independent experiments and are presented as means ± SD. Statistical significance was tested using (E and F) Kruskal–Wallis *H*. n.s., not significant.

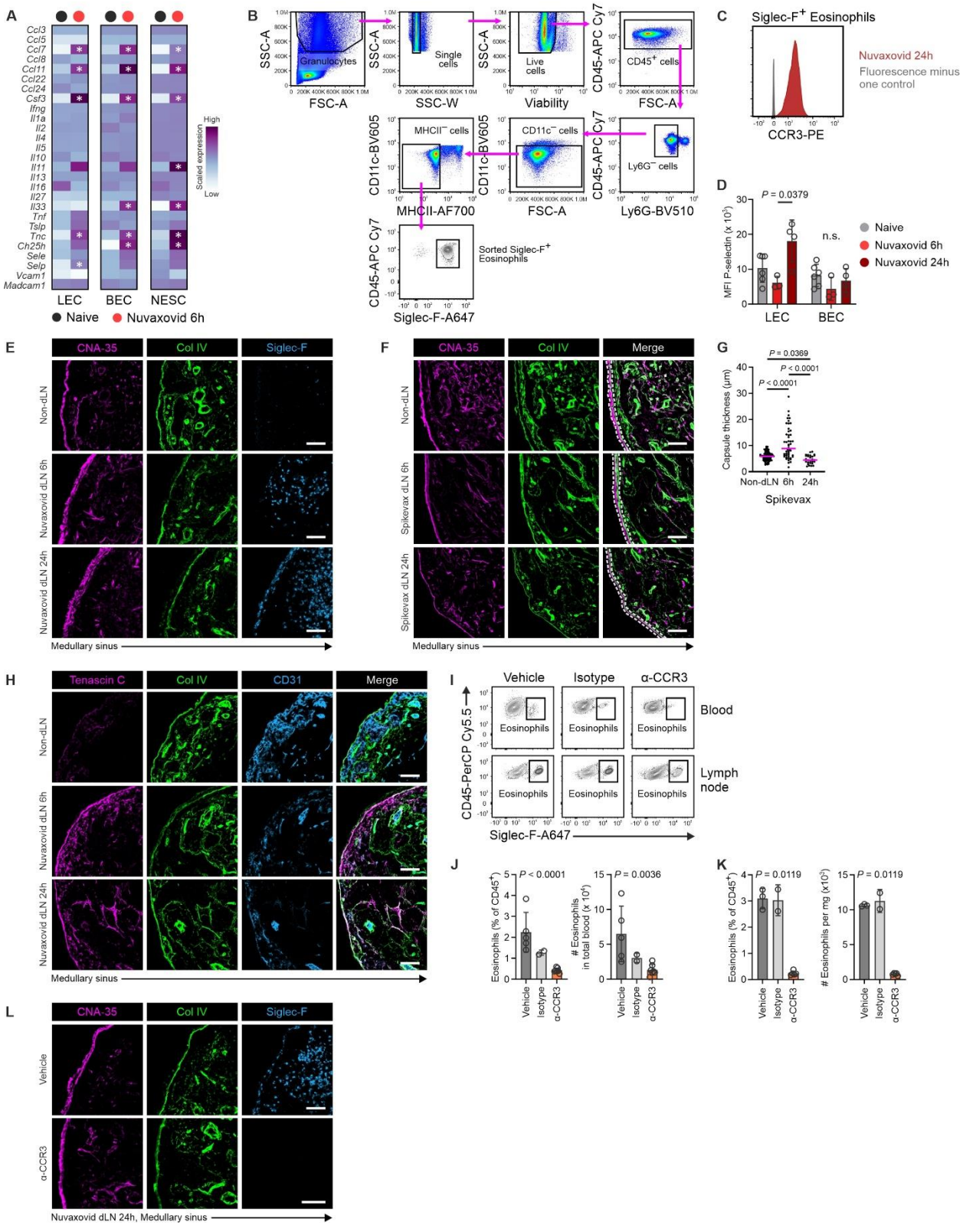
A
Ccl3
Ccl5
Ccl7
Ccl8
Ccl11
Ccl22
Ccl24
Csf3
Ifng
Il1a
Il2
Il4
Il5
Il10
Il11
Il13
Il16
Il27
Il33
Tnf
Tslp
Tnc
Ch25h
Sele
Selp
Vcam1
Madcam1
High
Scaled expression
Low
LEC
BEC
NESC
Naive
Nuvaxovid 6h
B
SSC-A
FSC-A
Granulocytes
SSC-W
Single cells
Viability
Live cells
CD45-APC Cy7
CD45+ cells
CD11c-BV605
MHCII− cells
MHCII-AF700
CD11c− cells
FSC-A
Ly6G− cells
Ly6G-BV510
Sorted Siglec-F+ Eosinophils
Siglec-F-A647
C
Siglec-F+ Eosinophils
Nuvaxovid 24h
Fluorescence minus one control
CCR3-PE
D
P = 0.0379
n.s.
MFI P-selectin (x 10³)
Naive
Nuvaxovid 6h
Nuvaxovid 24h
LEC
BEC
E
CNA-35
Col IV
Siglec-F
Non-dLN
Nuvaxovid dLN 6h
Nuvaxovid dLN 24h
Medullary sinus
F
CNA-35
Col IV
Merge
Non-dLN
Spikevax dLN 6h
Spikevax dLN 24h
Medullary sinus
G
P = 0.0369
P < 0.0001
P < 0.0001
Capsule thickness (µm)
Non-dLN
6h
24h
Spikevax
H
Tenascin C
Col IV
CD31
Merge
Non-dLN
Nuvaxovid dLN 6h
Nuvaxovid dLN 24h
Medullary sinus
I
Vehicle
Isotype
α-CCR3
Blood
Lymph node
Eosinophils
CD45-PerCP Cy5.5
Siglec-F-A647
J
P < 0.0001
P = 0.0036
Eosinophils (% of CD45+)
Eosinophils in total blood (x 10⁴)
Vehicle
Isotype
α-CCR3
K
P = 0.0119
P = 0.0119
Eosinophils (% of CD45+)
Eosinophils per mg (x10³)
Vehicle
Isotype
α-CCR3
L
CNA-35
Col IV
Siglec-F
Vehicle
α-CCR3
Nuvaxovid dLN 24h, Medullary sinus

Fig. S11. Eosinophil infiltration modulates dLN stroma after Nuvaxovid vaccination. (**A**) Heatmaps of eosinophil-related mRNAs in naïve LNs and Nuvaxovid-dLNs. (**B**) Gating strategy for sorting eosinophils from Nuvaxovid-dLNs. (**C**) Flow cytometry analysis of CCR3 on eosinophils in Nuvaxovid-dLNs, n = 2. (**D**) Flow cytometry quantification of P-selectin expression in naïve LN and Nuvaxovid-dLNs, n = 3 to 6 samples per group. (**E**) Single channels (from merged panes in Fig. 8H) of CNA-35 (magenta), collagen IV (Col IV, green), and Siglec-F (blue) in Nuvaxovid-dLNs, n = 4 to 8 LNs per group. Scale bars: 50 μm. (**F**) Confocal images of CNA-35 (magenta) and Col IV (green) in Spikevax-non-dLNs and -dLNs, n = 3 to 5 LNs per group. The dashed lines indicate capsule borders. Scale bars: 50 μm. (**G**) Quantification of capsular thickness [from (F)], n = 3 to 5 LNs per group, each dot represents one measurement. (**H**) Confocal images of tenascin C (magenta), Col IV (green), and CD31 (blue) in Nuvaxovid-non-dLNs and -dLNs, n = 4 to 6 LNs per group. Scale bars: 50 μm. (**I** to **K**) Flow cytometry (I) plots and quantifications of eosinophils in (J) blood and (K) Nuvaxovid-dLNs in α-CCR3 antibody pretreated mice (eosinophil depletion) or controls, n = 2 to 7 mice. (**L**) Single channels (from merged panes in Fig. 8K) of CNA-35 (magenta), Col IV (green) and Siglec-F (blue) in Nuvaxovid-dLNs, n = 4 to 5 LNs. Scale bars: 50 μm. All data (A to L) are from i.m. immunized mice. Data are from (A) 30 LNs pooled from 15 mice from (C to L) 2 to 4 independent experiments and are presented as means ± SD. Statistical significance was tested using (J and K) Kruskal–Wallis *H* or (D and G) Kruskal–Wallis *H* with Dunn's post-hoc test. n.s., not significant.

Population	Naive	Vehicle	Spikevax	Comirnaty	Vaxzevria	Nuvaxovid
Cell numbers after QC	5315	5367	7289*	5706	3817	3368
LEC	1426	1222	1547	1179	1005	535
BEC	705	854	866	490	445	991
NESC	2686	2784	4438	3035	2013	4438
LEC subclustering						
SCS ceiling	523	484	576	337	337	204
SCS floor	414	299	354	288	193	162
Medullary sinus	420	366	498	454	404	148
Ccl19^{+}	44	35	79	40	32	10
BEC subclustering						
HEV	285	335	307	174	172	237
TrEC	83	110	114	71	56	103
Art	43	68	92	35	36	111
CapEC	115	125	137	91	79	247
Vena	15	15	22	12	10	34
Ccl19^{+}	29	31	64	28	22	108
NESC subclustering						
Capsule	188	126	239	246	95	353
TRC	471	503	857	566	391	760
Ccl19^{high} TRC	199	193	189	143	84	148
TBRC	477	522	569	407	278	572
IFRC	224	214	538	328	211	684
FDC	78	84	87	87	49	102
MRC	140	153	162	126	73	189
MedRC	416	395	923	536	423	700
Cd34^{+} stromal cells	95	147	170	105	77	143
Perivascular cells	165	204	230	114	107	273
Pericytes	13	19	29	14	15	35

Table S1.

Cell numbers for scRNA-seq populations. QC, quality control; LEC, lymphatic endothelial cell; BEC, blood endothelial cell; NESC, non-endothelial stromal cell; SCS, subcapsular sinus; HEV, high endothelial venule; TrEC, transitional endothelial cells; Art, arterial endothelial cells; CapEC, capillary endothelial cells; TRC, T zone reticular cells; TBRC, T–B border reticular cells; IFRC, inter-follicular reticular cells; FDC, follicular dendritic cells; MRC, marginal reticular cells; MedRC, medullary reticular cells. All data are from i.m. immunizations. * Cell number after QC for s.c. Spikevax sample is 9489.

Gene	LEC	BEC	NESC
Ccl7			0.7580525
Tmsb10	0.759836		
Ppia	0.742199		
Rpl35	0.714764		
mt-Atp6	−0.71497		
mt-Nd3	−0.82089	−0.9220589	−0.8906002
Cdk8	−1.22182	−1.4380964	−1.3366730
Hexb	−1.24442	−1.3854515	−1.3845850

Table S2.

Log_2 fold–change values for statistically significant (Wilcoxon rank sum test with Bonferroni-correction) differentially expressed protein coding genes in vehicle-vaccinated control vs naïve sample.

Antibody	Clone	Fluorophore/ conjugate	Source	Catalog number	RRID	Final concentration	Fixation	Application
Imaging								
Primary antibodies								
ACKR4	Polyclonal	-	Santa Cruz	sc-46835	AB_2087281	1 µg/ml	Acetone	IF
CCL11	Polyclonal	-	R&D Systems	AF420-SP	AB_354486	5 µg/ml	PFA	IF
CCL21	Polyclonal	-	R&D Systems	AF457	AB_2072083	8 µg/ml	No fixing	IF
CD31/PECAM-1	Polyclonal	-	R&D Systems	AF3628	AB_2161028	5 µg/ml	PFA	FISH, Vibratome
CD36	Polyclonal	-	R&D Systems	AF2519	AB_2228767	10 µg/ml	Acetone	IF
CD321 (F11R)/JAM-A	H202-106	-	Invitrogen	MA5-28179	AB_2745155	10 µg/ml	PFA	Vibratome
Collagen I	Polyclonal	-	Millipore	AB765P	AB_92259	10 µg/ml	No fix	IF
CD144/VE-Cadherin	Polyclonal	-	R&D Systems	AF1002	AB_2077789	5 µg/ml	Acetone	IF
LYVE-1	Polyclonal	-	ReliaTech GmbH	103-PA50	AB_2783787	10 µg/ml	Acetone	IF
MARCO	ED31	-	Biorad	MCA1849T	AB_322923	5 µg/ml	Acetone	IF
RFP (Anti-tdTomato)	Polyclonal	-	Rockland	600-401-379	AB_2209751	1.05 µg/ml	PFA	Vibratome
SARS2-S1-His	Polyclonal	-	(*80*)	-	-	1:1000	PFA	IF, Vibratome
Tenascin C	578	-	R&D Systems	MAB2138	AB_2203818	2,5 µg/ml	Acetone	IF
Secondary antibodies								

Donkey anti-Goat IgG (H+L) Highly Cross-Adsorbed	Polyclonal	Alexa Fluor Plus 488	Invitrogen	A32814	AB_2762838	5 µg/ml	Acetone, PFA	IF, Vibratome
Donkey anti-Goat IgG (H+L)	Polyclonal	Alexa Fluor 647	Invitrogen	A21447	AB_2535864	5 µg/ml	PFA	FISH
Donkey anti-rabbit IgG (H+L) Highly Cross-Adsorbed	Polyclonal	Alexa Fluor Plus 647	Invitrogen	A31573	AB_2536183	5 µg/ml	PFA	Vibratome
Donkey anti-rabbit IgG (Heavy chain)	Polyclonal	Alexa Fluor 647	Invitrogen	A27040	AB_2536101	5 µg/ml	Acetone	IF
Goat anti-rabbit IgG (H+L) Highly Cross-Adsorbed	Polyclonal	Alexa Fluor 488	Invitrogen	A11034	AB_2576217	5 µg/ml	PFA	IF
Goat anti-rabbit IgG (H+L) Highly Cross-Adsorbed	Polyclonal	Alexa Fluor 546	Invitrogen	A11035	AB_2534093	5 µg/ml	Acetone, PFA	IF, Vibratome
Goat anti-rat IgG (H+L) Cross-Adsorbed	Polyclonal	Alexa Fluor 546	Invitrogen	A11081	AB_2534125	5 µg/ml	Acetone, PFA	IF, Vibratome
Fluorochrome conjugated antibodies								
CD21/CD35	7E9	Alexa Fluor 647	BioLegend	123423	AB_2629577	10 µg/ml	PFA	IF
CD31	MEC13.3	Alexa Fluor 488	BioLegend	102514	AB_493413	10 µg/ml	Acetone	IF
CD31	MEC13.3	Alexa Fluor 594	BioLegend	102520	AB_2563319	10 µg/ml	Acetone, PFA	IF
CD31	390	Alexa Fluor 647	BioLegend	102416	AB_493410	10 µg/ml	PFA	IF
CD206	C068C2	Alexa Fluor 488	BioLegend	141710	AB_10900445	5 µg/ml	Acetone	IF
CD274	10F.9G2	APC	BioLegend	124312	AB_10612741	10 µg/ml	Acetone	IF

Collagen IV	Polyclonal	Alexa Fluor 488	Southern Biotech	1340-30	AB_2794738	4 µg/ml	Acetone, PFA	IF, Vibratome
ER-TR7	ER-TR7	DyLight 405	Novus Biologicals	NB100-64932V	AB_3167548	10 µg/ml	Acetone	IF
F4/80	Cl:A3-1	Alexa Fluor 647	Biorad	MCA497A647	AB_323931	11 µg/ml	PFA	IF
Ki67	B56	Alexa Fluor 555	BD Biosciences	558617	AB_647108	5 µl/test	Acetone	IF
Siglec-F	E50-2440	Alexa Fluor 647	BD Biosciences	562680	AB_2687570	10 µg/ml	Acetone, PFA	IF, Vibratome
SMA	1A4	Cy3	Sigma	C6198	AB_476856	1:200	PFA	IF
In vivo administration								
CCR3	6S2-19-4	-	BioXcell	BE0316	AB_2754554	300 µg/i.v. injection	-	IF, Flow Cyt
CCR3 isotype control	LTF-2	-	BioXcell	BE0090	AB_1107780	300 µg/i.v. injection	-	IF, Flow Cyt
CD31	MEC13.3	Alexa Fluor 488	BioLegend	102514	AB_493413	2 µg/s.c. injection	-	IF
CD45	30-F11	Alexa Fluor 488	BioLegend	103122	AB_493532	5 µg/s.c. injection	-	Flow Cyt
Flow Cytometry								
B220	RA3-6B2	BV421	BD Biosciences	562922	AB_2737894	0.5 µg/ml	-	Flow Cyt
B220	RA3-6B2	PE-CF594	BD Biosciences	562290	AB_11151901	1 µg/ml	-	Flow Cyt
CCR3	J073E5	PE	BioLegend	144505	AB_2561533	1 µg/ml	-	Flow Cyt
CD3	17A2	PE	BD Biosciences	555275	AB_395699	1 µg/ml	-	Flow Cyt
CD4	GK1.5	BV421	BioLegend	100437	AB_10900241	0.125 µg/ml	-	Flow Cyt
CD8a	53-6.7	PE Cy7	BD Biosiences	552877	AB_394506	1 µg/ml	-	Flow Cyt
CD11b	M1/70	BD Horizon BB515	BD Biosciences	564454	AB_2665392	0.4 µg/ml	-	Flow Cyt
CD11c	N418	BV711	BioLegend	117349	AB_2563905	1 µg/ml	-	Flow Cyt
CD11c	N418	BV605	Biolegend	117333	AB_11204262	0.25 µg/ml	-	Flow Cyt
CD16/CD32	2.4G2	-	BioXCell	BE0307	AB_ 2736987	92.4 µg/ml	-	Flow Cyt
CD31	390	BV711	BioLegend	102449	AB_2860594	1 µg/ml	-	Flow Cyt
CD45	30-F11	PerCP-Cy5.5	BD Biosciences	550994	AB_394003	1 µg/ml	-	Flow Cyt
CD45	30-F11	APC-Cy7	BD Biosciences	561037	AB_396774	1 µg/ml	-	Flow Cyt
CD62P	RB40.34	BV650	BD Biosciences	752963	AB_2917918	2 µg/ml	-	Flow Cyt

CD69	H1-2F3	FITC	Cell Signaling	39443S	-	2 µg/ml	-	Flow Cyt
CD193 (CCR3)	J073ES	PE	BioLegend	144505	AB_2561533	1 µg/ml	-	Flow Cyt
CD274	10F.9G2	APC	BioLegend	124312	AB_10612741	2 µg/ml	-	Flow Cyt
I-A/I-E (MHCII)	M5-114.15.2	Alexa Fluor 700	BioLegend	107622	AB_493727	2.5 µg/ml	-	Flow Cyt
Ly6G	1A8	BV510	BioLegend	127633	AB_2562937	1 µg/ml	-	Flow Cyt
Podoplanin	8.1.1	PE-Cy7	BioLegend	127412	AB_10613648	2 µg/ml	-	Flow Cyt
Siglec-F	E50-2440	Alexa Fluor 647	BD Biosciences	562680	AB_2687570	1 µg/ml	-	Flow Cyt
Ter119	Ter119	BV785	BioLegend	116245	AB_2650921	1 µg/ml	-	Flow Cyt
Ter119	Ter119	PE/Dazzle594	BioLegend	116244	AB_2565872	1 µg/ml	-	Flow Cyt

Table S3.
Antibodies and their final concentrations.

Cluster	Genes for identification
LEC	
CD36^{+} *Ltb*$^{+}$ SCS ceiling	*Ackr4*$^{+}$ *CD36*$^{+}$ *Ltb*$^{+}$
Fgl2^{+} *Ltb*$^{–}$ SCS ceiling	*Ackr4*$^{+}$ *Fgl2*$^{+}$ *Ltb*$^{–}$
CD36^{+} *Ltb*$^{–}$ SCS ceiling	*Ackr4*$^{+}$ *CD36*$^{+}$ *Ltb*$^{–}$
SCS floor	*Madcam1*$^{+}$ *Coch*$^{+}$ *Itga2b*$^{+}$ *Lyve1*$^{+}$
Marco^{+} Medullary sinus	*Itga2b*$^{+}$ *Mrc1*$^{+}$ *Lyve1*$^{+}$ *Marco*$^{+}$
Marco^{lo} Medullary sinus	*Itga2b*$^{+}$ *Mrc1*$^{+}$ *Lyve1*$^{+}$ *Marco*^{lo}
Ifnb1^{+} Medullary sinus (specific for Vaxzevria)	*Itga2b*$^{+}$ *Mrc1*$^{+}$ *Lyve1*$^{+}$ *Marco*$^{+}$ *Ifnb1*$^{+}$
Ccl19^{+} LECs	*Prox1*$^{+}$ *Ccl19*$^{+}$
BEC	
High endothelial venules (HEV)	*Glycam1*^{hi} *Chst4*$^{+}$ *Selp*$^{+}$
Venules	*Selp*$^{+}$ *Chst4*$^{–}$ *Vwf*$^{+}$
Transitional endothelial cells (TrEC)	*Glycam1*$^{+}$ *Chst4*$^{–}$ *Vwf*$^{–}$
Capillary endothelial cells (CapEC)	*Ly6c1*$^{+}$ *Podxl*$^{–}$ *Fbln5*$^{–}$
Arterial endothelial cells (Art)	*Ly6c1*$^{+}$ *Podxl*$^{+}$ *Fbln5*$^{+}$
Ccl19^{+} BEC	*Pecam1*$^{+}$ *Ccl19*$^{+}$ *C3*$^{+}$
NESC	
Capsule	*Des*$^{–}$ *Cd34*$^{+}$
T zone reticular cells (TRC)	*Ccl19*$^{+/lo}$ *Ccl21a*$^{+}$ *Fmod*^{lo} *Bst1*$^{+/lo}$ *Dpt*$^{+}$ *Stc1*^{lo}
Ccl19^{hi} TCRs	*Ccl19*^{hi} *Ccl21a*^{hi} *Grem1*$^{+}$ *Fmod*$^{+}$ *Bst1*$^{+}$
T–B border reticular cells (TBRC)	*Ccl19*$^{+}$ *Ccl21a*^{hi} *Grem1*$^{+}$ *Fmod*$^{+}$ *Bst1*$^{+}$ *Dpt*$^{+}$ *Il7*$^{+}$ *Stmn2*$^{+}$
Interfollicular reticular cells (IFRC)	*Ccl19*^{lo} *Ccl21a*^{lo} *Grem1*$^{–}$ *Fmod*$^{–}$ *Stc1*$^{+}$
Follicular dendritic cells (FDC)	*Cr2*$^{+}$ *Madcam1*$^{+}$ *Cxcl13*^{hi} *Fcer2a*$^{+}$ *Fcgr2b*$^{+}$
Marginal reticular cells (MRC)	*Cr2*$^{+}$ *Madcam1*$^{+}$ *Cxcl13*^{hi} *Fcer2a*$^{–}$ *Fcgr2b*$^{+}$
Medullary sinus reticular cells (MedRC)	*Inmt*$^{+}$ *Ccl19*$^{+/lo}$ *Ccl21a*$^{+}$ *Fmod*^{lo} *Cxcl12*$^{+}$ *Lum*$^{+}$

Cd34^{+} stromal cells	*Ccl19*$^{+}$ *Cd34*$^{+}$ *Inmt*$^{+}$ *Ly6c1*$^{+}$ *Dpt*$^{+}$ *Lum*$^{+}$ *Des*$^{+}$
Perivascular cells (Perivasc)	*Pdgfra*$^{-}$ *Pdgfrb*$^{+}$ *Rgs4*$^{+}$ *Notch3*$^{+}$
Pericytes	*Pdgfra*$^{-}$ *Pdgfrb*$^{+}$ *Cspg4*$^{+}$ *Itga7*$^{+}$

Table S4.
Signature genes used for LEC, BEC and NESC subcluster identification.

Movies S1 and S2.
Panoramic view of early S protein expression in sinusoidal LECs after gene-based COVID-19 vaccinations. **Movie S1.** 3D reconstruction of S protein (cyan) and endothelial marker CD31 (magenta) immunostaining from the subcapsular sinus (SCS) of a draining lymph node (dLN) 6 hours after i.m. administration of Spikevax. **Movie S2**. 3D reconstruction of S protein (cyan) and endothelial marker CD31 (magenta) immunostaining from the medullary sinus (for the first 10 s CD31 signal only) of a draining lymph node (dLN) 6 hours after i.m. administration of Spikevax. Both movies are generated from confocal images of multi-tissue vibratome samples.

Movies S3 to S5.
Junction morphology of LEC–LEC contacts in the ceiling and floor of SCS. **Movie S3 and Movie S4.** 3D reconstruction of endothelial marker CD31 staining (white) from the subcapsular sinus (SCS) of naïve LN. **Movie S5**. 3D reconstruction of endothelial marker CD31 staining (white) from the subcapsular sinus (SCS) of a dLN 6 hours after i.m. administration of Vaxzevria. Movie S3 highlights $CD31^+$ junctions in the SCS ceiling LECs (visualized in fluorescence intensity mode), whereas movies S4 and S5 show SCS floor LEC–LEC junctions (visualized in volumetric mode).

Movies S6 to S8.
Induction of tight junction protein JAM-A in SCS after vaccination. **Movie S6.** 3D reconstruction of endothelial markers CD31 (green) and JAM-A (magenta) staining from the subcapsular sinus (SCS) of naïve LN. **Movie S7**. 3D reconstructions of endothelial markers CD31 (green) and JAM-A (magenta) staining from the subcapsular sinus (SCS) of a dLN 6 hours after i.m. administration of Vaxzevria. **Movie S8**. 3D reconstruction of endothelial marker CD31 staining (white) from the subcapsular sinus (SCS) dLN 24 hours after i.m. administration of Vaxzevria. Dashed line, SCS LECs ceiling.

Movies S9 and S10.
Panoramic view of eosinophil infiltration in Nuvaxovid-dLNs. **Movie S9**. 3D reconstructions of Siglec-F^+ eosinophils (magenta) and $ProxTom^+$ lymphatics (white) visualized in multi-tissue vibratome samples of draining LNs 6 hours after i.m. administration of Nuvaxovid. **Movie S10**. 3D reconstructions of Siglec-F^+ eosinophils (magenta) and $ProxTom^+$ lymphatics (white) visualized in multi-tissue vibratome samples of draining LNs and 24 hours after i.m. administration of Nuvaxovid. Both movies have been constructed from several confocal images. Movies demonstrate the prominent eosinophil infiltration especially within the $Prox1^+$ medullary sinus and show the presence of extranodal eosinophils in the LN surrounding tissue

Data file S1. (separate file)
Transcriptomic changes in interferon-inducible genes in LECs, BECs, and NESCs.

Data file S2. (separate file)
Raw data file.

Main Text:

INTRODUCTION

The lymph node (LN) stromal component plays a central role in the orchestration of effective adaptive immune responses. Stromal cells, including blood vascular endothelial (BECs), lymphatic endothelial cells (LECs), and fibroblastic reticular cells (FRCs), provide critical physical migration pathways and chemotactic signals, which guide lymphocyte and dendritic cell (DC) traffic to and within the tissue (*1-4*). The stroma also secretes growth-promoting factors, which regulate proliferation and survival of immune cells, and provides a structural scaffold for LN expansion during immune reactions (*1-4*). Moreover, all lymph-borne material, including soluble antigens and free particulate material (e.g., extracellular vesicles, microbes, and nanoparticles) drain to subcapsular sinus (SCS) and medullary sinuses of the draining LNs (dLNs), which are covered by LECs (*5*). Sinusoidal LECs can scavenge (*6*), present (*7, 8*), or archive (*9, 10*) incoming free antigens. Prior work has shown that soluble antigens can also be transferred to LN-resident antigen-presenting cells (APCs) within seconds. This process occurs by an active fluid-phase vesicular transcytosis pathway through LECs (*11*) and via the collagen fibril–based reticular conduit system formed by FRCs (*12-15*).

Over five billion people have been immunized with traditional protein subunit vaccines or gene-based adenovirus vector and mRNA vaccines targeting SARS-CoV-2 spike (S) protein (*16*). Whether responses within the dLN stroma are triggered by the different vaccine types remain largely unknown. Protein vaccinations rely on the direct injection of the recombinant S protein into the muscle (*16*). In mRNA vaccines, lipid nanoparticles (LNPs) merge with cell membranes at the injection site and release the encapsulated in vitro–transcribed, RNAse-resistant mRNA molecules into the cytoplasm for translation (*16-19*). Adenovirus vector vaccines use live non-replicating viral particles to locally transduce muscle cells (*16, 20*). The injected or locally translated immunogen is taken up by DCs, which migrate to the dLN within approximately 8 to 12 hours for antigen presentation (*21, 22*). The activation of migratory DCs is augmented by adjuvants (e.g., aluminum salts and bark-derived saponins) in protein vaccines and by nucleotides, LNPs, and adenovirus gene transfer vehicles in gene-based vaccines (*16, 23-25*).

Here, we report that inoculation of mice with approved mRNA and adenovirus vector vaccines against COVID-19 results in stromal expression of immunogenic S protein in the dLN within 6 hours. We observed that gene-based and nanoparticle protein-based vaccines induced vaccine-specific stromal responses, which functionally altered immune responses by affecting scavenging, antigen filtering, chemokine gradient formation, and eosinophil infiltration in the dLNs. Our data highlight early stromal responses to different COVID-19 vaccines, which reprogram the cellular landscape of dLNs before the arrival of migratory DCs.

RESULTS

Gene-based COVID-19 immunizations induce stromal cell-specific S protein positivity in dLNs

To study the early response of LN stromal cells to different COVID-19 vaccines, we administered subcutaneous (s.c.) immunizations of a clinically available adenovirus vector vaccine (Vaxzevria from AstraZeneca (*26*)) or an mRNA vaccine (Spikevax from Moderna (*27*), or Comirnaty from Pfizer-BioNTech (*28*)) to the footpad of wild-type mice (Fig. 1A). Immunohistological analyses

showed S protein reactivity in the LEC-lined subcapsular and medullary sinus systems of popliteal dLNs after 2 hours. All three vaccines achieved maximal S protein signal strength in both sinus systems at 6 hours post-inoculation. S protein reactivity was maintained at 30 hours by the mRNA vaccines, but not the adenovirus vaccine (Fig. 1, B and C, and fig. S1, A to C). A few ERTR7^{+} reticular cells in the parenchyma showed low signal for S protein after mRNA vaccination (fig. S1D), whereas most CD31^{hi} BECs remained S protein–negative. S protein signal in the dLNs of immunized mice was local and specific, since we did not observe it in the contralateral non-draining popliteal LNs of the vaccinated mice or LNs of naïve mice (fig. S1E).

To accurately recapitulate clinical COVID-19 vaccination in our mouse models, we treated mice intramuscularly (i.m.) with one of the three gene-based vaccines or with a nanoparticle-containing protein subunit vaccine (Nuvaxovid from Novavax (*29*)) (Fig. 1A). We observed slower drainage of lymph-borne particles to dLNs after i.m. vaccinations compared with the s.c. administration route when we used Spikevax mRNA-LNP vaccine labeled with a fluorescent marker (fig. S1F). We observed twofold popliteal dLN expansion 6 hours after i.m. vaccination (fig. S1G), confirming initiation of an immune response at this early time point. There were decreased S protein signals in dLNs with all three gene-based vaccines after i.m. vaccinations (fig. S1H) compared to the corresponding s.c. immunizations. However, we also detected the vaccine type–selective, LEC-dominant S protein reactivity among different stromal cells after i.m. immunization with gene-based vaccines. Moreover, we found only minimal S protein positivity after i.m. protein vaccination (fig. S1H).

To obtain a more detailed view of the S protein localization in the narrow and easily collapsing sinuses of the dLN after i.m. immunizations, we dissected the dLN intact with all surrounding tissues for staining and 3D reconstructions of high-resolution confocal image stacks (fig. S1I). Using quantitative image analyses of the SCS after mRNA-LNP Spikevax immunization, we found that abundant S protein reactivity was restricted to floor LECs, compared with ceiling LECs, which showed variable S protein signal (Fig. 1D; fig. S1J; and movie S1). Comirnaty mRNA-LNP vaccination showed the strongest S protein reactivity in the SCS and reactivity was primarily restricted to SCS floor LECs. By contrast, deposition of S protein in SCS LECs was undetectable following adenovirus-based Vaxzevria and protein-based Nuvaxovid vaccination (Fig. 1D and fig. S1J). In the medullary sinus, S protein signal was observed in CD31^{+} LECs after mRNA-LNP (Spikevax and Comirnaty) and protein (Nuvaxovid) immunization (Fig. 1D; fig. S1J; and movie S2). All gene-based vaccinations produced strong S protein positivity of nonendothelial medullary sinus leukocytes (Fig. 1D and fig. S1K). Thus, S protein rapidly appears in distinct dLN stromal cell types after immunization with COVID-19 gene-based vaccines.

Gene-based vaccines transfect dLN stromal cells in vivo

We used scRNA-seq analyses to determine whether spike mRNA and early transcriptomic changes are present in dLN stromal cells 6 hours post-immunization (i.m.) (Fig. 1A and table S1). Using uniform manifold approximation and projection (UMAP) presentation for dimensionality reduction and visualization, we observed clear clustering of the three main stromal cell types, identified as LECs (*30, 31*), BECs (*32, 33*), and nonendothelial stromal cells (NESCs) (*34-36*) in pooled analyses of dLN samples from mice that were either unvaccinated (naïve), vehicle-vaccinated, or vaccinated with any of the four different COVID-19 vaccines (Fig. 2A and fig. S2, A to C). After immunization with mRNA-LNP Spikevax and Comirnaty vaccinations, we

observed medium to high expression of spike mRNA in 31 to 48% of LECs, but only in 2 to 7% of BECs and NESCs (Fig. 2B). By contrast, few LECs, BECs, or NESCs were positive for spike mRNA after adenoviral Vaxzevria vaccination (Fig. 2B). When Spikevax was administered s.c., the order of spike mRNA positivity (both the level of expression and the percentage of positive cells) from highest to lowest was in LECs, NESCs, and BECs (fig. S2D). Spike mRNA expression was higher in all stromal cell populations after s.c. immunization compared to i.m. immunization (fig. S2D). Even though both scRNA-seq analyses and imaging data showed that i.m. immunization results in lower spike mRNA and S protein levels in dLN stromal cells than s.c. immunizations, we administered COVID-19 vaccines i.m. in all subsequent studies to better reflect the clinical immunization practice.

To dissect the cell types positive for spike mRNA after i.m. vaccinations in greater detail, we reclustered each of the three main stromal cell populations separately. Based on the expression of established signature genes within the prospero homeobox 1 (*Prox1)*$^+$ LECs (*30*, *31*), we identified different LEC subclusters, including SCS ceiling, SCS floor, medullary, and C-C motif chemokine ligand 19 (*Ccl19)*$^+$ LEC subpopulations (Fig. 2C and fig. S2E). Within the ceiling LEC cluster, we defined three distinct subpopulations characterized by differential *Cd36,* lymphotoxin beta (*Ltb)* and fibrinogen-like protein 2 (*Fgl2)* expression (Fig. 2C). The medullary LEC population was further dissected into two major subpopulations based on *Marco* (macrophage receptor with collagenous structure) expression. Previously identified pentraxin 3 (*Ptx3)*$^+$ medullary LECs (*30, 31*) were included within the *Marco*^{lo} cluster. Spikevax mRNA was expressed at medium to high levels in 64 to 75% of floor and medullary LECs. By contrast, ceiling LEC and *Ccl19*$^+$ LEC populations showed weaker spike mRNA expression (Fig. 2D). Comirnaty mRNA-LNP vaccination resulted in medium to high spike mRNA expression in the majority of floor LECs. By contrast, only < 21% of LECs in the ceiling, medullary, and *Ccl19*$^+$ clusters had medium to high spike mRNA expression (Fig. 2D). After adenoviral Vaxzevria vaccination, few spike mRNA–positive cells were observed across all LEC subclusters (Fig. 2D).

To directly visualize the endothelial transfection after mRNA vaccinations, we performed fluorescence in situ hybridization (FISH) with custom-made spike mRNA-specific probes. High-resolution imaging of SCS LECs revealed the localization of spike mRNA within CD31$^+$ endothelial cells after both Spikevax or Comirnaty mRNA vaccinations (Fig. 2E). The FISH signal was neither detected in the contralateral LNs of vaccinated mice nor in the LNs of unvaccinated mice (Fig. 2E and fig. S2, F to G). When BECs (*32*) and NESCs (*34-36*) were reclustered, we observed the highest spike RNA levels after mRNA vaccination with Spikevax or Comirnaty in follicular DCs, marginal reticular cells, CD34$^+$ stromal cells, and capsular cells (Fig. 2, F and G). FISH analyses revealed spike mRNA expression in CD21/CD35$^+$ follicular DCs in dLNs from vaccinated mice (fig. S3G). In scRNA-seq analyses, all other BEC and NESC types were predominantly spike mRNA–negative or showed low expression of spike mRNA (Fig. 2, F and G). dLN leukocytes (lymphocytes, DCs, and monocytes/macrophages) had lower spike mRNA counts than LECs (fig. S3H). Thus, there is direct and robust cell- and vaccine-specific in vivo transfection of stromal cells in the dLN within 6 hours post-vaccination, which was particularly prominent in lymph-exposed floor LECs after mRNA vaccinations.

Different COVID-19 immunizations induce distinct early transcriptomic changes in dLN stromal cells

To study the early stromal cell responses to different COVID-19 vaccines, we compared scRNA-seq data from the dLNs of i.m. vaccinated mice with those of naive control mice by analyzing the whole transcriptome and differentially expressed genes (DEGs) at 6 hours post-immunization. Similarity plots showed that the stromal responses induced by Vaxzevria (adenovirus vaccine) and Comirnaty (mRNA vaccine) were more similar in LECs, BECs, and NESCs than those induced by the two different mRNA vaccines (Fig. 3A). Each vaccine induced multiple vaccine-specific DEGs across stromal cell types (Fig. 3B and fig. S4, A to D). The vaccines induced 520 to 805 DEGs in LECs, of which only 18.3% were shared by all four vaccine types and 19.0% were shared by the three gene-based vaccines (Spikevax, Comirnaty, and Vaxzevria) (Fig. 3B). The stromal responses induced by the protein vaccine (Nuvaxovid) had the lowest similarity to the other vaccine types and the highest number of unique DEGs (Fig. 3, A and B, and fig. S4D). Comparison of unvaccinated and vehicle-injected mice revealed only few (< 5) protein-encoding DEGs (table S2), indicating that local injection pressure or volume did not induce any major transcriptomic alterations of the stromal cells. Moreover, SCS ceiling LECs from Spikevax-immunized mice expressing spike mRNA at high or medium levels had multiple DEGs compared with spike mRNA–negative cells (fig. S4, E to G). Thus, gene-based vaccines can cause direct intrinsic changes in transfected stromal cells in addition to cell-extrinsic vaccine-induced inflammatory responses.

The differences in stromal cell responses observed between protein- and gene-based vaccines were evident in gene pathway analyses (Fig. 3C and fig. S4H). All gene-based vaccines induced transcription of multiple interferon-inducible genes, whereas the protein vaccine up-regulated fewer and different genes (fig. S4I and data file S1). Additionally, immunization with adenoviral Vaxzevria vaccine generated a specific LEC cluster expressing interferon beta 1 (*Ifnb1*) as a distinctive marker (Fig. 2C). These cells had a medullary LEC identity, but were clearly distinct from the conserved *Marco*^{hi} and *Marco*^{lo} medullary LEC subclusters (Figs. 2C and 3D). FISH analyses verified that *Ifnb1*$^{+}$ LECs often intermingled with *Ifnb1*$^{-}$ LECs at the outer border of the medullary sinus (Fig. 3E).

Gene pathway analyses of antigen handling processes showed that all gene-based vaccines induced *Tap1* (transporter associated with antigen processing 1) and *Tapbp* (TAP-binding protein) expression in LECs. The adenovirus vaccine Vaxzevria selectively induced major histocompatibility complex class I and β2-microglobulin genes. The protein vaccine Nuvaxovid affected none of these genes (fig. S4J). All gene-based vaccines showed strong upregulation of *Cd274*, encoding programmed death-ligand 1 (PD-L1) (Fig. 3F). Vaxzevria induced the strongest expression of *Cd274*, whereas the protein vaccine had only minor effects. PD-L1 protein induction by Vaxzevria was visible in quantitative immunohistological analyses (Fig. 3, G and H). Kinetic flow cytometric analyses of PD-L1 surface expression on stromal cell subsets at 0, 6, and 24 hours verified selective PD-L1 induction by Vaxzevria, but not by Nuvaxovid (Fig. 3I and fig. S5A). PD-L1 protein and mRNA induction were more prominent in LECs than in BECs or NESCs (Fig. 3I). Thus, compared to gene-based vaccines, the protein vaccine Nuvaxovid has minimal effects on molecules involved in antigen handling and costimulation in stromal cells of dLNs.

To determine whether LN stromal cells can modulate lymphocyte activation after vaccination, we developed a surrogate in vitro assay to exclude the contribution of migratory and LN-resident professional APCs, such as DCs and macrophages (Fig. 3J). We isolated stromal cells (CD45^{-}Ter119^{-} cells) from naive LNs and exposed them to Vaxzevria in vitro to mimic vaccinations (fig. S5B). This resulted in robust expression of the S protein in a subset of cells (Fig.

3K). When lymphocytes isolated from naïve LNs were cocultured with Vaxzevria-exposed stromal cells for 1 day, we found that CD69, a marker of early T cell activation, was expressed to a greater degree in a larger percentage of CD8 T cells compared with lymphocytes cultured with unvaccinated stromal cells or without stromal cells (Fig. 3, L and M, and fig. S5C). Thus, vaccination-induced changes in stromal cells potentially modulate T cell activation.

mRNA-LNP immunization reduces LEC-mediated scavenging in dLN sinus

As lymph-borne vaccines primarily come in contact with the LECs of LN sinuses, we analyzed vaccine-induced changes in sinus-dependent functions. When studying scavenger receptors (*37*), we observed modifications in their transcription in LECs after all vaccinations. *Cd36* and stabilin 2 (*Stab2),* the major scavenger receptors expressed in SCS ceiling LECs, were down-regulated 6 hours after i.m. immunization with each of the COVID-19 vaccines. In medullary LECs, macrophage scavenger receptor 1 (*Msr1*), *Marco*, mannose receptor C-type 1 (*Mrc1*), and *Stab2* were down-regulated, whereas oxidized low-density lipoprotein receptor 1 (*Olr1*) and *Cd44* were induced after immunizations with most vaccines (Fig. 4, A and B, and fig. S6, A and B). In line with reduced mRNA expression, we found a more than 50% reduction in the expression of both MARCO and MRC1/CD206 protein in the medullary LECs of dLNs at 6 hours and 24 hours post-immunization with the mRNA-LNP vaccine Spikevax (Fig. 4, C to F). The 50 to 75% decreases in MRC1/CD206 protein (one of the principal mannose receptors (*37-39*)) correlated with 60 and 93% decreases in the binding of s.c. administered lymph-borne dextran (a mannose–containing molecule) to medullary LECs in mice immunized with Spikevax 6 hours and 24 hours earlier, respectively (Fig. 4, G to I). Thus, there are rapid alterations in scavenger receptor expression and reprogramming of the dLN sinusoidal LEC scavenging functions upon immunization.

Immunization induces changes in junctions of dLN LECs

LECs are held together by adherens and tight junctions (fig. S7A) (*40*). We found that the adherens junction cadherin *Cdh4* was down-regulated and endothelial cell-specific *Cdh5* (VE-cadherin) was up-regulated at 6 hours post-immunization with all four vaccines in SCS floor and medullary sinus LECs (Fig. 5A and fig. S7B). Of the tight junction components, all vaccines down-regulated the expression of claudin 11 (*Cldn11)* in every LEC subpopulation and *Cldn5* in the SCS ceiling, whereas most vaccines induced junctional adhesion molecule A (JAM-A, encoded by *F11r*) expression (Fig. 5A and fig. S7B). We observed VE-cadherin induction at the protein level at 24 hours in the SCS after Spikevax vaccination and in the medullary sinus LECs after Vaxzevria immunization (Fig. 5, B to E). We found three morphologically different junctions, namely smooth-edged leaflets, perpendicular diagonal junctions, and serrated leaflets, in naïve SCS LECs with VE-cadherin staining (Fig. 5F and fig. S7C). VE-cadherin was present in SCS floor LECs in a continuous linear pattern interspersed with globular-like enrichments at the LEC–LEC borders, resembling zipper-like junctions of peripheral LECs (*40, 41*). In vaccine-primed dLNs, we observed a transient increase in the LEC junction perimeter in the SCS at 6 hours after Vaxzevria immunization (Fig. 5G and H), implying an increase in the average LEC size. By contrast, immunization with Nuvaxovid decreased the LEC junction perimeter, whereas Spikevax had no effect. Pecam1/CD31 also outlined the LEC junctions in a continuous pattern in both naïve and Vaxzevria-vaccinated mice (Fig. 5I and movies S3 to S5), although its mRNA was down-regulated in the SCS after the vaccination (Fig. 5A). Furthermore, the induction of *F11r* after Vaxzevria

immunization (Fig. 5A) resulted in higher JAM-A protein expression in the SCS and medullary LECs (fig. S7, D and E, and movies S6 to S8). Thus, junctional gene and protein expression are altered in a vaccine type- and stromal cell subtype-specific manner, but the zipper-like structural organization of junctions is retained, in vaccine-primed sinusoidal LECs.

mRNA-LNP vaccination diminishes transsinusoidal transfer of lymph-borne antigen to dLN

We observed that the transcription of several permeability-associated genes was down-regulated in LECs after all vaccinations (fig. S8A). This suggested that immunization could affect LEC-mediated transcytosis and conduit filling (*3, 42*), which are the key pathways controlling LN barrier function to free lymph-borne antigens. To analyze antigen transcytosis, we used a lymph-borne ~150-kDa IgG antibody that can enter the LN parenchyma within seconds by a fluid-phase vesicular transport system through SCS floor LECs but not via the conduit system (*11*) as a pathway-specific probe. We administered a fluorescently labeled anti-CD45 antibody s.c. into the footpads of mice that had been i.m. vaccinated with Spikevax 6 hours earlier and evaluated the distribution of the antibody tracer after 10 min in the LN parenchyma (Fig. 6A and fig. S8B). We found a > 50% reduction in parenchymal T and B cells binding high amounts of the s.c. administered anti-CD45 antibody (Fig. 6A and fig. S8C). Thus, transsinusoidal transcytosis of lymph-borne antigens through LECs into the LN parenchyma is strongly reduced early post-vaccination.

We observed that transcription of key reticular conduit components—fibrillar collagens I, III, and V forming the core and collagen VI and fibrillin 2 forming the microfibrillar zone (*13*)—was strongly inhibited in three conduit-forming cell types [T cell zone reticular cells (TRCs), *Ccl19*^{hi} TRCs, and interfollicular reticular cells (IFRCs)] (*42*) in dLNs after immunization with any of the four vaccines (Fig. 6B). By contrast, transcripts encoding collagen IV were strongly induced in these three NESC types, whereas those encoding fibronectin, perlecan, nidogen-1, and laminins were largely unaffected by the vaccinations. To functionally test conduit filling in vaccine-primed dLNs, we subcutaneously injected a prototypic conduit probe, fluorescently labeled wheat germ agglutinin (WGA) (*12*, *13*), into mice that had been Spikevax-vaccinated 6 hours earlier (fig. S6D). When the dLN was isolated 2 min after the WGA injection, we observed an almost complete disappearance of the normal conduit-associated WGA signal in the LN after vaccination (Fig. 6C), indicating inhibition of conduit-mediated free antigen transfer.

WGA and other low molecular weight cargoes (e.g., dextrans), which have been used previously to analyze conduit function (*42*), do not have specific ligands in the conduits and require artifact-prone tissue post-fixation methods for visualization. Therefore, we devised s.c. injections of CNA, a 35-kDa bacterial collagen adhesin (*43, 44*), as a physiological in vivo affinity probe that specifically binds fibrillar collagens in the conduit core without the need for fixation. Ex vivo staining with the fluorescent CNA-35-EGFP (enhanced green fluorescent protein) probe revealed colocalization with collagen I staining in the conduits, allowing precise identification of the conduit network (Fig. 6D and fig. S8E). When the CNA-35-EGFP probe was administered s.c. into contralateral (control) footpads of Spikevax immunized mice, by 30 min the probe filled a small proportion of the total conduit network that was identified by ex vivo CNA-35-tdTomato staining (Fig. 6E). Conduit filling was more evident in the proximal subfloor area of the conduit network than in its deeper parts. We observed a significant reduction in conduit filling with the CNA-35 probe 6 hours after Spikevax immunization (Fig. 6, E and F). The overall conduit area

identified by ERTR7 staining or by ex vivo staining with CNA-35 was not diminished after vaccination (fig. S8, F and G). Thus, the physical conduit network is maintained in recently vaccine-primed dLNs, although its capacity to drain lymph-borne cargos is severely reduced.

mRNA-LNP vaccination suppresses ACKR4 expression and chemokine landscape in dLN

The chemokine scavenging receptor atypical chemokine receptor 4 (ACKR4) is the best-established marker of SCS ceiling LECs (*30, 31, 45*). Its expression is essential for generating functional CCL21 gradients, which guide C-C motif chemokine receptor 7 (CCR7)–expressing cells from the SCS into the LN parenchyma (*45-47*). Indeed, *Ackr4* was strongly expressed in ceiling LECs in naïve LNs, but was no longer expressed by these cells 6 hours after immunization with the four different COVID-19 vaccines (Fig. 7A). Using Spikevax as a representative vaccine, we found that ACKR4 immunoreactivity was reduced at 6 hours and 24 hours post-vaccination in the dLN SCS (Fig. 7B). Moreover, when we s.c. administered an A647-tagged ACKR4 ligand, CCL19 (*48*), into Spikevax-immunized mice, we observed reduced binding of the ligand in the SCS LECs in vaccine-dLNs compared to controls (Fig. 7C). Reduced ACKR4 expression and diminished scavenging of s.c. administered CCL19 was confirmed in quantitative analyses (Fig. 7, D and E).

Different vaccines induced distinct early alterations to chemokine transcription in vaccine-dLNs (Fig. 7, F and G, and fig. S9A). Gene-based vaccines increased *Ccl19* transcription in NESCs [the main CCL19-producing cells in LNs (*1, 2*)] and specifically in TRCs and IFRCs. By contrast, the protein vaccine reduced *Ccl19* expression specifically in *Ccl19*^{hi} cells. Transcription of *Ccl21a* [a CCR7 and ACKR4 ligand (*48*)], was unaffected in most LEC and NESC types, but was down-regulated in SCS ceiling LECs by Spikevax and in *Ccl19*^{hi} TRCs by Comirnaty and Nuvaxovid (Fig. 7, F and G). There was also reduced extracellular CCL21 immunoreactivity in dLNs after Spikevax immunization (Fig. 7H). Furthermore, the gene-based vaccines triggered transcription of several additional chemokines, including *Ccl2*, *Ccl7*, *Cxcl9*, *Cxcl10*, and *Cxcl13* in the LEC and NESC subtypes (Fig. 7, F and G).

Migratory DCs play a central role in generating an immune response in the LN following vaccination. Using in vivo migration assays with s.c. administered DsRed^{+} DCs, we observed that the proportion of migratory DCs (DsRed^{+} and CD11c^{+}MHCII^{hi}) in dLNs remained unchanged by Spikevax vaccination (Fig. 7I and fig. S9, B and C). Moreover, migratory DCs localized to the sinusoidal (SCS) and nonsinusoidal compartments of dLNs and non-dLNs in a comparable manner (Fig. 7J). Since DC migration remained intact, our data suggest that DCs may use navigation cues independent of chemokine patterns shaped by ACKR4 to enter the dLN parenchyma during the first 24 hours after vaccination.

Nuvaxovid-triggered eosinophil migration alters stromal architecture in dLNs

We observed abundant small, round, CD31^{lo} cells in the medullary areas of the dLN stroma after protein-based Nuvaxovid vaccination (fig. S10A). These cells were not fluorescent in Ly6G-tdTomato reporter mice (*49*), confirming that they were not neutrophils entering the acutely inflamed dLN. Instead, they expressed Siglec-F (sialic acid binding Ig-like lectin F), had bilobular or multilobular nuclei, and an eosinophilic cytoplasm, which are all characteristic of eosinophils (fig. S10, B and C).

We found naïve LNs and non-dLNs of vaccinated mice to have low eosinophil numbers in quantitative flow cytometric assays (Fig. 8A and fig. S10D). When comparing all four vaccinations, eosinophil infiltration of the dLN was selective for Nuvaxovid (Fig. 8A). By contrast, the increase in eosinophils at the vaccination site in the muscle and the minor changes in eosinophil frequencies in the blood were comparable between the four vaccines (fig. S10, E and F). The LN-infiltrating Siglec-F^+ cells were readily detectable after Nuvaxovid vaccination by histology (Fig. 8B). The LN-residing eosinophils were present at 6 hours post-vaccination, were proliferating ($Ki67^+$) and remained abundant and localized in the medullary area 2 and 5 days post-vaccination (fig. S10, G and H).

To understand the contribution of stromal cells to eosinophil infiltration in Nuvaxovid-immunized mice, we first analyzed the potential routes of eosinophil entry into the LN. We did not find eosinophils in or around HEVs in the LN parenchyma (Fig. 8B and fig. S10G). In Nuvaxovid-immunized fluorescent LEC-reporter mice (ProxTom mice), we observed numerous individual and clustered eosinophils within the SCS and medullary sinus of the LN (Fig. 8C; fig. S10I; and movies S9 and S10). However, eosinophils were not present within the afferent lymphatic vessels outside of the dLN and instead appeared to migrate in the intercellular space of perinodal adipose tissue (Fig. 8C and fig. S10J). Eosinophils frequently formed long narrow tracks with multiple successive cells outside the LN (fig. S10I) and were often localized next to and within the LN capsule. Thus, eosinophils may infiltrate the Nuvaxovid-dLN via the capsule rather than via blood vasculature or afferent lymphatic vessels.

The stromal cells of the dLN exhibited several transcriptional changes that could influence eosinophil infiltration, including the marked up-regulation of the primary eosinophil chemoattractant *Ccl11* (encoding eotaxin-1) in medullary sinus LECs, capsular fibroblasts, and medullary reticular cells (Fig. 8, D and E, and fig. S11A). CCL11 protein was also increased in Nuvaxovid-dLNs (Fig. 8F). Eosinophils isolated from Nuvaxovid-dLNs expressed CCR3, a CCL11 receptor (*50*), and migrated toward recombinant CCL11 in under-agarose migration assays (Fig. 8G and fig. S11, B and C). Sinus LECs also up-regulated *Ccl11* and *Csf3* (colony stimulating factor 3), as well as P-selectin (*Selp*) (Fig. 8D), which supports eosinophil binding in blood vessels (*51*). Flow cytometric analyses confirmed atypical P-selectin protein induction in LECs, rather than BECs (fig. S11D). Thus, stromal cells of Nuvaxovid-dLNs can produce chemotactic and adhesion signals known to induce eosinophil infiltration.

The extracellular matrix architecture was altered in eosinophil-rich areas after Nuvaxovid vaccination. The thickness of the dLN capsule increased at 6 and 24 hours after Nuvaxovid immunization, whereas the capsule at 24 hours was thinner than at baseline after Spikevax immunization (Fig. 8H and fig. S11, E to G). After Nuvaxovid vaccination, the organization of fibrillar collagen was altered, as evidenced by the woven and loose pattern of the CNA-35 probe binding to the capsule surrounding the medullary areas (Fig. 8F). These areas were most heavily infiltrated by eosinophils. Furthermore, Nuvaxovid vaccination altered the matrix composition at the molecular level. mRNA and protein expression of tenascin C (linked to eosinophils and matrix modulation in allergy (*52*)), for example, was different in the Nuvaxovid-dLNs and non-dLNs (Fig. 8, D and E, and fig. S11H).

To study the causal role of eosinophils in the regulation of matrix organization in dLNs, we depleted eosinophils in vivo using an anti-CCR3 antibody treatment before Nuvaxovid immunization (Fig. 8I). The treatment reduced the number of eosinophils in dLN by > 90% compared with the controls (Fig. 8J and fig. S11 I to K). Eosinophil depletion partially reversed

Nuvaxovid immunization–induced capsular thickening and fibrillary collagen loosening in the dLN (Fig. 8K and fig. S11L) suggesting that the observed eosinophil infiltration is causally associated with dLN stromal changes.

DISCUSSION

Stromal priming by vaccinations remains poorly characterized. We report that stromal cells of the dLN become directly transfected with gene-based COVID-19 vaccines and express the immunogenic protein within 2 to 6 hours after vaccination. Immunizations with mRNA-LNP, adenovirus vector, and protein vaccines lead to early shared and vaccine-specific transcriptomic and proteomic responses in different stromal cell types and have functional effects on antigen filtration and leukocyte migration in dLNs.

mRNA-LNP vaccines injected i.m. translate locally at the injection sites and in the liver for several days in mice, and they have been recovered from the blood in humans (*18*, *53*-*55*). Vaccine mRNA has also been recovered from phagocytic myeloid cells in the dLN (*56*), but its presence in dLN stromal cells has not been studied previously. We found several lines of evidence that speak for specific and direct in vivo transfection of selected LECs in vaccine-dLNs. First, not all stromal cells were positive for spike mRNA and S protein. Second, different spike mRNA levels were found in the ceiling and floor LECs within the same SCS compartment after the given vaccination. Third, vaccine-derived spike mRNA was detectable inside LECs by FISH. Fourth, spike mRNA was recovered after vaccinations with the adenovirus vector containing the DNA template for S protein. Finally, only low S protein signal was found in LECs after direct application of high concentration of recombinant S protein into the muscle (the protein vaccine Nuvaxovid). It is possible that sinusoidal LEC is the main LN stromal cell type encountering the highest concentration of transfection competent mRNA-LNP and adenovirus particles, however further validation will be required. The pathways mediating vaccine particle entry further to NESCs (and BECs) in the LN parenchyma remain to be determined, but may include at least endocytosis or transcytosis of the particles through LECs or conduit-mediated transfer, which is capable of transferring vaccinia and Zika viruses (*57*). We demonstrate that vivo transfection of sinusoidal LECs by mRNA-LNP particles is possible, which has potential therapeutic applications for the dLN-targeted manipulation of gene expression in this highly differentiated cell type. Using our filtration pathway-specific probes we observed that the influx of lymph-borne material from the sinus into the LN parenchyma both via transcytosis and conduits is temporarily hampered after immunizations. We propose that this “stromal shutdown” coincides with the known lymphocyte retention during the first day of immune responses (*58*). “Stromal shutdown” may allow for more effective synchronization and modulation of the LN microenvironment according to the first immunogenic exposure without interference from confounding signals from possible subsequent antigen exposures.

Eosinophils may serve as $MHCII^+$ APCs and antigen sensitization in allergic lung inflammation results in eosinophil immigration into the lung dLN via the lymphatics (*59*-*63*). Based on our transcriptomic, imaging, and functional experiments, we propose the following model for eosinophil–stromal cell crosstalk in vaccine-draining LNs. All four vaccines induce eosinophil accumulation at the vaccination site in the muscle. However, only Nuvaxovid triggers strong eosinophilic infiltration into the medullary sinus and paracortex of dLNs. The eosinophil migration appears to occur through extranodal tissues and the LN capsule rather than via blood or lymphatic

vessels. The influx may be driven by chemoattractant and eosinophil growth-supporting molecules expressed in specific stromal cell subsets in the dLN. Since remodeling of the Nuvaxovid-dLN stroma (increased capsular thickness and separation of collagen fibrils) correlates with the eosinophilic infiltration and it is partially reversed after eosinophil depletion in vivo, a causal relationship is supported.

Our study has several limitations. The use of approved proprietary COVID-19 vaccines made it impossible to include specific vehicle controls in our studies. Since the S protein in each vaccine type is relatively similar (*26-29*), we anticipate that the majority of observed stromal responses in LNs were triggered by the adjuvant properties inherent to each vaccine format rather than the specific antigen. However, the immunogen template (mRNA/DNA) or the carrier (LNP/viral particle) alone are not predictive of the stromal response, since these responses were more similar between the mRNA-LNP vaccine (Comirnaty) and adenoviral vector vaccine (Vaxzevria) than between the two different mRNA-LNP vaccines. We contribute to the understanding of dLN responses to other gene-based vaccines that are developed against different pathogens and cancer antigens using the same LNP compositions and adenoviral vectors. It will be important to analyze the full kinetics of stromal responses and their contribution to the efficacy of the ensuing adaptive immune responses in future studies. One final limitation is that the vaccine doses (milligram of body weight) used in our study and in similar experimental models (*56, 64-68*), is much higher than that used in humans. This, and the inherent differences between mouse and human immune systems (*69*), prevent us from making any conclusions on the effects of the vaccinations on stromal cells in humans.

In conclusion, our results describe a stromal dimension to immunizations, including vaccine-type selective in vivo transfection of LN stromal cells. We also show early reprogramming of the stromal cell transcriptome and proteome, a functional stromal shutdown response, and skewed leukocyte migration patterns in response to different vaccines. These modifications in the stromal cell populations heavily precondition the LN landscape for subsequent triggering of adaptive immune responses by migratory DCs.

MATERIALS AND METHODS.

Study design

The goal of this study was to characterize early stromal cell responses in the dLNs after immunization with different types of COVID-19 vaccines. We administered clinically approved mRNA-LNP, adenoviral vector and protein COVID-19 vaccines into mice, and evaluated LEC, BEC and NESC responses in control and dLNs (Fig. 1A). We used scRNA-seq and immunofluorescent imaging to infer transcriptomic and protein level changes (including spike mRNA and S protein expression) in vaccine-primed LNs. The functional effects of the vaccine-induced stromal reprogramming were analyzed using in vivo tests for antigen scavenging, antigen filtration, chemokine binding and leukocyte migration. Sample size and endpoints were chosen based on previous literature, our preliminary data, the “3Rs” principle, and the regulations of our animal license. Mice were randomly assigned to groups, but researchers were not blinded to the experimental groups. The number of samples and experimental replicates are reported in the figure legends. Each data point in the figures refers to an individual sample.

Mice

Wild-type C57BL/6NRj mice were purchased from Janvier Labs. B6;129S-Tg(Prox1-tdTomato)12Nrud/J (ProxTom, stock #018128) reporter mice (*70*) and B6.Cg-Tg(CAG-DsRed*MST)1Nagy/J (DsRed, stock #006051) fluorescent mice (*71*) were purchased from The Jackson Laboratory. Ly6G-tdTomato (CatchupIVM-red214) neutrophil reporter mice were a kind gift from Dr. M. Gunzer (*49*). The mice were housed and bred under specific pathogen-free conditions at the Central Animal Laboratory of the University of Turku. All animal experimentation was approved by the National Animal Experiment Board in Finland (animal license numbers 14685/2020, 22423/2023) and was conducted according to the "3Rs" principle of animal research. Age- and sex-matched 8- to 16-week-old mice were used in each experiment.

Vaccines

Spikevax (Moderna) and Comirnaty (Pfizer-BioNTech) contain 5′ type 2-capped, pseudouridine-modified and human-optimized mRNA for the original SARS-CoV-2 S protein in proprietary LNPs (*27*, *28*). In the Vaxzevria vaccine (AstraZeneca), DNA encoding the SARS-CoV-2 S protein was inserted into a chimpanzee adenovirus ChAdOx1 vector (*26*). Nuvaxovid contains recombinant SARS-CoV-2 S protein emulsified in Matrix-M adjuvant (Novavax) (*29*). To analyze lymphatic drainage, Spikevax was fluorescently labeled as detailed in the Supplementary Materials and Methods. The vaccines were surplus vials from the Finnish national vaccination programs and they were made available for the study by the permission from the Finnish Institute for Health and Welfare. Vaccines were stored and diluted according to the clinical protocols.

Antibodies

All antibodies and dilutions used in this study are listed in table S3.

Immunizations

The vaccines were administered into anesthetized (with 2.3% isoflurane and 250 ml/min oxygen) recipient mice at a dose of 20 µl. We therefore administered 4 µg of Spikevax mRNA, 2 µg of Comirnaty RNA, $> 1 \times 10^7$ Vaxzevria virus particles, and 0.2 µg of protein + 2 µg Matrix-M liposomes of Nuvaxovid vaccine per dose. These doses are comparable to those used in other mouse studies (*56*, *64-68*), albeit much higher (calculated on the basis of dose per kilogram of body weight) than those used in clinical vaccinations. I.m. injections were administered into the lateral gastrocnemius muscle and s.c. injections into the dorsal side of the hind paws using a 30-G needle.

Lymph node stromal cell isolation for scRNA-seq

Popliteal LNs were collected from naïve unvacccinated, vehicle-injected (PBS), or vaccinated mice (20 µl) 6 hours after immunization. A total of 30 draining popliteal LNs were pooled from mice in the same treatment group and processed together for scRNA-seq. Stromal cells were isolated as described previously (*72*). Briefly, the LNs were cut into smaller pieces and digested with 0.8 mg/ml of dispase (Gibco), 0.2 mg/ml of collagenase P (Roche), and 0.1 mg/ml of DNase

I (Roche) in RPMI-1640 at 37°C for 20 min. Extracted cells in the supernatant were collected into FACS buffer (2% FCS and 0.25% NaN_3 in PBS). The remaining tissue fragments were subjected to a second (and third, if needed) 10-min digestion cycle with fresh enzymes. Finally, the supernatants were pooled. To enrich the stromal cells, leukocytes and red blood cells were depleted using CD45 Mouse Microbeads (Miltenyi Biotec) and anti-Ter119 Mouse Microbeads (Miltenyi Biotec) according to the manufacturer's protocol.

Library preparation and scRNA-seq

Stromal cells were processed with the Chromium X platform (10x Genomics) capturing approximately 10,000 cells per sample. scRNA-seq libraries were prepared with the Chromium Next GEM Single Cell 3′ Dual Index v3.1 kit. During cDNA pre-amplification and Sample Index PCR reactions, 12 amplification cycles were used.

The libraries were sequenced using 1% of PhiX spike-in and 28-bp (Read 1), 10-bp (i7 index), 10-bp (i5 index), and 90-bp (Read 2) read lengths on SP and S2 flow cells of the Illumina NovaSeq 6000 Instrument. Data postprocessing including demultiplexing, read alignment, and quality control were performed with Cell Ranger (v6.1.1). To detect S protein mRNA, the genomes were aligned with the reported sequences for Spikevax, Comirnaty, and Vaxzevria (*73*, *74*).

Processing of scRNA-seq data

scRNA-seq data were analyzed using the Seurat (v4.3.0) package in R. As a quality control, genes that were expressed in fewer than three cells, and cells expressing < 200 genes were removed from analysis. Cells expressing < 1000 or > 6000 (> 5000 for Spikevax s.c.) unique gene counts and cells with > 10% mitochondrial genes were also filtered out leaving 3817 to 9489 cells (table S1) for analysis. For the main analysis, naïve, vehicle, Spikevax, Comirnaty, Vaxzevria, and Nuvaxovid samples were combined using Seurat's integration workflow with default parameters. Dimensional reduction using UMAP and nearest-neighbor graph were computed using 40 principal components. Unsupervised clustering was performed using resolution 0.7.

Stromal cells were identified as LECs, BECs, and NESCs based on the expression of canonical markers (LEC: $Prox1^{+}Lyve1^{+}Pecam1^{+}$; BEC: $Prox1^{-}Pecam1^{+}Cdh5^{+}$; and NESC: $Pdpn^{+}Ccl19^{+}Prox1^{-}$) (*30*-*36*). Clusters expressing *Ptprc* or *Epcam* (markers for hematopoietic and epithelial cells, respectively) were excluded from further analysis. For subcluster analyses, dimensional reduction and the nearest-neighbor graph were computed using 30 (LECs, NESCs) or 25 (BECs) principal components. Unsupervised clustering was performed using resolution 0.5 (LECs and BECs) or 0.7 (NESCs). Clusters expressing *Ptprc* or canonical markers from a different subset identity were excluded. To identify subclusters, we analyzed DEGs between the clusters that had a minimum expression of 40% and a log-fold change of 0.5. The markers used to identify 8 LEC, 6 BEC, and 11 NESC clusters are listed in table S4. The protocols used in analyses of spike mRNA expression in different dLN leukocyte subpopulations are outlined in the Supplementary Material and Methods.

DEG analysis

Genes detected at > 20% in either of the two compared samples were tested for differential expression using the Wilcox Ranks Sum test. DEGs with a log-fold change of less than log(2) were removed. DEGs with a multiple comparison adjusted *P* value < 0.05 (Bonferroni-corrected values) were considered as statistically significant. DEG pathway enrichment analysis was done by performing overrepresentation analysis of DEGs within Gene Ontology derived pathways. Samples were divided into gene-based (Spikevax, Comirnaty, Vaxzevria) and protein (Nuvaxovid) vaccination groups. DEGs from LEC, BEC, and NESC were detected from genes expressed > 20% with a log-fold change of > 0.5. Statistically significant DEGs (Bonferroni-corrected *P* value <0.05) were converted to corresponding Entrez-codes (AnnotationDbi v1.62.1) and gene-enrichment analysis for biological processes was performed with clusterProfiler (v4.8.1). Enriched pathways were classified by stromal cell type and ranked for both vaccine groups separately by adjusted *P* values (Benjamini–Hochberg method). The results were visualized using the ComplexHeatmap package (v2.16.0) (*75*). Genome-wide annotations for mouse were acquired from the org.Mm.eg.db package (v3.15.0).

Expression analysis of SARS-CoV-2 spike mRNA and other specific genes

For spike mRNA analyses, the cells in each parent cluster were divided into four categories in relation to the expression of vaccine maximum values (zero: no expression; low: 0 to 33% of maximum value; medium: ≥ 33 to 66% of maximum value; high: ≥ 66 to 100% of maximum value). For analysis of DEGs induced by direct transfection, cells expressing medium or high values of spike mRNA were compared to negative cells (no expression of spike mRNA) in SCS ceiling LECs of Spikevax-samples.

A similarity heatmap was generated with the Complex Heatmap package (v2.16.0) (*75*) using Euclidean distance. Average expression values of each gene from each sample were used to calculate Euclidian distance between the samples. Interferon-inducible (Ref. (*76*) and GO term GO0060337), scavenger receptor (*37, 77*), and junctional (*78*) genes were defined according to the literature. BiomaRt (v2.54.1) (*79*) was used for gene annotation. Stacked violin plots were created with the package scCustomize (v2.0.1).

Processing LNs for microscopy

Popliteal LNs were collected and carefully embedded in Tissue-Tek O.C.T. Compound (Sakura) in a predetermined orientation to produce vertical sections in relation to the hilar blood vessels. Samples were snap-frozen using dry ice, stored at −70°C, and used for cutting cryosections. Tissues from ProxTom reporter mice were fixed in 4% paraformaldehyde (PFA, Santa Cruz, sc-281692), washed, and incubated overnight in 30% sucrose at 4°C before they were embedded in O.C.T.

Immunofluorescence staining

Sections were fixed with ice-cold acetone (unless indicated otherwise). Samples were stained with either primary antibodies followed by appropriate secondary antibodies (diluted in PBS + 5% normal mouse serum (Jackson ImmunoResearch, 015-000-120)), or with directly conjugated primary antibodies (antibodies incubated 1 hour at room temperature unless stated otherwise).

Antibodies and their working dilutions are specified in table S3. DAPI (Invitrogen, D1306) was used for nuclear detection and samples were mounted with ProLong Gold Antifade (Thermo Fisher Scientific, P36930).

For S protein staining, samples were fixed with cold 4% PFA for 5 min at 4°C, washed with PBS, and quenched with 0.1 M glycine. Rabbit anti-S protein polyclonal antibody, which was produced in-house (*80*), was added onto the sections for 1 hour at room temperature followed by Alexa Fluor 488–conjugated goat anti-rabbit IgG secondary antibody (Invitrogen, A11034). When staining for CCL11, samples were fixed as above, blocked with 5% donkey serum (Jackson ImmunoResearch, 005-000-121) for 30 min and incubated with goat anti-mouse CCL11 antibody (R&D, AF420-SP) overnight followed by 1 hour incubation with secondary antibody and the CNA-35-tdTomato probe.

Ten-micron frozen sections were stained for extracellular CCL21 according to previously published protocols (*45, 81*). Briefly, unfixed and unpermeabilized sections were incubated with polyclonal anti-CCL21 (R&D Systems, AF457) overnight at 4°C. After washes with ice-cold PBS, sections were incubated for 4 hours with a secondary antibody at 4°C, washed with ice-cold PBS and fixed with 4% PFA for 10 min at room temperature.

For the ACKR4 staining, 10-μm sections were fixed with ice-cold acetone for 10 minutes, air-dried and stored at −70°C until used. Samples were rehydrated in PBS supplemented with 0.1% bovine serum albumin (BSA) at room temperature, blocked with 10% donkey serum (Merck Life Science, D9663-10ML) for 30 min, and incubated sequentially with goat anti-mouse ACKR4 antibody (Santa Cruz, sc-46835) and Alexa Fluor 488–conjugated donkey anti-goat IgG antibody (Invitrogen, A32814). Hoechst (Abcam, ab228551) was used for nuclear detection.

Primary LN-derived in vitro–cultured stromal cells were fixed with 4% PFA for 10 min at room temperature, washed with PBS three times, and permeabilized with 0.1% Triton X-100 for 15 min at room temperature. After washing cells with PBS three times, cells were blocked with 2% BSA in PBS for 30 min at room temperature and stained with the rabbit anti-S protein polyclonal antibody (*80*) for 30 min at room temperature. Cells were washed with PBS twice and incubated with an Alexa Fluor 488–conjugated goat anti-rabbit IgG secondary antibody (Invitrogen, A11034) and Cy3-conjugated anti-SMA antibody (Sigma, C6198). DAPI (Invitrogen, D1306, 1 μg/ml) was used for nuclear detection and samples were imaged in PBS.

Preparation and analysis of multitissue blocks

The popliteal dLNs with the surrounding perinodal tissue and the shaved skin were harvested, fixed in 4% PFA overnight, washed with PBS, dehydrated in methanol (50% and 100% on ice), and stored in 100% methanol at −20°C until used. The samples were rehydrated in 50% methanol and PBS, mounted into 8% low-melting agarose (Biozym Sieve Genetic Pure Agarose, 850080) and cut into 150-μm thick sections with a Leica VT1200 vibrating blade microtome (Leica Biosystems; amplitude 1.00, speed 0.03 to 0.10 mm/s) under cold PBS. The sections were then incubated with primary antibodies diluted in a staining buffer (PBS supplemented with 0.5% Triton X-100, 0.2% BSA, and 0.05% NaN_3) overnight at 4°C with gentle agitation. Samples were washed with PBS three times (each wash was a minimum of 1 hour) before adding fluorescently labeled secondary antibodies (working concentrations in table S3) diluted in the staining buffer and 5% normal mouse serum. Sections were incubated with antibodies overnight at 4°C with gentle

agitation. When applicable, samples were stained for additional markers as above. Finally, the tissue sections were mounted on microscope slides using Fluoromount-G (Invitrogen, 00-4958-02) with spacers (7 × 30 mm coverslip, thickness #1, ORSAtec GmbH) and a coverslip.

RNA FISH

FISH was performed with the RNAscope Multiplex Fluorescent V2 Assay (Advanced Cell Diagnostics, Cat#310091, 322381, 322809 and 323110) from freshly frozen tissues according to the manufacturer's protocols. Briefly, PFA-fixed and dehydrated LN cryosections were treated with H_2O_2 before digestion with protease IV. Samples were hybridized with custom-made probes against Spikevax (ACD, 1215391-C3) and Comirnaty (ACD, 1116531-C3) spike mRNA as well as *Ifnb1* (ACD, 406531-C1) at 40°C for 2 hours in the ACD HybEZ II hybridization system. After amplification, the signal was developed with the HRP-C3 or HRP-C1 reagent and detected using the Opal 520 secondary antibody (Akoya Biosciences, FP14871001KT). The samples were finally stained with a polyclonal anti-CD31 antibody (R&D, AF3628-SP) and an Alexa Fluor 647–conjugated donkey anti-goat IgG secondary antibody (Invitrogen, A21447) or Alexa 647–conjugated anti-CD21/CD35 antibody (BioLegend, 123423).

In vitro T cell activation by LN stromal cells

To analyze the contribution of vaccine-primed LN LECs in lymphocyte activation in isolation from DCs, we developed an ex vivo assay based on studies showing the capacity of LECs to prime $CD8^+$ cells (*6, 7*). We isolated and enriched stromal cells from naïve or non-dLNs of immunized mice as described above. Cells were cultured on fibronectin-coated (10 µg/ml) (Millipore, 341631) plates in αMEM (Gibco, A10490-01) supplemented with 10% fetal bovine serum (FBS), 1% HEPES (Euroclone, ECM0180D), penicillin and streptomycin (Gibco, 15140-122, 100 units/ml and 100 µg/ml, respectively). Once cells were at an exponential growth phase (typically in 1 to 2 weeks), 6×10^5 to 7×10^5 stromal cells were plated on fibronectin-coated eight-well µ-slides (ibidi, 80826). The next day, cells were transfected with Vaxzevria (1 µl of vaccine in 300 µl of αMEM). After 24 hours, the vaccine was removed and lymphocytes isolated from LNs of untouched, naïve mice were added to stromal cells at a 10:1 ratio and cultured in IMDM medium (Gibco, 12440-053) supplemented with 10% FBS and penicillin/streptomycin. The following day, lymphocytes were collected and processed flow cytometry analysis. Stromal cells were then fixed for 10 min in 4% PFA at room temperature and stained for imaging. Activation of CD8 T cells (indicated by CD69 expression) in cells cocultured with transfected stromal cells was compared to samples where lymphocytes were cultured alone or with non-transfected stromal cells.

In vivo functional assays

To test the LEC scavenging function, 50 µg of fluorescently labeled lysine-fixable 500-kDa FITC-dextran (Invitrogen, D7136) was injected s.c. into mice that were previously i.m. vaccinated with Spikevax (6- and 24-hour time points). Two minutes after the dextran injections, the dLNs were harvested and tissues were fixed in 4% PFA, washed with PBS three times and incubated in 30% sucrose overnight before processing for microscopy as described above.

To study LEC-mediated transcytosis, 5 μg of a monoclonal Alexa Fluor 488–labeled anti-mouse CD45 antibody (BioLegend, 103122) was injected s.c. in a 20-μl volume into mice previously i.m. vaccinated with Spikevax (6-hour time point). Ten minutes after the antibody injections, the dLNs were collected and tissues were processed for flow cytometric detection of the in vivo–bound anti-CD45 antibody.

Conduit filling was determined by injecting 5 μg of Alexa Fluor 647–labeled WGA (Invitrogen, W32466) s.c. into mice previously i.m. vaccinated with Spikevax (6- and 24-hour time points). Two minutes after WGA injections, the dLNs were harvested and processed as described above for the dextran. For the CNA-35 assay, plasmids encoding the CNA-35-EGFP (pET28a-CNA35-EGFP; Plasmid #61603, Addgene) and CNA-35-tdTomato (pET28a-tdTomato-CNA-35; Plasmid #61606, Addgene; gifts from M. Merkx) were transformed into *Escherichia coli* BL21(DE3) and induced with IPTG (*44*). The recombinant proteins were purified using Ni^{2+}-affinity chromatography. Ten micrograms of the probe was injected s.c. in a 20-μl volume into mice previously i.m. vaccinated with Spikevax (6-hour time point). Thirty minutes after the probe was administered the dLNs were collected and processed for microscopy without any fixation.

Recombinant mouse CCL19 (R&D Systems, 440-M3-025/CF) was labeled with the Alexa Fluor 647 microscale protein-labeling kit (Invitrogen, 30009). Two micrograms of fluorescently labeled and filtered CCL19 and AF488-conjugated CD31 antibody (BioLegend, 102514) were then injected s.c. into mice previously i.m. vaccinated with Spikevax (24-hour time point). LNs were collected 30 min after chemokine injections and processed for imaging without any ex vivo staining.

Image acquisition and quantification

The specific models, objectives, cameras, and software of the separate wide-field, stereo, and conventional microscopes, as well as spinning disk and high-resolution confocal microscopes used to examine different immunofluorescently labeled samples are detailed in the Supplementary Materials and Methods.

Image analysis is described in detail in the Supplementary Materials and Methods. Briefly, images were preprocessed and the mean fluorescence intensity (MFI) of target protein was measured from selected regions of the lymph node (such as SCS or medullary sinus) directly from the selected region of interest (ROI) of the target protein staining or from masked areas (e.g., CD31 binary mask based on thresholded signal). The junction perimeter in SCS LECs was measured based on VE-cadherin staining and capsule thickness was measured in the medullary sinus region.

Adoptive transfer of migratory DCs

Bone-marrow derived DCs from $DsRed^{+}$ donor mice were differentiated as previously described (*82*, *83*). Briefly, 8×10^7 to 1×10^8 bone marrow cells harvested from one mouse were cultured with in-house generated granulocyte–macrophage colony-stimulating factor (GM-CSF) hybridoma supernatant for 9 days. Nonadherent cells were then collected and maturated by lipopolysaccharide (200 ng/ml) from *E. coli* 0127:B8 (Sigma-Aldrich, L4516). One million mature DCs ($MHCII^{hi}CD11c^{+}$ verified by flow cytometry) were injected s.c. in a 20-μl volume into both footpads of mice 6 hours after the mice were i.m. vaccinated with Spikevax. DCs were allowed to

migrate for 18 hours and the vaccine-dLN and non-dLNs were collected for flow cytometry analysis or fixed and processed for imaging as described above.

Flow cytometry analysis

Stromal cells and tissue-resident leukocytes were brought into single-cell suspensions using mechanic and enzymatic dissociation of the tissue. LN stromal cells were isolated as described above. LN lymphocytes were released by mechanical homogenization. DCs and eosinophils were isolated from LNs by enzymatic digestions of tissues with 1 mg/ml of collagenase D (Roche) and 50 µg/ml of DNase I (Roche) in Hanks balanced salt solution (HBSS) for 30 min at 37°C. Muscle tissue was processed into a single-cell suspension by digesting minced tissue enzymatically with 3.6 mg/ml collagenase I, 0.65 mg/ml of collagenase XI, and 3 mg/ml of hyaluronidase (all three enzymes from Sigma-Aldrich) for 60 min at 37°C at 300 rpm. All samples were finally filtered to remove cell aggregates. Peripheral blood was collected into 50 µl of heparin and red blood cells were lysed using the BD Pharm Lyse™ Lysing Buffer (BD Biosciences).

When indicated, cells were stained with Fixable Viability Dye eFluor 780 (eBioscience, 65-0865-14) for detection of live cells. Unspecific binding to Fc-receptors was blocked with an anti-CD16/32 antibody (Bio X Cell, BE0307). Cells were stained with fluorescently labeled antibodies diluted in FACS buffer for 30 min at 4°C, washed and fixed with 1% formaldehyde in PBS (except migratory DC and cells from Ly6G-tdTomato-reporter mice which were analyzed without fixing). Samples were acquired with an LSR Fortessa flow cytometer with FACS DiVaTM version 9.2 software (BD). Data were analyzed with the FlowJo software (FlowJo LLC, v10.7.0).

Under-agarose eosinophil migration assay

CCL11-trigged migration of FACS-sorted eosinophils isolated from dLNs of Nuvaxovid-immunized mice (i.m., 24-hour time point) was studied using an under-agarose assay, as detailed in the Supplementary Materials and Methods.

Eosinophil depletion in vivo

To deplete eosinophils in peripheral blood and tissues, mice were administered with 300 µg of anti-CCR3 antibody (BioXCell, BE0316, clone 6S2-19-4) (*84*), isotype control (BioXcell, BE0090, clone LTF-2) or vehicle (PBS) i.v. for 3 consecutive days. On day 3, mice were immunized with Nuvaxovid (i.m.). Tissues were collected 24 hours after immunization and analyzed with flow cytometry and imaging.

Statistical analysis

Numeric data are plotted as means ± SD or means ± SEM. Statistical significance between two groups were determined using the Mann–Whitney *U* test and Student's *t* test, and comparisons between multiple groups using the Kruskal–Wallis *H* test followed by Dunn's post-hoc test. Analyses were performed with GraphPad Prism version 10 (GraphPad Software). *P* values less than 0.05 were considered statistically significant.

Supplementary Materials

Supplementary Materials and Methods

Figs. S1 to S11

Tables S1 to S4

References (*86-92*)

Movies S1 to S10

Data files S1 to S2

MDAR Reproducibility Checklist

REFERENCES AND NOTES

1. A. De Martin, Y. Stanossek, N. B. Pikor, B. Ludewig, Protective fibroblastic niches in secondary lymphoid organs. *J. Exp. Med.* **221**, (2024).
2. A. T. Krishnamurty, S. J. Turley, Lymph node stromal cells: cartographers of the immune system. *Nat. Immunol.* **21**, 369-380 (2020).
3. S. Jalkanen, M. Salmi, Lymphatic endothelial cells of the lymph node. *Nat. Rev. Immunol.* **20**, 556-578 (2020).
4. P. Cruz de Casas, K. Knopper, R. Dey Sarkar, W. Kastenmuller, Same yet different - how lymph node heterogeneity affects immune responses. *Nat. Rev. Immunol.* **24**, 358-374 (2024).
5. T. A. Doan, T. Forward, B. A. J. Tamburini, Trafficking and retention of protein antigens across systems and immune cell types. *Cell. Mol. Life Sci.* **79**, 275 (2022).
6. S. Hirosue, E. Vokali, V. R. Raghavan, M. Rincon-Restrepo, A. W. Lund, P. Corthesy-Henrioud, F. Capotosti, C. Halin Winter, S. Hugues, M. A. Swartz, Steady-state antigen scavenging, cross-presentation, and CD8+ T cell priming: a new role for lymphatic endothelial cells. *J. Immunol.* **192**, 5002-5011 (2014).
7. E. Vokali, S. S. Yu, S. Hirosue, M. Rincon-Restrepo, V. D. F, S. Scherer, P. Corthesy-Henrioud, W. W. Kilarski, A. Mondino, D. Zehn, S. Hugues, M. A. Swartz, Lymphatic endothelial cells prime naive CD8(+) T cells into memory cells under steady-state conditions. *Nat Commun* **11**, 538 (2020).
8. J. Dubrot, F. V. Duraes, L. Potin, F. Capotosti, D. Brighouse, T. Suter, S. LeibundGut-Landmann, N. Garbi, W. Reith, M. A. Swartz, S. Hugues, Lymph node stromal cells acquire peptide-MHCII complexes from dendritic cells and induce antigen-specific CD4(+) T cell tolerance. *J. Exp. Med.* **211**, 1153-1166 (2014).
9. S. M. Walsh, R. M. Sheridan, E. D. Lucas, T. A. Doan, B. C. Ware, J. Schafer, R. Fu, M. A. Burchill, J. R. Hesselberth, B. A. J. Tamburini, Molecular tracking devices quantify antigen distribution and archiving in the murine lymph node. *Elife* **10**, (2021).
10. B. A. Tamburini, M. A. Burchill, R. M. Kedl, Antigen capture and archiving by lymphatic endothelial cells following vaccination or viral infection. *Nat Commun* **5**, 3989 (2014).
11. L. Kahari, R. Fair-Makela, K. Auvinen, P. Rantakari, S. Jalkanen, J. Ivaska, M. Salmi, Transcytosis route mediates rapid delivery of intact antibodies to draining lymph nodes. *J. Clin. Invest.* **129**, 3086-3102 (2019).
12. J. E. Gretz, C. C. Norbury, A. O. Anderson, A. E. Proudfoot, S. Shaw, Lymph-borne chemokines and other low molecular weight molecules reach high endothelial venules via specialized conduits while a functional barrier limits access to the lymphocyte microenvironments in lymph node cortex. *J. Exp. Med.* **192**, 1425-1440 (2000).
13. M. Sixt, N. Kanazawa, M. Selg, T. Samson, G. Roos, D. P. Reinhardt, R. Pabst, M. B. Lutz, L. Sorokin, The conduit system transports soluble antigens from the afferent lymph to resident dendritic cells in the T cell area of the lymph node. *Immunity* **22**, 19-29 (2005).

14. R. Roozendaal, T. R. Mempel, L. A. Pitcher, S. F. Gonzalez, A. Verschoor, R. E. Mebius, U. H. von Andrian, M. C. Carroll, Conduits mediate transport of low-molecular-weight antigen to lymph node follicles. *Immunity* **30**, 264-276 (2009).
15. M. Y. Gerner, K. A. Casey, W. Kastenmuller, R. N. Germain, Dendritic cell and antigen dispersal landscapes regulate T cell immunity. *J. Exp. Med.* **214**, 3105-3122 (2017).
16. M. S. Gebre, L. A. Brito, L. H. Tostanoski, D. K. Edwards, A. Carfi, D. H. Barouch, Novel approaches for vaccine development. *Cell* **184**, 1589-1603 (2021).
17. N. Chaudhary, D. Weissman, K. A. Whitehead, mRNA vaccines for infectious diseases: principles, delivery and clinical translation. *Nat Rev Drug Discov* **20**, 817-838 (2021).
18. N. Pardi, S. Tuyishime, H. Muramatsu, K. Kariko, B. L. Mui, Y. K. Tam, T. D. Madden, M. J. Hope, D. Weissman, Expression kinetics of nucleoside-modified mRNA delivered in lipid nanoparticles to mice by various routes. *J Control Release* **217**, 345-351 (2015).
19. X. Hou, T. Zaks, R. Langer, Y. Dong, Lipid nanoparticles for mRNA delivery. *Nat Rev Mater* **6**, 1078-1094 (2021).
20. K. M. Quinn, D. E. Zak, A. Costa, A. Yamamoto, K. Kastenmuller, B. J. Hill, G. M. Lynn, P. A. Darrah, R. W. Lindsay, L. Wang, C. Cheng, A. Nicosia, A. Folgori, S. Colloca, R. Cortese, E. Gostick, D. A. Price, J. G. Gall, M. Roederer, A. Aderem, R. A. Seder, Antigen expression determines adenoviral vaccine potency independent of IFN and STING signaling. *J. Clin. Invest.* **125**, 1129-1146 (2015).
21. A. Kissenpfennig, S. Henri, B. Dubois, C. Laplace-Builhe, P. Perrin, N. Romani, C. H. Tripp, P. Douillard, L. Leserman, D. Kaiserlian, S. Saeland, J. Davoust, B. Malissen, Dynamics and function of Langerhans cells in vivo: dermal dendritic cells colonize lymph node areas distinct from slower migrating Langerhans cells. *Immunity* **22**, 643-654 (2005).
22. A. A. Itano, S. J. McSorley, R. L. Reinhardt, B. D. Ehst, E. Ingulli, A. Y. Rudensky, M. K. Jenkins, Distinct dendritic cell populations sequentially present antigen to CD4 T cells and stimulate different aspects of cell-mediated immunity. *Immunity* **19**, 47-57 (2003).
23. F. Liang, G. Lindgren, K. J. Sandgren, E. A. Thompson, J. R. Francica, A. Seubert, E. De Gregorio, S. Barnett, D. T. O'Hagan, N. J. Sullivan, R. A. Koup, R. A. Seder, K. Lore, Vaccine priming is restricted to draining lymph nodes and controlled by adjuvant-mediated antigen uptake. *Sci Transl Med* **9**, (2017).
24. R. Verbeke, M. J. Hogan, K. Lore, N. Pardi, Innate immune mechanisms of mRNA vaccines. *Immunity* **55**, 1993-2005 (2022).
25. E. Ben-Akiva, A. Chapman, T. Mao, D. J. Irvine, Linking vaccine adjuvant mechanisms of action to function. *Sci Immunol* **10**, eado5937 (2025).
26. M. Voysey, S. A. C. Clemens, S. A. Madhi, L. Y. Weckx, P. M. Folegatti, P. K. Aley, B. Angus, V. L. Baillie, S. L. Barnabas, Q. E. Bhorat, S. Bibi, C. Briner, P. Cicconi, A. M. Collins, R. Colin-Jones, C. L. Cutland, T. C. Darton, K. Dheda, C. J. A. Duncan, K. R. W. Emary, K. J. Ewer, L. Fairlie, S. N. Faust, S. Feng, D. M. Ferreira, A. Finn, A. L. Goodman, C. M. Green, C. A. Green, P. T. Heath, C. Hill, H. Hill, I. Hirsch, S. H. C. Hodgson, A. Izu, S. Jackson, D. Jenkin, C. C. D. Joe, S. Kerridge, A. Koen, G. Kwatra, R. Lazarus, A. M. Lawrie, A. Lelliott, V. Libri, P. J. Lillie, R. Mallory, A. V. A. Mendes, E. P. Milan, A. M. Minassian, A. McGregor, H. Morrison, Y. F. Mujadidi, A. Nana, P. J. O'Reilly, S. D. Padayachee, A. Pittella, E. Plested, K. M. Pollock, M. N. Ramasamy, S. Rhead, A. V. Schwarzbold, N. Singh, A. Smith, R. Song, M. D. Snape, E. Sprinz, R. K. Sutherland, R. Tarrant, E. C. Thomson, M. E. Torok, M. Toshner, D. P. J. Turner, J.

Vekemans, T. L. Villafana, M. E. E. Watson, C. J. Williams, A. D. Douglas, A. V. S. Hill, T. Lambe, S. C. Gilbert, A. J. Pollard, C. V. T. G. Oxford, Safety and efficacy of the ChAdOx1 nCoV-19 vaccine (AZD1222) against SARS-CoV-2: an interim analysis of four randomised controlled trials in Brazil, South Africa, and the UK. *Lancet* **397**, 99-111 (2021).

27. L. R. Baden, H. M. El Sahly, B. Essink, K. Kotloff, S. Frey, R. Novak, D. Diemert, S. A. Spector, N. Rouphael, C. B. Creech, J. McGettigan, S. Khetan, N. Segall, J. Solis, A. Brosz, C. Fierro, H. Schwartz, K. Neuzil, L. Corey, P. Gilbert, H. Janes, D. Follmann, M. Marovich, J. Mascola, L. Polakowski, J. Ledgerwood, B. S. Graham, H. Bennett, R. Pajon, C. Knightly, B. Leav, W. Deng, H. Zhou, S. Han, M. Ivarsson, J. Miller, T. Zaks, C. S. Group, Efficacy and Safety of the mRNA-1273 SARS-CoV-2 Vaccine. *N. Engl. J. Med.* **384**, 403-416 (2021).
28. F. P. Polack, S. J. Thomas, N. Kitchin, J. Absalon, A. Gurtman, S. Lockhart, J. L. Perez, G. Perez Marc, E. D. Moreira, C. Zerbini, R. Bailey, K. A. Swanson, S. Roychoudhury, K. Koury, P. Li, W. V. Kalina, D. Cooper, R. W. Frenck, Jr., L. L. Hammitt, O. Tureci, H. Nell, A. Schaefer, S. Unal, D. B. Tresnan, S. Mather, P. R. Dormitzer, U. Sahin, K. U. Jansen, W. C. Gruber, C. C. T. Group, Safety and Efficacy of the BNT162b2 mRNA Covid-19 Vaccine. *N. Engl. J. Med.* **383**, 2603-2615 (2020).
29. P. T. Heath, E. P. Galiza, D. N. Baxter, M. Boffito, D. Browne, F. Burns, D. R. Chadwick, R. Clark, C. Cosgrove, J. Galloway, A. L. Goodman, A. Heer, A. Higham, S. Iyengar, A. Jamal, C. Jeanes, P. A. Kalra, C. Kyriakidou, D. F. McAuley, A. Meyrick, A. M. Minassian, J. Minton, P. Moore, I. Munsoor, H. Nicholls, O. Osanlou, J. Packham, C. H. Pretswell, A. San Francisco Ramos, D. Saralaya, R. P. Sheridan, R. Smith, R. L. Soiza, P. A. Swift, E. C. Thomson, J. Turner, M. E. Viljoen, G. Albert, I. Cho, F. Dubovsky, G. Glenn, J. Rivers, A. Robertson, K. Smith, S. Toback, V. S. G. nCo, Safety and Efficacy of NVX-CoV2373 Covid-19 Vaccine. *N. Engl. J. Med.* **385**, 1172-1183 (2021).
30. N. Fujimoto, Y. He, M. D'Addio, C. Tacconi, M. Detmar, L. C. Dieterich, Single-cell mapping reveals new markers and functions of lymphatic endothelial cells in lymph nodes. *PLoS Biol* **18**, e3000704 (2020).
31. M. Xiang, R. A. Grosso, A. Takeda, J. Pan, T. Bekkhus, K. Brulois, D. Dermadi, S. Nordling, M. Vanlandewijck, S. Jalkanen, M. H. Ulvmar, E. C. Butcher, A Single-Cell Transcriptional Roadmap of the Mouse and Human Lymph Node Lymphatic Vasculature. *Front Cardiovasc Med* **7**, 52 (2020).
32. K. Brulois, A. Rajaraman, A. Szade, S. Nordling, A. Bogoslowski, D. Dermadi, M. Rahman, H. Kiefel, E. O'Hara, J. J. Koning, H. Kawashima, B. Zhou, D. Vestweber, K. Red-Horse, R. E. Mebius, R. H. Adams, P. Kubes, J. Pan, E. C. Butcher, A molecular map of murine lymph node blood vascular endothelium at single cell resolution. *Nat Commun* **11**, 3798 (2020).
33. K. Veerman, C. Tardiveau, F. Martins, J. Coudert, J. P. Girard, Single-Cell Analysis Reveals Heterogeneity of High Endothelial Venules and Different Regulation of Genes Controlling Lymphocyte Entry to Lymph Nodes. *Cell Rep* **26**, 3116-3131 e3115 (2019).
34. L. B. Rodda, E. Lu, M. L. Bennett, C. L. Sokol, X. Wang, S. A. Luther, B. A. Barres, A. D. Luster, C. J. Ye, J. G. Cyster, Single-Cell RNA Sequencing of Lymph Node Stromal Cells Reveals Niche-Associated Heterogeneity. *Immunity* **48**, 1014-1028 e1016 (2018).

35. C. Perez-Shibayama, U. Islander, M. Lutge, H. W. Cheng, L. Onder, S. S. Ring, A. De Martin, M. Novkovic, J. Colston, C. Gil-Cruz, B. Ludewig, Type I interferon signaling in fibroblastic reticular cells prevents exhaustive activation of antiviral CD8(+) T cells. *Sci Immunol* **5**, (2020).
36. V. N. Kapoor, S. Muller, S. Keerthivasan, M. Brown, C. Chalouni, E. E. Storm, A. Castiglioni, R. Lane, M. Nitschke, C. X. Dominguez, J. L. Astarita, A. T. Krishnamurty, C. B. Carbone, Y. Senbabaoglu, A. W. Wang, X. Wu, V. Cremasco, M. Roose-Girma, L. Tam, J. Doerr, M. Z. Chen, W. P. Lee, Z. Modrusan, Y. A. Yang, R. Bourgon, W. Sandoval, A. S. Shaw, F. J. de Sauvage, I. Mellman, C. Moussion, S. J. Turley, Gremlin 1(+) fibroblastic niche maintains dendritic cell homeostasis in lymphoid tissues. *Nat. Immunol.* **22**, 571-585 (2021).
37. M. R. PrabhuDas, C. L. Baldwin, P. L. Bollyky, D. M. E. Bowdish, K. Drickamer, M. Febbraio, J. Herz, L. Kobzik, M. Krieger, J. Loike, B. McVicker, T. K. Means, S. K. Moestrup, S. R. Post, T. Sawamura, S. Silverstein, R. C. Speth, J. C. Telfer, G. M. Thiele, X. Y. Wang, S. D. Wright, J. El Khoury, A Consensus Definitive Classification of Scavenger Receptors and Their Roles in Health and Disease. *J. Immunol.* **198**, 3775-3789 (2017).
38. F. Sallusto, M. Cella, C. Danieli, A. Lanzavecchia, Dendritic cells use macropinocytosis and the mannose receptor to concentrate macromolecules in the major histocompatibility complex class II compartment: downregulation by cytokines and bacterial products. *J. Exp. Med.* **182**, 389-400 (1995).
39. J. Wollman, K. Wanniarachchi, B. Pradhan, L. Huang, J. G. Kerkvliet, A. D. Hoppe, N. W. Thiex, Mannose receptor (MRC1) mediates uptake of dextran by bone marrow-derived macrophages. *Mol. Biol. Cell* **35**, ar153 (2024).
40. P. Baluk, D. M. McDonald, Buttons and Zippers: Endothelial Junctions in Lymphatic Vessels. *Cold Spring Harb Perspect Med* **12**, (2022).
41. J. P. Scallan, M. Jannaway, Lymphatic Vascular Permeability. *Cold Spring Harb Perspect Med* **12**, (2022).
42. S. E. Acton, L. Onder, M. Novkovic, V. G. Martinez, B. Ludewig, Communication, construction, and fluid control: lymphoid organ fibroblastic reticular cell and conduit networks. *Trends Immunol.* **42**, 782-794 (2021).
43. K. N. Krahn, C. V. Bouten, S. van Tuijl, M. A. van Zandvoort, M. Merkx, Fluorescently labeled collagen binding proteins allow specific visualization of collagen in tissues and live cell culture. *Anal. Biochem.* **350**, 177-185 (2006).
44. S. J. Aper, A. C. van Spreeuwel, M. C. van Turnhout, A. J. van der Linden, P. A. Pieters, N. L. van der Zon, S. L. de la Rambelje, C. V. Bouten, M. Merkx, Colorful protein-based fluorescent probes for collagen imaging. *PLoS One* **9**, e114983 (2014).
45. M. H. Ulvmar, K. Werth, A. Braun, P. Kelay, E. Hub, K. Eller, L. Chan, B. Lucas, I. Novitzky-Basso, K. Nakamura, T. Rulicke, R. J. Nibbs, T. Worbs, R. Forster, A. Rot, The atypical chemokine receptor CCRL1 shapes functional CCL21 gradients in lymph nodes. *Nat. Immunol.* **15**, 623-630 (2014).
46. Y. Zhang, L. Garcia-Ibanez, C. Ulbricht, L. S. C. Lok, J. A. Pike, J. Mueller-Winkler, T. W. Dennison, J. R. Ferdinand, C. J. M. Burnett, J. C. Yam-Puc, L. Zhang, R. M. Alfaro, Y. Takahama, I. Ohigashi, G. Brown, T. Kurosaki, V. L. J. Tybulewicz, A. Rot, A. E. Hauser, M. R. Clatworthy, K. M. Toellner, Recycling of memory B cells between

germinal center and lymph node subcapsular sinus supports affinity maturation to antigenic drift. *Nat Commun* **13**, 2460 (2022).
47. S. A. Bryce, R. A. Wilson, E. M. Tiplady, D. L. Asquith, S. K. Bromley, A. D. Luster, G. J. Graham, R. J. Nibbs, ACKR4 on Stromal Cells Scavenges CCL19 To Enable CCR7-Dependent Trafficking of APCs from Inflamed Skin to Lymph Nodes. *J. Immunol.* **196**, 3341-3353 (2016).
48. J. Gosling, D. J. Dairaghi, Y. Wang, M. Hanley, D. Talbot, Z. Miao, T. J. Schall, Cutting edge: identification of a novel chemokine receptor that binds dendritic cell- and T cell-active chemokines including ELC, SLC, and TECK. *J. Immunol.* **164**, 2851-2856 (2000).
49. A. Hasenberg, M. Hasenberg, L. Mann, F. Neumann, L. Borkenstein, M. Stecher, A. Kraus, D. R. Engel, A. Klingberg, P. Seddigh, Z. Abdullah, S. Klebow, S. Engelmann, A. Reinhold, S. Brandau, M. Seeling, A. Waisman, B. Schraven, J. R. Gothert, F. Nimmerjahn, M. Gunzer, Catchup: a mouse model for imaging-based tracking and modulation of neutrophil granulocytes. *Nat Methods* **12**, 445-452 (2015).
50. A. Gurtner, D. Crepaz, I. C. Arnold, Emerging functions of tissue-resident eosinophils. *J. Exp. Med.* **220**, (2023).
51. S. D. Robinson, P. S. Frenette, H. Rayburn, M. Cummiskey, M. Ullman-Cullere, D. D. Wagner, R. O. Hynes, Multiple, targeted deficiencies in selectins reveal a predominant role for P-selectin in leukocyte recruitment. *Proc. Natl. Acad. Sci. U.S.A.* **96**, 11452-11457 (1999).
52. H. Abdala-Valencia, M. E. Coden, S. E. Chiarella, E. A. Jacobsen, B. S. Bochner, J. J. Lee, S. Berdnikovs, Shaping eosinophil identity in the tissue contexts of development, homeostasis, and disease. *J. Leukoc. Biol.* **104**, 95-108 (2018).
53. K. Roltgen, S. C. A. Nielsen, O. Silva, S. F. Younes, M. Zaslavsky, C. Costales, F. Yang, O. F. Wirz, D. Solis, R. A. Hoh, A. Wang, P. S. Arunachalam, D. Colburg, S. Zhao, E. Haraguchi, A. S. Lee, M. M. Shah, M. Manohar, I. Chang, F. Gao, V. Mallajosyula, C. Li, J. Liu, M. J. Shoura, S. B. Sindher, E. Parsons, N. J. Dashdorj, N. D. Dashdorj, R. Monroe, G. E. Serrano, T. G. Beach, R. S. Chinthrajah, G. W. Charville, J. L. Wilbur, J. N. Wohlstadter, M. M. Davis, B. Pulendran, M. L. Troxell, G. B. Sigal, Y. Natkunam, B. A. Pinsky, K. C. Nadeau, S. D. Boyd, Immune imprinting, breadth of variant recognition, and germinal center response in human SARS-CoV-2 infection and vaccination. *Cell* **185**, 1025-1040 e1014 (2022).
54. T. E. Fertig, L. Chitoiu, D. S. Marta, V. S. Ionescu, V. B. Cismasiu, E. Radu, G. Angheluta, M. Dobre, A. Serbanescu, M. E. Hinescu, M. Gherghiceanu, Vaccine mRNA Can Be Detected in Blood at 15 Days Post-Vaccination. *Biomedicines* **10**, (2022).
55. A. F. Ogata, C. A. Cheng, M. Desjardins, Y. Senussi, A. C. Sherman, M. Powell, L. Novack, S. Von, X. Li, L. R. Baden, D. R. Walt, Circulating Severe Acute Respiratory Syndrome Coronavirus 2 (SARS-CoV-2) Vaccine Antigen Detected in the Plasma of mRNA-1273 Vaccine Recipients. *Clin. Infect. Dis.* **74**, 715-718 (2022).
56. C. Li, A. Lee, L. Grigoryan, P. S. Arunachalam, M. K. D. Scott, M. Trisal, F. Wimmers, M. Sanyal, P. A. Weidenbacher, Y. Feng, J. Z. Adamska, E. Valore, Y. Wang, R. Verma, N. Reis, D. Dunham, R. O'Hara, H. Park, W. Luo, A. D. Gitlin, P. Kim, P. Khatri, K. C. Nadeau, B. Pulendran, Mechanisms of innate and adaptive immunity to the Pfizer-BioNTech BNT162b2 vaccine. *Nat. Immunol.* **23**, 543-555 (2022).

57. G. V. Reynoso, A. S. Weisberg, J. P. Shannon, D. T. McManus, L. Shores, J. L. Americo, R. V. Stan, J. W. Yewdell, H. D. Hickman, Lymph node conduits transport virions for rapid T cell activation. *Nat. Immunol.* **20**, 602-612 (2019).
58. C. R. Mackay, W. Marston, L. Dudler, Altered patterns of T cell migration through lymph nodes and skin following antigen challenge. *Eur. J. Immunol.* **22**, 2205-2210 (1992).
59. E. A. Jacobsen, K. R. Zellner, D. Colbert, N. A. Lee, J. J. Lee, Eosinophils regulate dendritic cells and Th2 pulmonary immune responses following allergen provocation. *J. Immunol.* **187**, 6059-6068 (2011).
60. J. R. MacKenzie, J. Mattes, L. A. Dent, P. S. Foster, Eosinophils promote allergic disease of the lung by regulating CD4(+) Th2 lymphocyte function. *J. Immunol.* **167**, 3146-3155 (2001).
61. H. B. Wang, P. Akuthota, Y. Kanaoka, P. F. Weller, Airway eosinophil migration into lymph nodes in mice depends on leukotriene C(4). *Allergy* **72**, 927-936 (2017).
62. H. Z. Shi, A. Humbles, C. Gerard, Z. Jin, P. F. Weller, Lymph node trafficking and antigen presentation by endobronchial eosinophils. *J. Clin. Invest.* **105**, 945-953 (2000).
63. H. B. Wang, I. Ghiran, K. Matthaei, P. F. Weller, Airway eosinophils: allergic inflammation recruited professional antigen-presenting cells. *J. Immunol.* **179**, 7585-7592 (2007).
64. A. R. Dvorscek, C. I. McKenzie, V. C. Staheli, Z. Ding, J. White, S. A. Fabb, L. Lim, K. O'Donnell, C. Pitt, D. Christ, D. L. Hill, C. W. Pouton, D. L. Burnett, R. Brink, M. J. Robinson, D. M. Tarlinton, I. Quast, Conversion of vaccines from low to high immunogenicity by antibodies with epitope complementarity. *Immunity* **57**, 2433-2452 e2437 (2024).
65. K. S. Corbett, D. K. Edwards, S. R. Leist, O. M. Abiona, S. Boyoglu-Barnum, R. A. Gillespie, S. Himansu, A. Schafer, C. T. Ziwawo, A. T. DiPiazza, K. H. Dinnon, S. M. Elbashir, C. A. Shaw, A. Woods, E. J. Fritch, D. R. Martinez, K. W. Bock, M. Minai, B. M. Nagata, G. B. Hutchinson, K. Wu, C. Henry, K. Bahl, D. Garcia-Dominguez, L. Ma, I. Renzi, W. P. Kong, S. D. Schmidt, L. Wang, Y. Zhang, E. Phung, L. A. Chang, R. J. Loomis, N. E. Altaras, E. Narayanan, M. Metkar, V. Presnyak, C. Liu, M. K. Louder, W. Shi, K. Leung, E. S. Yang, A. West, K. L. Gully, L. J. Stevens, N. Wang, D. Wrapp, N. A. Doria-Rose, G. Stewart-Jones, H. Bennett, G. S. Alvarado, M. C. Nason, T. J. Ruckwardt, J. S. McLellan, M. R. Denison, J. D. Chappell, I. N. Moore, K. M. Morabito, J. R. Mascola, R. S. Baric, A. Carfi, B. S. Graham, SARS-CoV-2 mRNA vaccine design enabled by prototype pathogen preparedness. *Nature* **586**, 567-571 (2020).
66. M. S. Gebre, S. Rauch, N. Roth, J. Gergen, J. Yu, X. Liu, A. C. Cole, S. O. Mueller, B. Petsch, D. H. Barouch, mRNA vaccines induce rapid antibody responses in mice. *NPJ Vaccines* **7**, 88 (2022).
67. S. E. Magnusson, K. H. Karlsson, J. M. Reimer, S. Corbach-Sohle, S. Patel, J. M. Richner, N. Nowotny, L. Barzon, K. L. Bengtsson, S. Ulbert, M. S. Diamond, L. Stertman, Matrix-M adjuvanted envelope protein vaccine protects against lethal lineage 1 and 2 West Nile virus infection in mice. *Vaccine* **32**, 800-808 (2014).
68. L. D. W. King, D. Pulido, J. R. Barrett, H. Davies, D. Quinkert, A. M. Lias, S. E. Silk, D. J. Pattinson, A. Diouf, B. G. Williams, K. McHugh, A. Rodrigues, C. A. Rigby, V. Strazza, J. Suurbaar, C. Rees-Spear, R. A. Dabbs, A. S. Ishizuka, Y. Zhou, G. Gupta, J. Jin, Y. Li, C. Carnrot, A. M. Minassian, I. Campeotto, S. J. Fleishman, A. R. Noe, R. S.

MacGill, C. R. King, A. J. Birkett, L. A. Soisson, C. A. Long, K. Miura, R. Ashfield, K. Skinner, M. R. Howarth, S. Biswas, S. J. Draper, Preclinical development of a stabilized RH5 virus-like particle vaccine that induces improved antimalarial antibodies. *Cell Rep Med* **5**, 101654 (2024).
69. K. Medetgul-Ernar, M. M. Davis, Standing on the shoulders of mice. *Immunity* **55**, 1343-1353 (2022).
70. L. A. Truman, K. L. Bentley, E. C. Smith, S. A. Massaro, D. G. Gonzalez, A. M. Haberman, M. Hill, D. Jones, W. Min, D. S. Krause, N. H. Ruddle, ProxTom lymphatic vessel reporter mice reveal Prox1 expression in the adrenal medulla, megakaryocytes, and platelets. *Am. J. Pathol.* **180**, 1715-1725 (2012).
71. K. Vintersten, C. Monetti, M. Gertsenstein, P. Zhang, L. Laszlo, S. Biechele, A. Nagy, Mouse in red: red fluorescent protein expression in mouse ES cells, embryos, and adult animals. *Genesis* **40**, 241-246 (2004).
72. A. L. Fletcher, D. Malhotra, S. E. Acton, V. Lukacs-Kornek, A. Bellemare-Pelletier, M. Curry, M. Armant, S. J. Turley, Reproducible isolation of lymph node stromal cells reveals site-dependent differences in fibroblastic reticular cells. *Front Immunol* **2**, 35 (2011).
73. https://github.com/NAalytics/Assemblies-of-putative-SARS-CoV2-spike-encoding-mRNA-sequences-for-vaccines-BNT-162b2-and-mRNA-1273/
74. https://doi.org/10.21203/rs.3.rs-799338/v1
75. Z. Gu, R. Eils, M. Schlesner, Complex heatmaps reveal patterns and correlations in multidimensional genomic data. *Bioinformatics* **32**, 2847-2849 (2016).
76. A. E. Shaw, J. Hughes, Q. Gu, A. Behdenna, J. B. Singer, T. Dennis, R. J. Orton, M. Varela, R. J. Gifford, S. J. Wilson, M. Palmarini, Fundamental properties of the mammalian innate immune system revealed by multispecies comparison of type I interferon responses. *PLoS Biol* **15**, e2004086 (2017).
77. Q. Taban, P. T. Mumtaz, K. Z. Masoodi, E. Haq, S. M. Ahmad, Scavenger receptors in host defense: from functional aspects to mode of action. *Cell Commun Signal* **20**, 2 (2022).
78. N. Wibbe, K. Ebnet, Cell Adhesion at the Tight Junctions: New Aspects and New Functions. *Cells* **12**, (2023).
79. S. Durinck, P. T. Spellman, E. Birney, W. Huber, Mapping identifiers for the integration of genomic datasets with the R/Bioconductor package biomaRt. *Nat Protoc* **4**, 1184-1191 (2009).
80. M. Jiang, P. Kolehmainen, L. Kakkola, S. Maljanen, K. Melen, T. Smura, I. Julkunen, P. Osterlund, SARS-CoV-2 Isolates Show Impaired Replication in Human Immune Cells but Differential Ability to Replicate and Induce Innate Immunity in Lung Epithelial Cells. *Microbiol Spectr* **9**, e0077421 (2021).
81. M. Weber, R. Hauschild, J. Schwarz, C. Moussion, I. de Vries, D. F. Legler, S. A. Luther, T. Bollenbach, M. Sixt, Interstitial dendritic cell guidance by haptotactic chemokine gradients. *Science* **339**, 328-332 (2013).
82. J. Alanko, M. C. Ucar, N. Canigova, J. Stopp, J. Schwarz, J. Merrin, E. Hannezo, M. Sixt, CCR7 acts as both a sensor and a sink for CCL19 to coordinate collective leukocyte migration. *Sci Immunol* **8**, eadc9584 (2023).

83. A. Leithner, J. Renkawitz, I. De Vries, R. Hauschild, H. Hacker, M. Sixt, Fast and efficient genetic engineering of hematopoietic precursor cells for the study of dendritic cell migration. *Eur. J. Immunol.* **48**, 1074-1077 (2018).
84. J. C. Grimaldi, N. X. Yu, G. Grunig, B. W. Seymour, F. Cottrez, D. S. Robinson, N. Hosken, W. G. Ferlin, X. Wu, H. Soto, A. O'Garra, M. C. Howard, R. L. Coffman, Depletion of eosinophils in mice through the use of antibodies specific for C-C chemokine receptor 3 (CCR3). *J. Leukoc. Biol.* **65**, 846-853 (1999).
85. Created in BioRender. Fair-mäkelä, R. (2025) https:// BioRender.com/b9q2mla
86. R. J. Mow, A. Srinivasan, E. Bolay, D. Merlin, C. Yang, Fluorescent Labeling and Imaging of IL-22 mRNA-Loaded Lipid Nanoparticles. *Bio Protoc* **14**, e4994 (2024).
87. J. Schindelin, I. Arganda-Carreras, E. Frise, V. Kaynig, M. Longair, T. Pietzsch, S. Preibisch, C. Rueden, S. Saalfeld, B. Schmid, J. Y. Tinevez, D. J. White, V. Hartenstein, K. Eliceiri, P. Tomancak, A. Cardona, Fiji: an open-source platform for biological-image analysis. *Nat Methods* **9**, 676-682 (2012).
88. W. E. Geslewitz, C. M. Percopo, H. F. Rosenberg, FACS isolation of live mouse eosinophils at high purity via a protocol that does not target Siglec F. *J. Immunol. Methods* **454**, 27-31 (2018).
89. C. T. Rueden, J. Schindelin, M. C. Hiner, B. E. DeZonia, A. E. Walter, E. T. Arena, K. W. Eliceiri, ImageJ2: ImageJ for the next generation of scientific image data. *BMC Bioinformatics* **18**, 529 (2017).
90. D. Ershov, M. S. Phan, J. W. Pylvanainen, S. U. Rigaud, L. Le Blanc, A. Charles-Orszag, J. R. W. Conway, R. F. Laine, N. H. Roy, D. Bonazzi, G. Dumenil, G. Jacquemet, J. Y. Tinevez, TrackMate 7: integrating state-of-the-art segmentation algorithms into tracking pipelines. *Nat Methods* **19**, 829-832 (2022).
91. E. Gomez-de-Mariscal, H. Grobe, J. W. Pylvanainen, L. Xenard, R. Henriques, J. Y. Tinevez, G. Jacquemet, CellTracksColab is a platform that enables compilation, analysis, and exploration of cell tracking data. *PLoS Biol* **22**, e3002740 (2024).
92. Created in BioRender. Fair-mäkelä, R. (2025) https:// BioRender.com/7j82faa

Acknowledgments: We thank E. Virtomaa, S. Mäki, A. Elomaa, P. Weinzettl, P. Laasola, and J. Siivonen for their technical help. We thank Drs. M. Gunzer and P. Rantakari for providing Ly6G-tdTomato-reporter mice and advice. We also thank the Cell Imaging and Cytometry Core, Single Cell Omics Core, Finnish Functional Genomics Centre and Histology Core Facility, University of Turku, for their expertise and instrumentation.

Funding: This research was supported by Research Council of Finland grants 347202 (R.F.-M), 346131 (J.I.), 362007 (J.A.), and 336422 (M.S.), Research Council of Finland InFLAMES Flagship grants 337530, 357910, and 358823, Instrumentarium Science Foundation (J.A.), Sigrid Juselius Foundation grant (M.S.), Sakari Alhopuro Foundation grants 20210041, and 20220168 (R.F.-M.).

Author contributions: Conceptualization: R.F.-M. and M.S. Formal analysis: R.F.-M., P.T., J.N., P.S., I.P., B.G., and J.A. Funding acquisition: R.F.-M. and M.S. Investigation: R.F.-M., P.T., J.N., P.S., I.P., L.K., E.H., and J.A. Methodology: R.F.-M., P.T., J.A., and M.S. Project administration: R.F.-M., and M.S. Resources: I.J., J.I., A.R., and M.S. Supervision: R.F.-M. and M.S. Visualization: R.F.-M., P.T., J.N., E.H., B.G., and J.A. Writing—original draft: R.F.-M. and M.S.

Writing—review and editing: R.F.-M., P.T., J.N., P.S., I.P., L.K., I.J., J.I., E.H., A.R., B.G., J.A., and M.S.

Competing interests: All authors declare that they have no competing interests.

Data and materials availability: scRNA-seq data generated in this study is deposited to GEO, accession number GSE300959. No other type of publicly uploadable data have been generated in this study and no noncommercially-available materials have been used in this study. Tabulated data underlying Figs. 1 to 8 and figs. S1 to S11 are provided in data file S2. All data are available in the main text or the supplementary materials.

Fig. 1. SARS-CoV-2 S protein is present in the stromal cells of dLNs early after gene-based COVID-19 vaccinations. (**A**) Schematic overview of the study depicting sample groups, sites for in vivo administration (i.m., intramuscular; s.c., subcutaneous), analyzed tissues (dLN, draining lymph node; Non-dLN, non-draining lymph node), and read-out assays. Graphics created with BioRender (*85*). (**B**) Immunostaining for S protein (magenta) and endothelial marker CD31 (black) in naïve LNs, dLN subcapsular sinus (SCS), and medullary sinus at 2, 6, and 30 hours after s.c. administration of Spikevax, Comirnaty and Vaxzevria. Scale bars, 50 μm. (**C**) Quantification of the percentage of S protein–positive area in SCS and medullary sinuses within different vaccine groups from (B). (**D**) 3D reconstructions and maximum image projections (single channels for staining shown in boxed regions) for S protein (cyan) and CD31 (magenta) in vibratome samples of multitissue blocks from dLNs 6 hours after i.m. administration of the indicated vaccines and from control naïve LNs. Dashed yellow line, SCS LEC ceiling; arrow, SCS floor; arrowhead, S protein$^+$ medullary sinus LECs; BV, blood vessel. Scale bars, 20 μm. Representative data are from (B and D) 2 to 5 LNs per group from (B) 2 to 3 and (D) 1 to 2 independent experiments. In (C) each data point represents one LN per group from 2 or 3 independent experiments and data are presented as means ± SD.

Fig. 2. LN stromal cells become transfected in vivo by gene-based COVID-19 vaccines. (**A**) Uniform manifold approximation and projection (UMAP) embedding of stromal cells pooled from naïve, vehicle control, and vaccinated mice. UMAP is colored by main stromal cell clusters of lymphatic endothelial cells (LECs), blood endothelial cells (BECs), and nonendothelial stromal cells (NESCs). Expression of their signature genes are shown in violin plots. (**B**) UMAPs of stromal cells from (A) colored by spike mRNA expression. Donut plots show quantifications of spike mRNA expression in the indicated sample groups. Cells with no expression (blue) are shown alongside cells in low (purple), middle (orange), and high (yellow) tertiles of spike mRNA expression. (**C**) UMAP of LEC subset depicting the scRNA-seq clusters and their signature genes shown in violin plots. (**D**) UMAP expression and quantification of spike mRNA expression [donut color-coding as in (B)] in LEC subclusters in the indicated sample groups. (**E**) Fluorescence in situ hybridization (FISH) for vaccine-specific spike mRNA (cyan) in the SCS LECs of the dLN from Spikevax- and Comirnaty-immunized mice stained for CD31 (magenta). Yellow cross indicates location of orthogonal views of the *z*-stacks. Scale bars, 5 μm. (**F** and **G**) Percentage of spike mRNA expressing cells in the indicated subclusters of (F) BECs and (G) NESCs. All data (A to G) are obtained from i.m. immunizations at the 6-hour time point. Data (A to D, F and G) are pooled from 30 LNs and 15 mice per group or (E) representative of 3 LNs per group from 2 independent experiments. Art, arterial endothelial cells; CapEC, capillary endothelial cells; FDC, follicular dendritic cells; HEV, high endothelial venules; IFRC, inter-follicular reticular cells; TBRC, T–B border reticular cells; TRC, T zone reticular cells; TrEC, transitional endothelial cells; MedRC, medullary reticular cells; MRC, marginal reticular cells; SC, stromal cells.

Fig. 3. Different COVID-19 vaccines induce distinct transcriptomic changes in stromal cells of the dLN. (**A**) Similarity plots visualizing Euclidean distance of gene expression between the samples. (**B**) UpSet plot visualizing percentage of unique and shared DEGs in LECs of vaccinated mice compared to naive controls. (**C**) Top up-regulated Gene Ontology pathways induced by gene-based and protein vaccinations. (**D**) Heatmap of top DEGs expressed in LEC medullary sinus clusters after Vaxzevria vaccinations. (**E**) FISH detection of *Ifnb1* (cyan) and CD31 staining (magenta) in Vaxzevria-dLN, n = 4 LNs. Dashed line indicates LN border. Scale bars, 5 μm. (**F** to **I**) PD-L1 expression analyses by (F) scRNA-seq, (G and H) confocal imaging [PD-L1 (green) and

CD31 (magenta), n = 2 to 3 LNs per group], and (I) flow cytometry in dLN after indicated immunizations, n = 3 to 7 samples per group. Scale bars, 50 μm. (**J** to **M**) Analyses of T cell activation by Vaxzevria-transfected primary LN stromal cells. (J) Experimental design. (K) Confocal images of S protein (cyan), smooth muscle actin (SMA, magenta) and nuclei (DAPI, blue) in stromal cells, n = 2. Scale bars, 50 μm. Flow cytometry (L) histograms and (M) quantification of CD69 expression on co-cultured $CD8^+$ lymphocytes (L and M, n = 4 samples per group). Data (A to I) are from i.m. immunizations and scRNA-seq data (A to D, F) from 30 LNs pooled from 15 mice in each group. Data are from (E and G) 3, (H and I) 3 to 5, (K) 2, or (L and M) 4 independent experiments and are presented as means ± SD. Statistical significance was tested using (F) Wilcoxon Rank Sum with Bonferroni-correction (*, $P < 0.05$), (H) Kruskal-Wallis *H* followed by Dunn's post-hoc test, or (I and M) Mann–Whitney *U*. DN, double negative cell; FRC, fibroblastic reticular cell; MFI, mean fluorescence intensity; n.s., not significant; VAX, vaccine.

Fig. 4. Scavenging in the dLN is reprogrammed early after immunizations. (**A**) Heatmaps of scavenger receptor mRNA expression in the LEC SCS ceiling and medullary sinus of naïve and vaccinated mice at 6 hours post-immunization. (**B**) Violin plots showing expression of selected scavenging receptor genes in LEC subpopulations among different vaccination groups. (**C** and **D**) Confocal images of (C) MARCO (green) and LYVE1 (magenta) and (D) MRC1 (green) and LYVE1 (magenta) expression in Spikevax-non-dLN and -dLNs, n = 3 to 7 LNs per group. Scale bars, 50 μm. (**E** and **F**) Quantification of (E) MARCO [from (C)] and (F) MRC1 [from (D)] expression measured by MFI on $LYVE1^+$ cells in the medullary sinus, n = 3 to 7 LNs per group. (**G**) Experimental design for measuring scavenging of s.c. administered fluorescently-labeled dextran in Spikevax-treated mice. Graphics created with BioRender (*85*). (**H**) Confocal images of scavenged dextran (DEX, green) and LYVE1 (magenta) expression in Spikevax-non-dLN and -dLNs, n = 3 to 6 LNs per group. Scale bars, 50 μm. (I) Quantification of scavenged DEX [from (H), n = 3 to 6 LNs per group]. All data (A to F, H and I) are from i.m. immunizations. Data are from (A and B) 30 LNs pooled from 15 mice in each group, from (C to F) 3 to 4, or (H and I) 2 independent experiments and are presented as means ± SD. Statistical significance was tested using (A and B) Wilcoxon Rank Sum with Bonferroni-correction (*, $P < 0.05$) or (E, F, and I) Kruskal-Wallis *H* followed by Dunn's post-hoc test. MFI, mean fluorescence intensity.

Fig. 5. LEC junctions are altered in vaccine-primed dLNs. (**A**) Heatmaps showing mRNA expression of adherens and tight junction molecules in LEC populations in naïve and vaccinated mice at 6 hours post-immunization. (**B** to **D**) Quantification of VE-cadherin (VE-cadh) in non-dLN and dLNs from (B) Spikevax-, (C) Vaxzevria-, and (D) Nuvaxovid-immunized mice, n = 3 to 8 LNs per group. (**E**) Confocal images of VE-cadherin (green) and CD31 (magenta) staining in Vaxzevria-non-dLN and dLNs, n = 3 to 5 LNs per group. Dashed lines mark the SCS ceiling and arrows indicate the SCS floor. Scale bars, 50 μm. (**F** and **G**) Confocal images of VE-cadherin (20- to 30-μm sections) in (F) naïve and (G) Vaxzevria-draining LNs, n = 2 to 4 LNs per group. Scale bars, 20 μm. (**H**) Quantification of the junction perimeter in dLN SCS LECs in immunized mice, n = 2 to 4 LNs per group, each dot represents one cell. For naïve controls, the same data points are visualized in each graph. (**I**) Confocal images of CD31 expression at LEC–LEC contacts in naïve and Vaxzevria-dLNs, n = 3 to 8 LNs per group. Scale bars, 20 μm. All data (A to I) are obtained from i.m. immunizations. Data in (A) are pooled from 30 LNs and 15 mice per group, from (B) 1 to 3, or (C to I) 2 to 4 independent experiments and are presented as means ± SD. Statistical significance was tested using (A) Wilcoxon Rank Sum with Bonferroni-correction (*, $P < 0.05$)

or (B to D and H) Kruskal-Wallis *H* followed by Dunn's post-hoc test. MFI, mean fluorescence intensity; n.s., not significant; P, parenchyma.

Fig. 6. Filtering of lymph-borne antigens is hampered in dLNs early after immunization. (**A)** Flow cytometry data of s.c. administered fluorescently-labeled anti-CD45 antibody binding to LN parenchymal lymphocytes in control LN and Spikevax-dLN, n = 6 LNs per group. Cells were stained ex vivo for CD3 and B220. Quantification of the percentage and mean fluorescence intensity (MFI) of the bound in vivo-administered anti-CD45 antibody analyzed from LN $CD3^+$ T cells and $B220^+$ B cells. (**B**) Heatmaps of conduit-associated genes in NESC subpopulations in dLNs 6 hours post-immunization. (**C**) Confocal images and field-of-view quantification of s.c. administered fluorescently-labeled wheat germ agglutinin (WGA, white) in the conduits of control and dLNs of Spikevax-immunized mice, n = 4 LNs per group. Nuclear detection was achieved with DAPI (blue). Scale bars, 50 µm. (**D**) Confocal images of collagen I (magenta) and collagen-binding CNA-35-EGFP probe (green) in naïve LN conduits, n = 3. Scale bars, 20 µm. (**E**) Confocal images of s.c. administered CNA-35-EGFP probe (green) and ex vivo staining of CNA-35-tdTomato probe (magenta) in control LNs and Spikevax-dLNs. The dashed line marks the LN capsule, n = 5 to 8 LNs per group. Scale bars, 50 µm. (**F**) Quantification of the MFI of the s.c. administered CNA-35-EGFP-probe in the ex vivo stained CNA-35-tdTomato$^+$ LN conduits, n = 5 to 8 LNs per group. All data (A to F) are obtained from i.m. immunizations. Data are from (B) 30 LNs pooled from 15 mice in each group, from (A) 2, or (C to F) 3 independent experiments and are presented as means ± SD. Statistical significance was tested using (A, C, F) Mann–Whitney *U* or (B) Wilcoxon Rank Sum with Bonferroni-correction (*, $P < 0.05$).

Fig. 7. Chemokine landscape is disrupted in vaccine-primed dLNs. (**A**) *Ackr4* and *Prox1* expression in naïve and vaccine-primed dLN LECs. (**B**) Confocal images of ACKR4 (cyan) in naïve and Spikevax-draining LNs, n = 3 LNs per group. Insets show higher magnifications. Scale bars, 50 µm. (**C**) Confocal images showing binding of s.c. co-administered fluorescently-labeled CCL19 (cyan) and anti-CD31 antibody (magenta) in control and Spikevax-draining LNs, n = 6 LNs per group. Scale bars, 50 µm. (**D** and **E**) Quantification of (D) ACKR4 [from (B)] and (E) in vivo scavenged CCL19 [from (C)], n = 3 to 6 LNs per group. (**F** and **G**) Heatmaps of chemokine mRNAs in vaccine-primed dLN (E) LEC and (F) NESC subpopulations. (**H**) Confocal images and quantification of extracellular CCL21 signal (cyan) in Spikevax-non-dLNs and -dLNs, n = 3 to 6 LNs per group. Scale bars, 200 µm. (**I)** Gating and flow cytometry analyses of $DsRed^+$ DC migration into control and Spikevax-draining LNs, n = 7 LNs per group. (**J**) Confocal images of $DsRed^+$ DCs (white) and CD31 (magenta) and quantification of the proportion of $DsRed^+$ DCs in SCS and non-SCS areas of control and Spikevax-draining LNs, n = 5 LNs per group, each dot represents one section. Scale bars, 100 µm. All data (A to J) are from i.m. immunizations. Data in (A, F and G) are from 30 LNs pooled from 15 mice in each group, from (B to E, H) 3, (I) 1, or (J) 2 independent experiments and are presented as means ± SD. Statistical significance was tested using (A, F, and G) Wilcoxon Rank Sum with Bonferroni-correction (*, $P < 0.05$), (D and H) Kruskal-Wallis *H* followed by Dunn's post-hoc test, or (E, I and J) Mann–Whitney *U*. MFI, mean fluorescence intensity; n.s., not significant.

Fig. 8. Nuvaxovid-induced eosinophil infiltration modulates dLN stroma. (**A**) Flow cytometry analyses of LN-eosinophils, n = 4 to 6 samples per group. (**B)** Confocal images of Siglec-F (magenta) and CD31 (green) in Nuvaxovid-non-dLN and -dLNs, n = 4 LNs per group. Scale bars, 200 µm. (**C**) Confocal images of Siglec-F (magenta) and collagen IV (Col IV, cyan) in Nuvaxovid-

immunized ProxTom reporter mouse (LECs in green), n = 2. Scale bars, 200 μm. (**D** and **E**) Heatmaps of eosinophil-related mRNAs in (D) LEC and (E) NESC subpopulations in naïve and Nuvaxovid-draining LNs. (**F**) Confocal images of CCL11 (green) and collagen-binding CNA-35 (magenta) in Nuvaxovid-dLNs, n = 2 to 3 LNs per group. Scale bars, 20 μm. (**G**) Migration of eosinophils (from Nuvaxovid-dLNs) in under-agarose assays. (**H**) Confocal images of CNA-35 (magenta), Col IV (green), and Siglec-F (blue) and quantification of capsular thickness in Nuvaxovid-non-dLNs and -dLNs, n = 4 to 8 LNs per group. Dashed lines indicate capsule borders. Scale bars, 50 μm. (**I** to **K**) Eosinophil-stroma interactions in Nuvaxovid-dLNs. (I) Experimental design. Graphics created with BioRender (*85*). (J) Flow cytometry quantification of eosinophil depletion, n = 3 to 5 samples per group. (K) Confocal images of CNA-35 (magenta), Col IV (green), and Siglec-F (cyan) (dashed lines indicate capsule borders) and quantification of capsular thickness, n = 4 to 5 LNs per group. Scale bars, 50 μm. All data (A to K) are from i.m. immunizations. Data in (D and E) are from 30 LNs pooled from 15 mice in each group, from (A and B, F to H, J and K) 2 to 3, or (C) 1 to 2 independent experiment and are presented as means ± SD. Statistical significance was tested using (A) Kruskal–Wallis *H* test, (D and E) Wilcoxon Rank Sum with Bonferroni-correction (*, $P < 0.05$), (G, J and K) Mann–Whitney *U*, or (H) Kruskal-Wallis *H* followed by Dunn's post-hoc test. P, parenchyma.

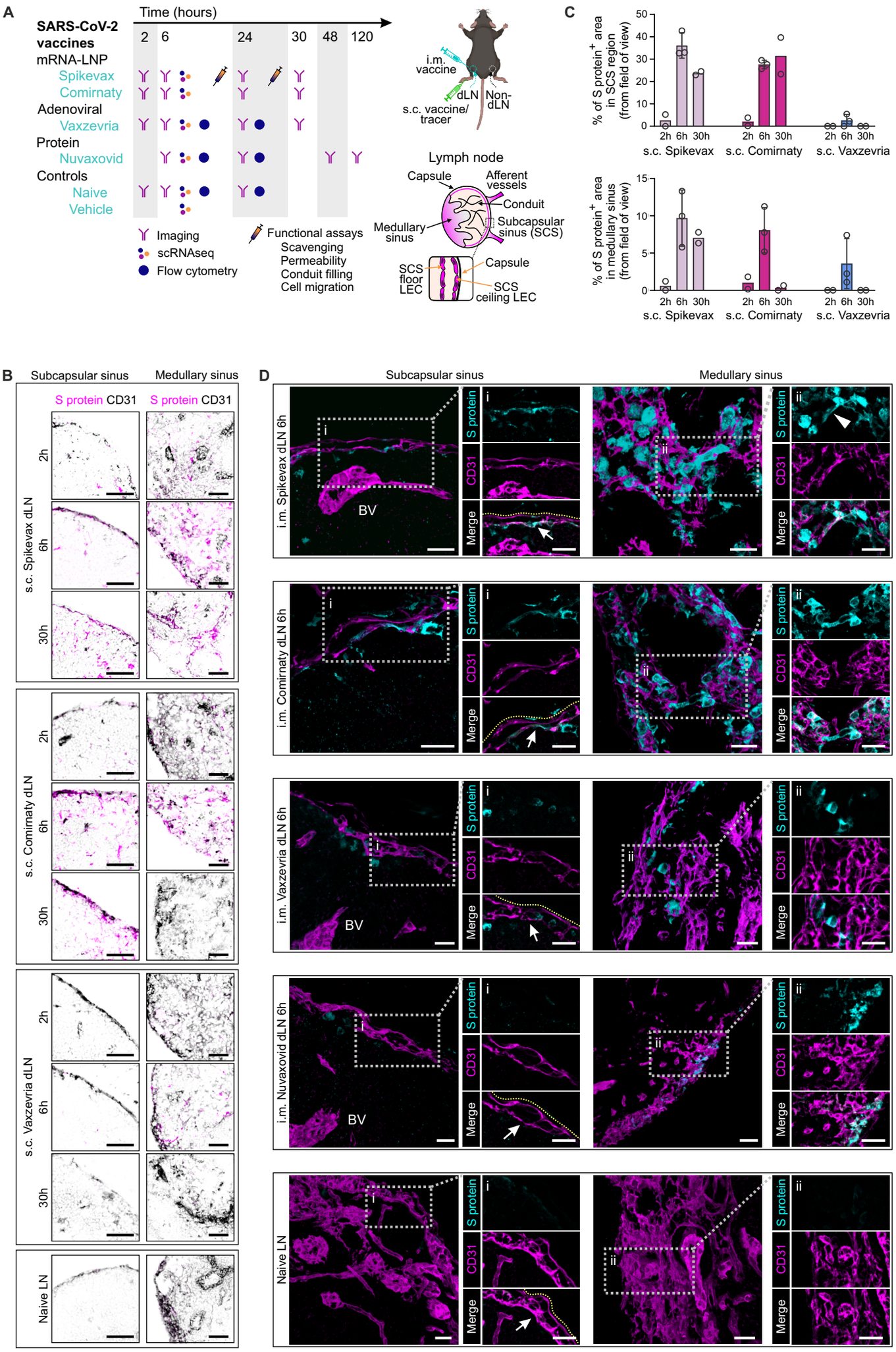
A
SARS-CoV-2 vaccines
mRNA-LNP
Spikevax
Comirnaty
Adenoviral
Vaxzevria
Protein
Nuvaxovid
Controls
Naive
Vehicle
Time (hours)
2
6
24
30
48
120
Imaging
scRNAseq
Flow cytometry
Functional assays
Scavenging
Permeability
Conduit filling
Cell migration
i.m. vaccine
dLN
Non-dLN
s.c. vaccine/ tracer
Lymph node
Capsule
Afferent vessels
Conduit
Subcapsular sinus (SCS)
Medullary sinus
SCS floor LEC
Capsule
SCS ceiling LEC
C
% of S protein+ area in SCS region (from field of view)
s.c. Spikevax
s.c. Comirnaty
s.c. Vaxzevria
% of S protein+ area in medullary sinus (from field of view)
B
Subcapsular sinus
Medullary sinus
S protein CD31
s.c. Spikevax dLN
s.c. Comirnaty dLN
s.c. Vaxzevria dLN
Naive LN
D
i.m. Spikevax dLN 6h
i.m. Comirnaty dLN 6h
i.m. Vaxzevria dLN 6h
i.m. Nuvaxovid dLN 6h
Naive LN
S protein
CD31
Merge
BV

Figure 1

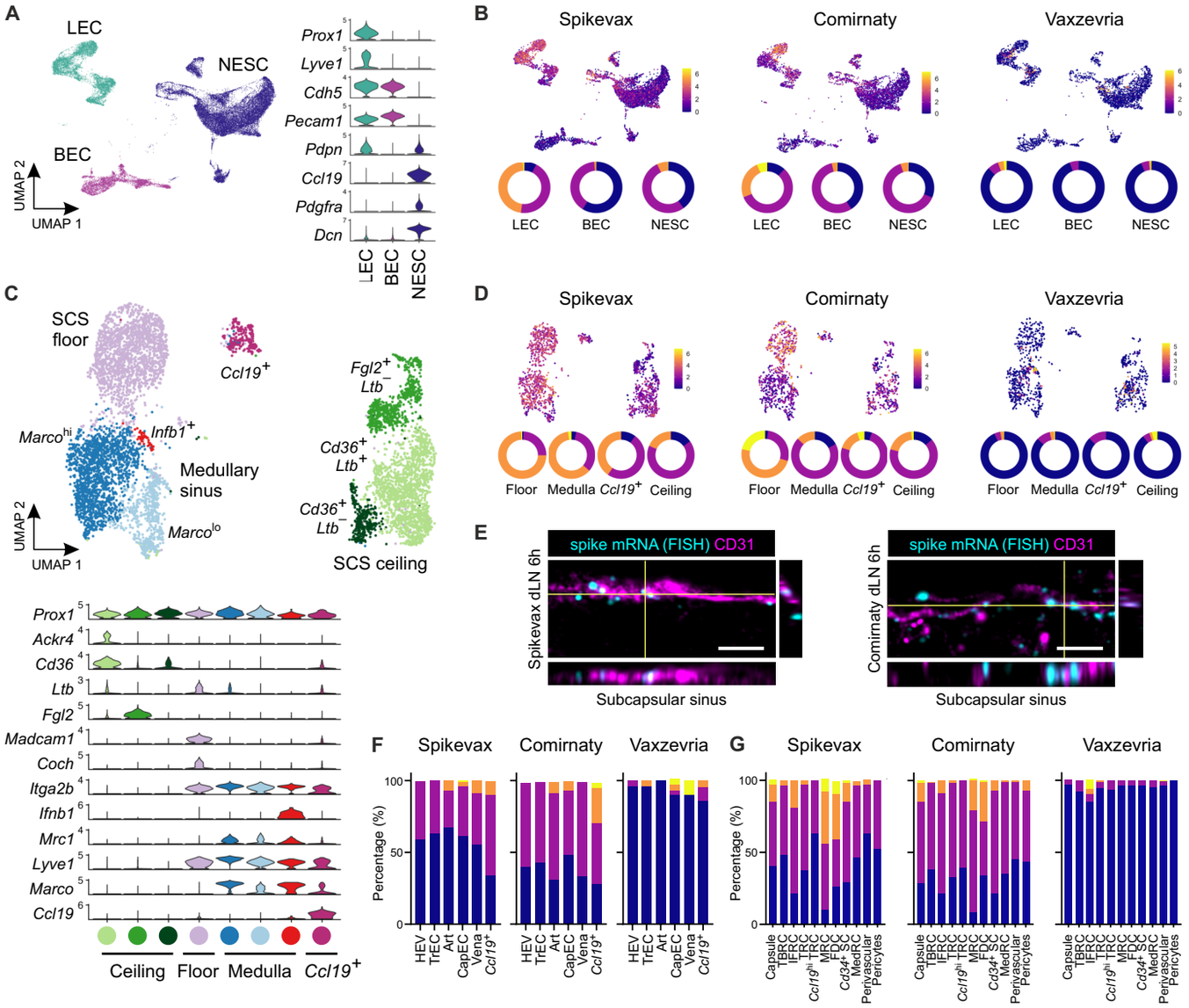
A
LEC
NESC
BEC
UMAP 2
UMAP 1
Prox1
Lyve1
Cdh5
Pecam1
Pdpn
Ccl19
Pdgfra
Dcn
LEC
BEC
NESC
B
Spikevax
Comirnaty
Vaxzevria
LEC
BEC
NESC
C
SCS floor
Ccl19+
Marcohi
Infb1+
Medullary sinus
Marcolo
Fgl2+ Ltb−
Cd36+ Ltb+
Cd36+ Ltb−
SCS ceiling
Prox1
Ackr4
Cd36
Ltb
Fgl2
Madcam1
Coch
Itga2b
Ifnb1
Mrc1
Lyve1
Marco
Ccl19
Ceiling
Floor
Medulla
Ccl19+
D
Spikevax
Comirnaty
Vaxzevria
Floor
Medulla
Ccl19+
Ceiling
E
spike mRNA (FISH) CD31
Spikevax dLN 6h
Comirnaty dLN 6h
Subcapsular sinus
F
Spikevax
Comirnaty
Vaxzevria
Percentage (%)
HEV
TrEC
Art
CapEC
Vena
Ccl19+
G
Spikevax
Comirnaty
Vaxzevria
Percentage (%)
Capsule
IFRC
TRC
Ccl19hi TRC
MRC
FDC
Cd34+ SC
MedRC
Perivascular
Pericytes

Figure 2

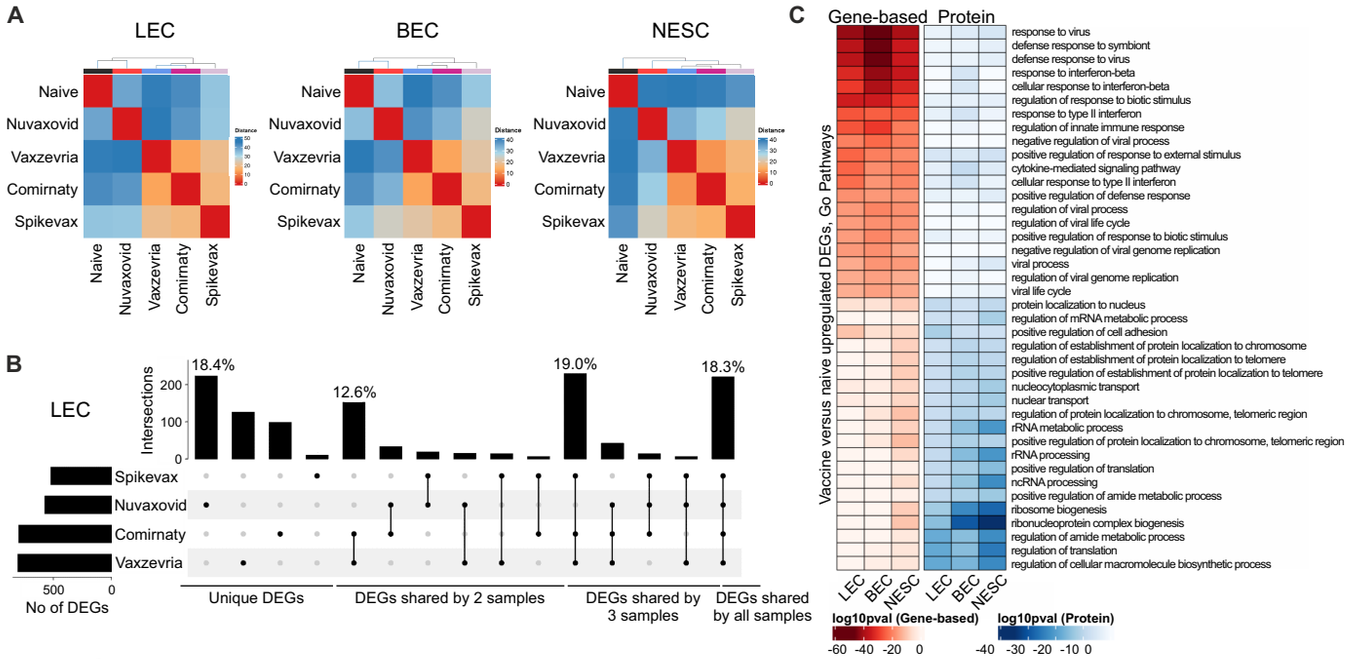
A
LEC
BEC
NESC
Naive
Nuvaxovid
Vaxzevria
Comirnaty
Spikevax
B
LEC
Intersections
18.4%
12.6%
19.0%
18.3%
No of DEGs
Unique DEGs
DEGs shared by 2 samples
DEGs shared by 3 samples
DEGs shared by all samples
C
Gene-based
Protein
Vaccine versus naive upregulated DEGs, Go Pathways
response to virus
defense response to symbiont
defense response to virus
response to interferon-beta
cellular response to interferon-beta
regulation of response to biotic stimulus
response to type II interferon
regulation of innate immune response
negative regulation of viral process
positive regulation of response to external stimulus
cytokine-mediated signaling pathway
cellular response to type II interferon
positive regulation of defense response
regulation of viral process
regulation of viral life cycle
positive regulation of response to biotic stimulus
negative regulation of viral genome replication
viral process
regulation of viral genome replication
viral life cycle
protein localization to nucleus
regulation of mRNA metabolic process
positive regulation of cell adhesion
regulation of establishment of protein localization to chromosome
regulation of establishment of protein localization to telomere
positive regulation of establishment of protein localization to telomere
nucleocytoplasmic transport
nuclear transport
regulation of protein localization to chromosome, telomeric region
rRNA metabolic process
positive regulation of protein localization to chromosome, telomeric region
rRNA processing
positive regulation of translation
ncRNA processing
positive regulation of amide metabolic process
ribosome biogenesis
ribonucleoprotein complex biogenesis
regulation of amide metabolic process
regulation of translation
regulation of cellular macromolecule biosynthetic process
log10pval (Gene-based)
log10pval (Protein)

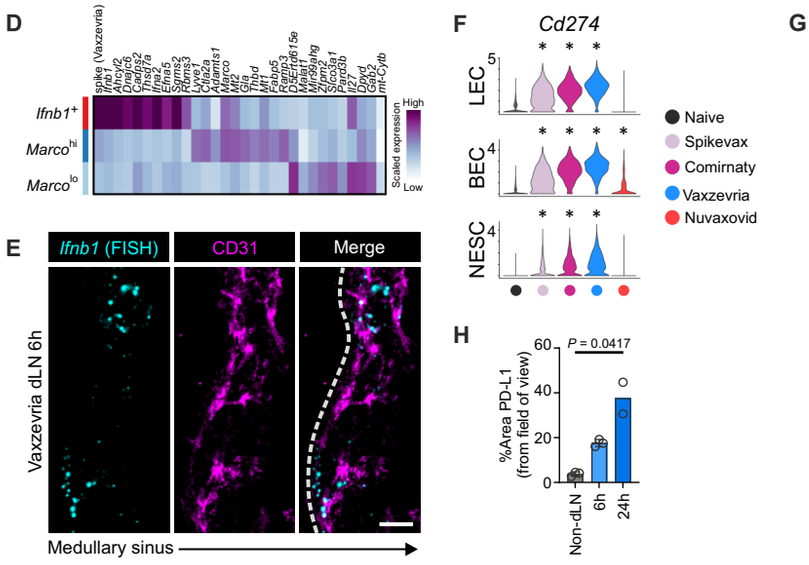
D
Ifnb1+
Marco hi
Marco lo
Scaled expression
High
Low
E
Ifnb1 (FISH)
CD31
Merge
Vaxzevria dLN 6h
Medullary sinus
F
Cd274
LEC
BEC
NESC
Naive
Spikevax
Comirnaty
Vaxzevria
Nuvaxovid
H
P = 0.0417
%Area PD-L1 (from field of view)
Non-dLN
6h
24h

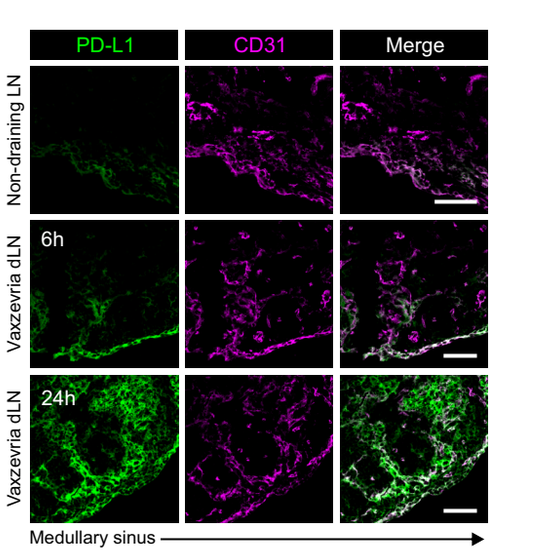
G
PD-L1
CD31
Merge
Non-draining LN
Vaxzevria dLN
6h
24h
Medullary sinus

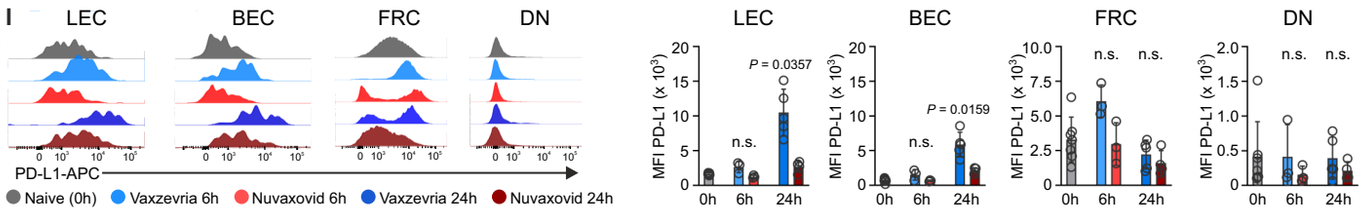
I
LEC
BEC
FRC
DN
PD-L1-APC
Naive (0h)
Vaxzevria 6h
Nuvaxovid 6h
Vaxzevria 24h
Nuvaxovid 24h
MFI PD-L1 (x 10³)
P = 0.0357
P = 0.0159
n.s.
0h
6h
24h

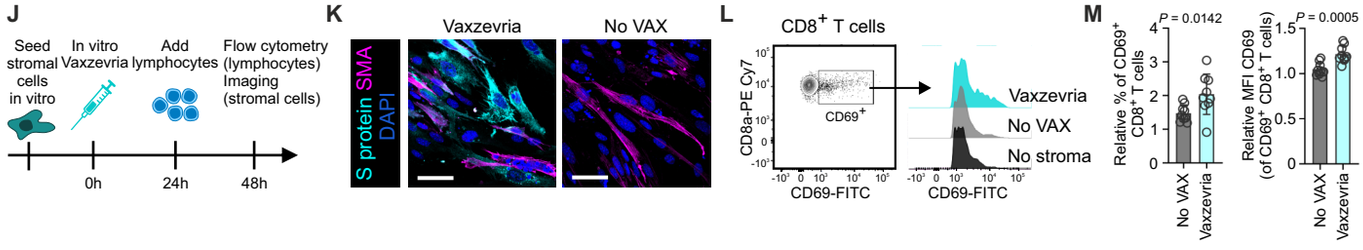
J
Seed stromal cells in vitro
In vitro Vaxzevria
Add lymphocytes
Flow cytometry (lymphocytes)
Imaging (stromal cells)
0h
24h
48h
K
Vaxzevria
No VAX
S protein SMA DAPI
L
CD8+ T cells
CD8a-PE Cy7
CD69+
CD69-FITC
Vaxzevria
No VAX
No stroma
M
P = 0.0142
P = 0.0005
Relative % of CD69+ CD8+ T cells
Relative MFI CD69 (of CD69+ CD8+ T cells)
No VAX
Vaxzevria

Figure 3

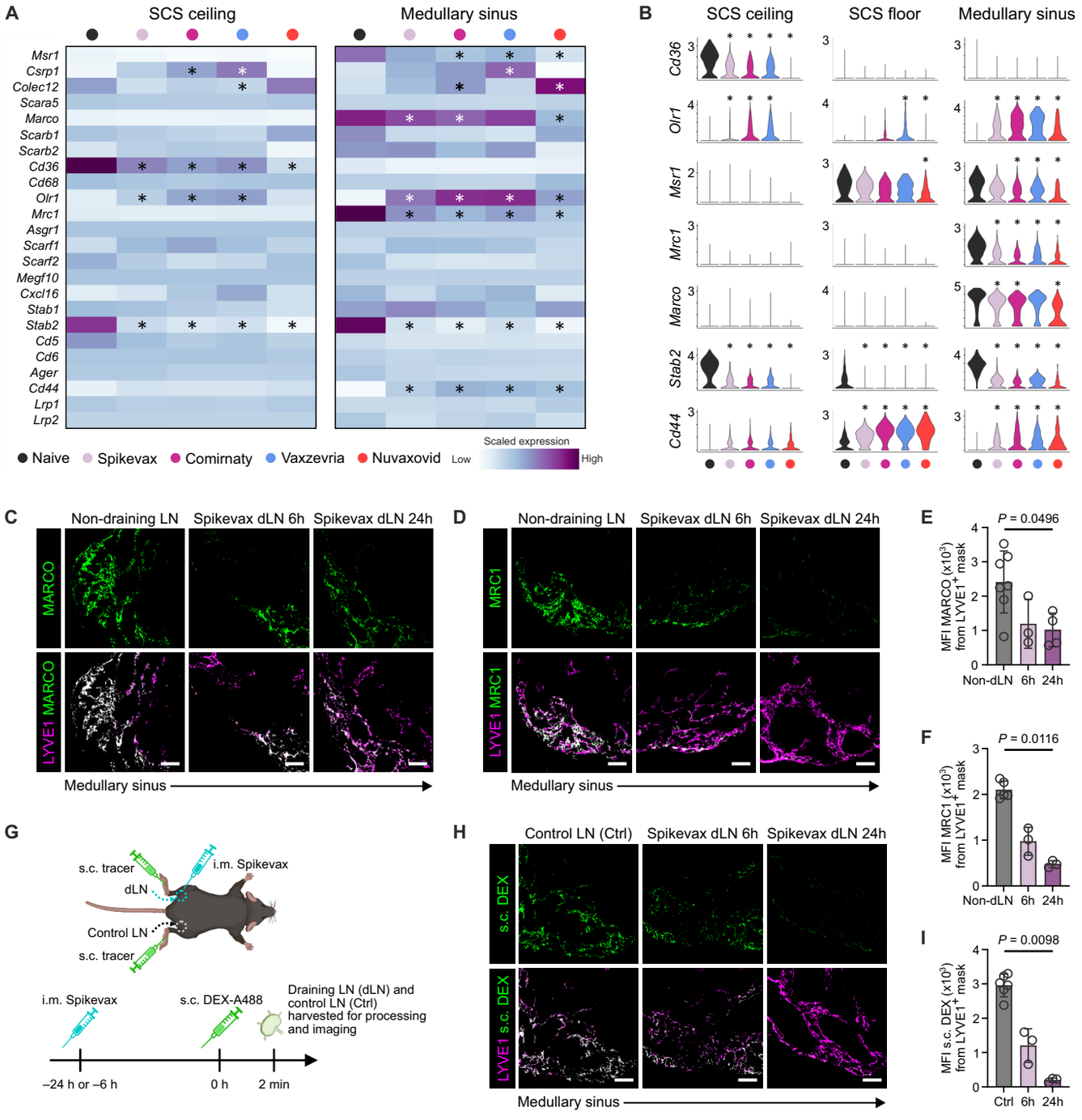
A
SCS ceiling
Medullary sinus
Msr1
Csrp1
Colec12
Scara5
Marco
Scarb1
Scarb2
Cd36
Cd68
Olr1
Mrc1
Asgr1
Scarf1
Scarf2
Megf10
Cxcl16
Stab1
Stab2
Cd5
Cd6
Ager
Cd44
Lrp1
Lrp2
Naive
Spikevax
Comirnaty
Vaxzevria
Nuvaxovid
Scaled expression
Low
High
B
SCS ceiling
SCS floor
Medullary sinus
Cd36
Olr1
Msr1
Mrc1
Marco
Stab2
Cd44
C
Non-draining LN
Spikevax dLN 6h
Spikevax dLN 24h
MARCO
LYVE1 MARCO
Medullary sinus
D
Non-draining LN
Spikevax dLN 6h
Spikevax dLN 24h
MRC1
LYVE1 MRC1
Medullary sinus
E
P = 0.0496
MFI MARCO (x10³) from LYVE1+ mask
Non-dLN
6h
24h
F
P = 0.0116
MFI MRC1 (x10³) from LYVE1+ mask
Non-dLN
6h
24h
G
s.c. tracer
i.m. Spikevax
dLN
Control LN
s.c. tracer
i.m. Spikevax
s.c. DEX-A488
Draining LN (dLN) and control LN (Ctrl) harvested for processing and imaging
–24 h or –6 h
0 h
2 min
H
Control LN (Ctrl)
Spikevax dLN 6h
Spikevax dLN 24h
s.c. DEX
LYVE1 s.c. DEX
Medullary sinus
I
P = 0.0098
MFI s.c. DEX (x10³) from LYVE1+ mask
Ctrl
6h
24h

Figure 4

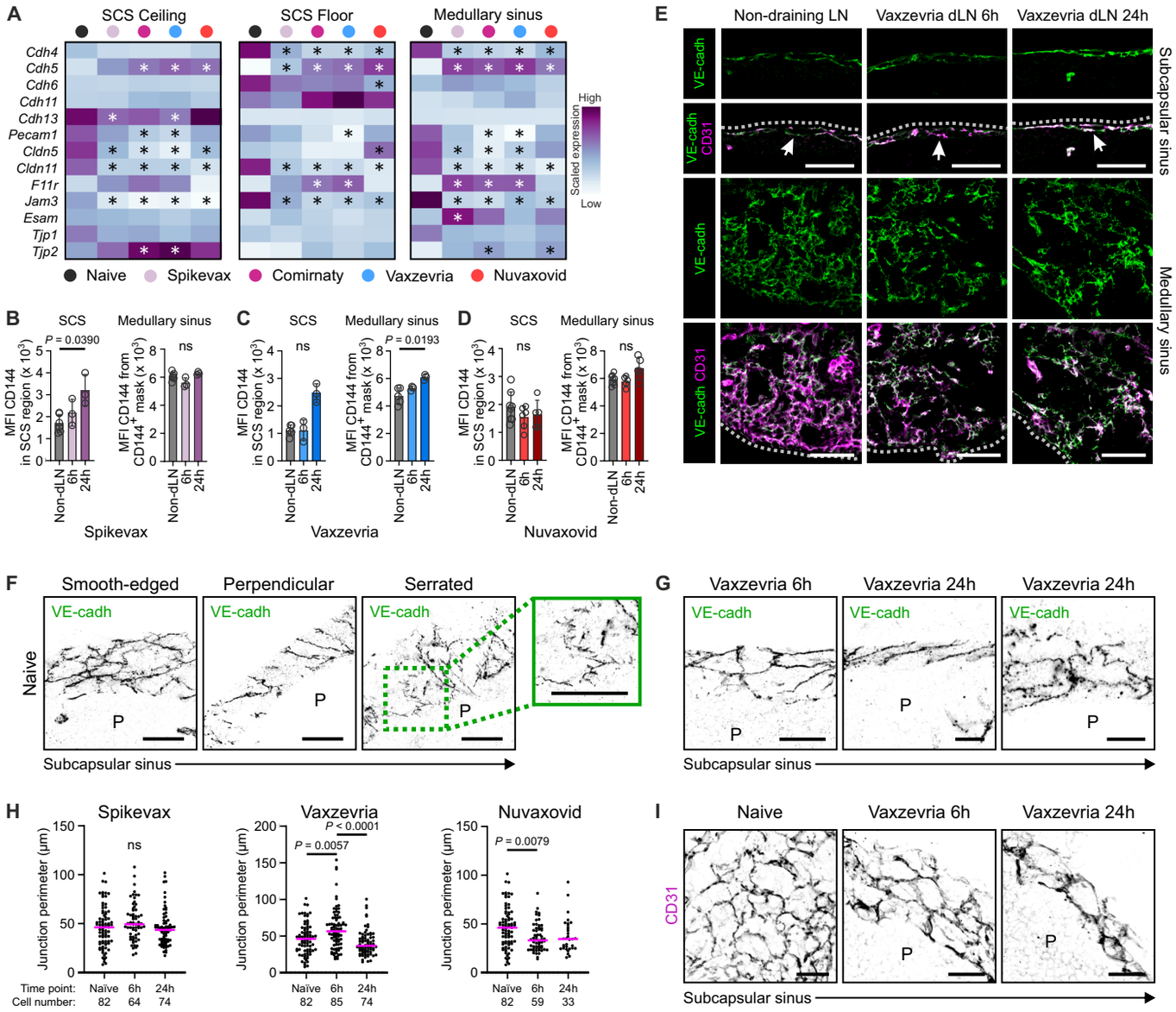
A
SCS Ceiling
SCS Floor
Medullary sinus
Cdh4
Cdh5
Cdh6
Cdh11
Cdh13
Pecam1
Cldn5
Cldn11
F11r
Jam3
Esam
Tjp1
Tjp2
High
Scaled expression
Low
Naive
Spikevax
Comirnaty
Vaxzevria
Nuvaxovid
B
SCS
Medullary sinus
P = 0.0390
ns
MFI CD144 in SCS region (x 10³)
MFI CD144 from CD144+ mask (x 10³)
Non-dLN
6h
24h
Spikevax
C
SCS
Medullary sinus
ns
P = 0.0193
Vaxzevria
D
SCS
Medullary sinus
ns
ns
Nuvaxovid
E
Non-draining LN
Vaxzevria dLN 6h
Vaxzevria dLN 24h
VE-cadh
VE-cadh CD31
Subcapsular sinus
Medullary sinus
F
Smooth-edged
Perpendicular
Serrated
Naive
VE-cadh
P
Subcapsular sinus
G
Vaxzevria 6h
Vaxzevria 24h
Vaxzevria 24h
VE-cadh
P
Subcapsular sinus
H
Spikevax
Vaxzevria
Nuvaxovid
Junction perimeter (µm)
ns
P < 0.0001
P = 0.0057
P = 0.0079
Time point:
Cell number:
Naïve 6h 24h
82 64 74
82 85 74
82 59 33
I
Naive
Vaxzevria 6h
Vaxzevria 24h
CD31
P
Subcapsular sinus

Figure 5

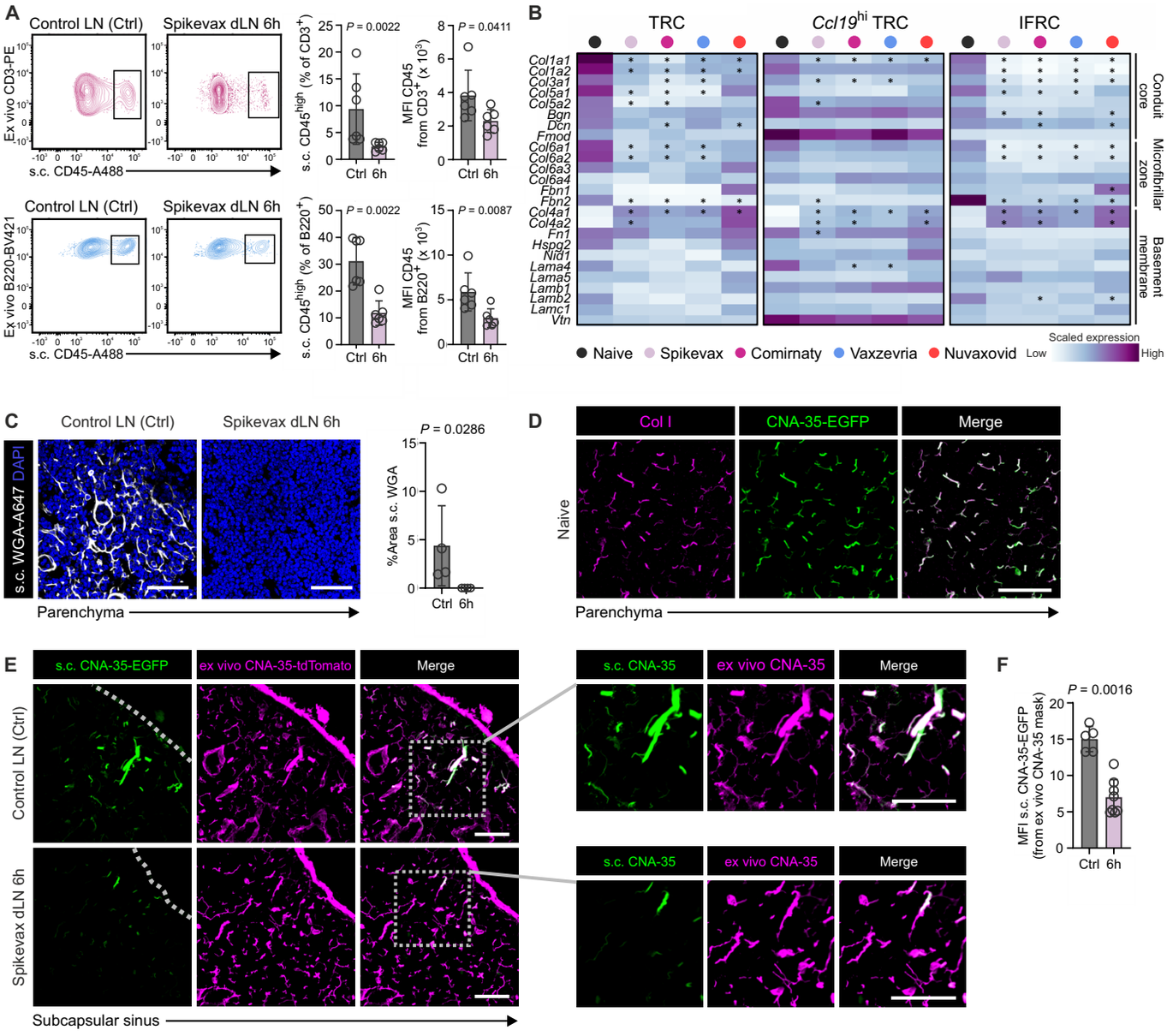
A
Control LN (Ctrl)
Spikevax dLN 6h
Ex vivo CD3-PE
s.c. CD45-A488
s.c. CD45high (% of CD3+)
P = 0.0022
MFI CD45 from CD3+ (x 10³)
P = 0.0411
Ctrl 6h
Ex vivo B220-BV421
s.c. CD45high (% of B220+)
P = 0.0022
MFI CD45 from B220+ (x 10³)
P = 0.0087
B
TRC
Ccl19hi TRC
IFRC
Col1a1
Col1a2
Col3a1
Col5a1
Col5a2
Bgn
Dcn
Fmod
Col6a1
Col6a2
Col6a3
Col6a4
Fbn1
Fbn2
Col4a1
Col4a2
Fn1
Hspg2
Nid1
Lama4
Lama5
Lamb1
Lamb2
Lamc1
Vtn
Conduit core
Microfibrillar zone
Basement membrane
Scaled expression
Low
High
Naive
Spikevax
Comirnaty
Vaxzevria
Nuvaxovid
C
Control LN (Ctrl)
Spikevax dLN 6h
s.c. WGA-A647 DAPI
Parenchyma
P = 0.0286
%Area s.c. WGA
Ctrl 6h
D
Col I
CNA-35-EGFP
Merge
Naive
Parenchyma
E
s.c. CNA-35-EGFP
ex vivo CNA-35-tdTomato
Merge
Control LN (Ctrl)
Spikevax dLN 6h
Subcapsular sinus
s.c. CNA-35
ex vivo CNA-35
Merge
F
P = 0.0016
MFI s.c. CNA-35-EGFP (from ex vivo CNA-35 mask)
Ctrl 6h

Figure 6

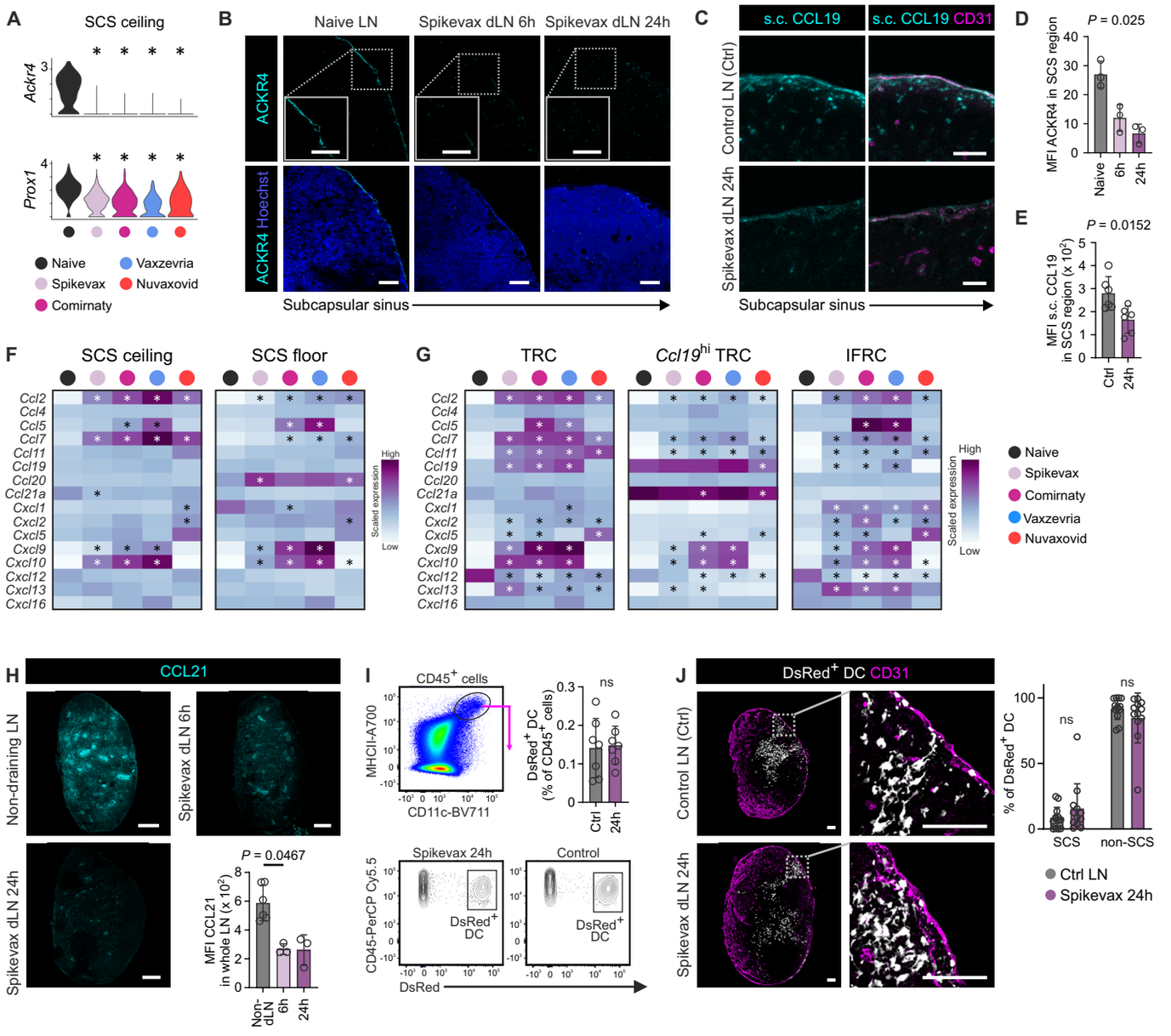
A
SCS ceiling
Ackr4
Prox1
Naive
Spikevax
Comirnaty
Vaxzevria
Nuvaxovid
B
Naive LN
Spikevax dLN 6h
Spikevax dLN 24h
ACKR4
ACKR4 Hoechst
Subcapsular sinus
C
s.c. CCL19
s.c. CCL19 CD31
Control LN (Ctrl)
Spikevax dLN 24h
Subcapsular sinus
D
P = 0.025
MFI ACKR4 in SCS region
Naive
6h
24h
E
P = 0.0152
MFI s.c. CCL19 in SCS region (x 10²)
Ctrl
24h
F
SCS ceiling
SCS floor
Ccl2
Ccl4
Ccl5
Ccl7
Ccl11
Ccl19
Ccl20
Ccl21a
Cxcl1
Cxcl2
Cxcl5
Cxcl9
Cxcl10
Cxcl12
Cxcl13
Cxcl16
High
Low
Scaled expression
G
TRC
Ccl19hi TRC
IFRC
Naive
Spikevax
Comirnaty
Vaxzevria
Nuvaxovid
H
CCL21
Non-draining LN
Spikevax dLN 6h
Spikevax dLN 24h
P = 0.0467
MFI CCL21 in whole LN (x 10²)
Non-dLN
6h
24h
I
CD45+ cells
MHCII-A700
CD11c-BV711
DsRed+ DC (% of CD45+ cells)
ns
Ctrl
24h
Spikevax 24h
Control
CD45-PerCP Cy5.5
DsRed+ DC
DsRed
J
DsRed+ DC CD31
Control LN (Ctrl)
Spikevax dLN 24h
% of DsRed+ DC
ns
SCS
non-SCS
Ctrl LN
Spikevax 24h

Figure 7

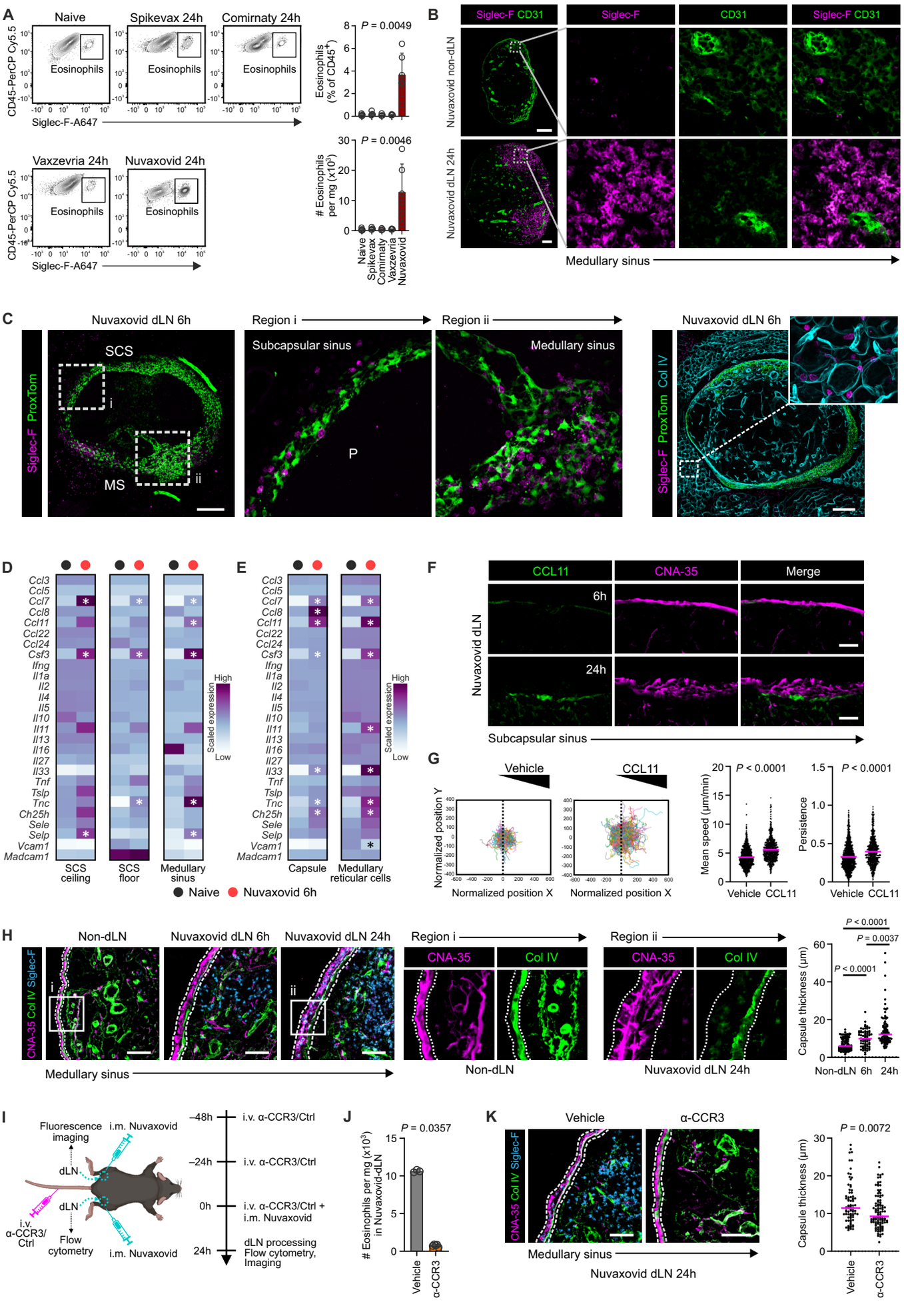
A
Naive
Spikevax 24h
Comirnaty 24h
Vaxzevria 24h
Nuvaxovid 24h
CD45-PerCP Cy5.5
Siglec-F-A647
Eosinophils
P = 0.0049
P = 0.0046
Eosinophils (% of CD45+)
Eosinophils per mg (x10³)
Naive
Spikevax
Comirnaty
Vaxzevria
Nuvaxovid
B
Siglec-F CD31
Siglec-F
CD31
Nuvaxovid non-dLN
Nuvaxovid dLN 24h
Medullary sinus
C
Nuvaxovid dLN 6h
Region i
Region ii
Siglec-F ProxTom
SCS
MS
Subcapsular sinus
Medullary sinus
P
Siglec-F ProxTom Col IV
D
E
Ccl3
Ccl5
Ccl7
Ccl8
Ccl11
Ccl22
Ccl24
Csf3
Ifng
Il1a
Il2
Il4
Il5
Il10
Il11
Il13
Il16
Il27
Il33
Tnf
Tslp
Tnc
Ch25h
Sele
Selp
Vcam1
Madcam1
High
Low
Scaled expression
SCS ceiling
SCS floor
Medullary sinus
Capsule
Medullary reticular cells
Naive
Nuvaxovid 6h
F
CCL11
CNA-35
Merge
6h
24h
Nuvaxovid dLN
Subcapsular sinus
G
Vehicle
CCL11
Normalized position Y
Normalized position X
Mean speed (μm/min)
Persistence
P < 0.0001
Vehicle
CCL11
H
Non-dLN
Nuvaxovid dLN 6h
Nuvaxovid dLN 24h
Region i
Region ii
CNA-35 Col IV Siglec-F
CNA-35
Col IV
Medullary sinus
Non-dLN
Nuvaxovid dLN 24h
Capsule thickness (μm)
P < 0.0001
P = 0.0037
Non-dLN
6h
24h
I
Fluorescence imaging
i.m. Nuvaxovid
dLN
i.v. α-CCR3/Ctrl
Flow cytometry
−48h
−24h
0h
24h
i.v. α-CCR3/Ctrl
i.v. α-CCR3/Ctrl + i.m. Nuvaxovid
dLN processing Flow cytometry, Imaging
J
P = 0.0357
# Eosinophils per mg (x10³) in Nuvaxovid-dLN
Vehicle
α-CCR3
K
Vehicle
α-CCR3
CNA-35 Col IV Siglec-F
Medullary sinus
Nuvaxovid dLN 24h
P = 0.0072
Capsule thickness (μm)

Figure 8